CERN-THESIS-2013-097

THE FLORIDA STATE UNIVERSITY

COLLEGE OF ARTS AND SCIENCES

SEARCH FOR CONTACT INTERACTIONS USING THE INCLUSIVE JET $P_{\mathbf{T}}$ SPECTRUM IN PP COLLISIONS AT $\sqrt{S} = 7$ TEV

By

JEFFREY DAVID HAAS

A Dissertation submitted to the
Department of Physics
in partial fulfillment of the
requirements for the degree of
Doctor of Philosophy

Degree Awarded:
Spring Semester, 2013

Jeffrey David Haas defended this dissertation on March 25, 2013.

The members of the supervisory committee were:

Harrison B. Prosper
Professor Directing Dissertation

Ettore Aldrovandi
University Representative

Laura Reina
Committee Member

Todd Adams
Committee Member

Paul Eugenio
Committee Member

The Graduate School has verified and approved the above-named committee members, and certifies that the dissertation has been approved in accordance with university requirements.

To God, Sunday, Jettson, Maddie, Dad, Mom, Jerry and Lori

ACKNOWLEDGEMENTS

I would like to thank my advisor and mentor, Harrison B. Prosper, for his guidance, insight and inspiration throughout my graduate career. I am grateful to the members of my committee, Todd Adams, Ettore Aldrovandi, Paul Eugenio, and Laura Reina for their time and commitment to guide my academic career in Experimental Physics.

A special thanks to Anwar Bhatti (Chair for EXO-11-010 analysis) Tommaso Dorigo, Jim Francis Hirschauer, Jane Nachtman (Committee members) and David Newbold (language editor) for their excellent support and guidance through the long approval and review process. Also, many thanks to the final document readers: Geoffrey Hall, Bernard Ille, Patrick Janot, David Stuart and Helmut Vogel, for their valuable input. I would like to thank the Exotica Multi-jet conveners: Robert M Harris and Sung-Won Lee, and the CMS Statistics Committee: Tommaso Dorigo (Chair), John Conway, Bob Cousins, Luc Demortier, Ulrich Heintz, Supriya Jain, Louis Lyons, Jochen Ott, Fedor Ratnikov, and Michael Schmitt, for their valuable guidance and suggestions.

I would like to thank Oliver Gutsche for the opportunity to present my Tier-1 computing experience at CHEP 2010 in Taiwan. I give many thanks to all of those involved who helped to publish those proceedings. I would like to thank Alan Hahn for the opportunity to evaluate silicon photomultipliers at the CMS hadron calorimeter test beam in 2009 at CERN. I would like to thank Sudhir Malik and Sezen Sekmen for their great insight and inspiration.

I would like to thank the professors, postdocs, and students in the high energy physics group of Florida state university; the Fermilab community for their helping hands and making the lab such a welcoming place; the CERN staff and the technical staffs of the institutes participating in CMS; and the United States Department of Energy for its financial support of my research.

I am thankful to my family and friends for believing in me and supporting me. This work would never have been possible without God, my wonderful wife Sunday who holds my

heart, the support of my parents, Norris and Ellen Haas, my sister Lori and her husband, Jerry Ernst.

My most valuable inspiration is always my son, Jettson James Haas.

TABLE OF CONTENTS

LIST OF TABLES

LIST OF FIGURES

ABSTRACT

We report results of a search for a deviation in the jet production cross section from the prediction of perturbative quantum chromodynamics at next-to-leading order. The search is conducted using a 7 TeV proton-proton data sample corresponding to an integrated luminosity of 5.0 fb^{-1}, collected with the Compact Muon Solenoid detector at the Large Hadron Collider. A deviation could arise from interactions characterized by a mass scale Λ too high to be probed directly at the LHC. Such phenomena can be modeled as contact interactions. No evidence of a deviation is found. Using a Bayesian method lower limits are set on Λ of 10.1 TeV and 14.1 TeV at 95% confidence level for models with destructive and constructive interference, respectively.

CHAPTER 1

INTRODUCTION

"Physical concepts are free creations of the human mind, and are not, however it may seem, uniquely determined by the external world. In our endeavor to understand reality we are somewhat like a man trying to understand the mechanism of a closed watch. He sees the face and the moving hands, even hears its ticking, but he has no way of opening the case. If he is ingenious he may form some picture of a mechanism which could be responsible for all the things he observes, but he may never be quite sure his picture is the only one which could explain his observations. He will never be able to compare his picture with the real mechanism and he cannot even imagine the possibility or the meaning of such a comparison. But he certainly believes that, as his knowledge increases, his picture of reality will become simpler and simpler and will explain a wider and wider range of his sensuous impressions. He may also believe in the existence of the ideal limit of knowledge and that it is approached by the human mind. He may call this ideal limit the objective truth." [1]

1.1 The goal of particle physics

Questions about fundamental aspects of the universe are difficult ones to answer. In order to tackle questions, such as:

- What are the building blocks of our universe?
- What forces form the world in which we live?
- What drives the evolution of the universe, from the Big Bang to the present state?

particle physics describes the world in terms of fundamental constituents of matter and their mutual interactions. Theoretical and experimental particle physicists have been very

successful in uncovering new principles of nature and many unsuspected features of the universe, which resulted in a detailed physical theory called the Standard Model (SM). The SM is a field theory, based on a Lagrangian, L_{SM}, that describes the weak, electromagnetic and strong interactions of a set of fundamental fields.

If we work with units in which $\hbar = c = 1$, the Lagrangian has units of mass^4. We can consider the SM as an effective theory that is the limit of a more general theory described by the Lagrangian $L_{new-theory}$ [2], which can be expressed as an expansion in $1/M$,

$$L_{new\ theory} = L_{SM} + \frac{1}{M} dim5 + \frac{1}{M^2} dim6 + \ldots, \tag{1.1}$$

where M denotes a large mass scale and dim represents one or more dimension n operators. At energies much less than M, the dominant terms in this new theory will be those of the SM, because the other terms are suppressed by an inverse power of M.

The SM describes the world very accurately, however, there are several questions still left unanswered. A sample of questions can be broken into two parts, experimental ones and theoretical ones.

- Experimental questions:
  - What is the nature of dark matter?
  - What is the nature of dark energy?
  - Where do neutrino masses come from?
  - What is the origin of the matter-antimatter asymmetry?
- Theoretical questions:
  - How do particles acquire mass?
  - Are protons stable?
  - How does gravity fit in?
  - Can one theory describe all fundamental fields, including the gravitational field?

These are some of the questions which define our experimental path for the future of particle physics. It is perfectly plausible that the terms suppressed by the large mass scale could answer some of these questions.

Historically, objects that were once thought to be elementary, such as those shown in Figure 1.1, actually turn out to be composite structures. The current set of elementary particles is shown in Figure 1.2. Evidence of compositeness of one or more particles in

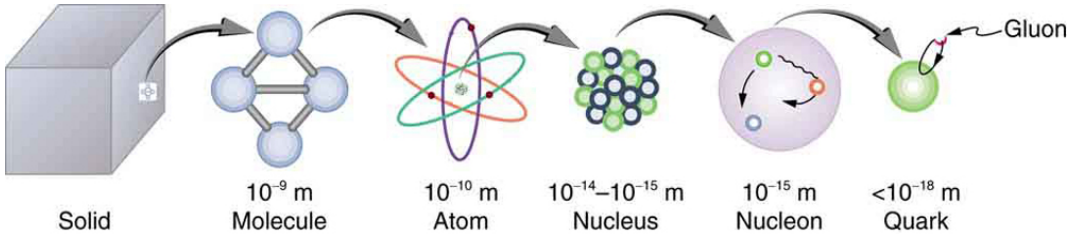

Figure 1.1. The discovery of composite structures in decreasing size over time.

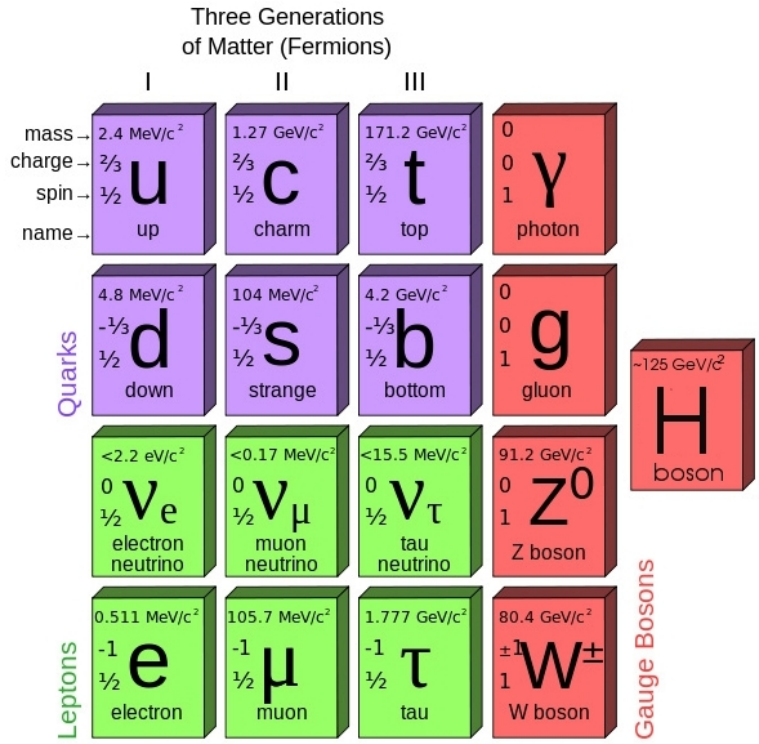

Figure 1.2. Three generations of particles, which make up the building blocks of matter: six quarks and six leptons. The particles in the right most column are associated with the fundamental forces.

Figure 1.2 would show that some of the higher order terms in Equation 1.1 exist.

In 1934 Enrico Fermi developed a theory of the β decay, in which the latter was described as an interaction between 4-fermion fields at a point, as depicted in Figure 1.3. Such an interaction is called a contact interaction. The electroweak theory, developed in the 1960s, replaced the four fermion contact interaction with interactions involving the exchange of W and Z bosons between fermions. Figure 1.3 shows the description of neutron beta decay as a contact interaction and the description according to the electroweak theory. In the electroweak description the matrix element contains a propagator that represents the exchange of a W^-. This propagator goes like $1/(q^2 - M^2)$ where M here is a large mass scale, in this case the mass of the (virtual) W boson. For low momentum transfers $q << M$, q can be neglected and the propagator becomes $1/M^2$. In this case, the theory reduces to a 4-quark contact interaction theory. If quarks and leptons are composite, with at least

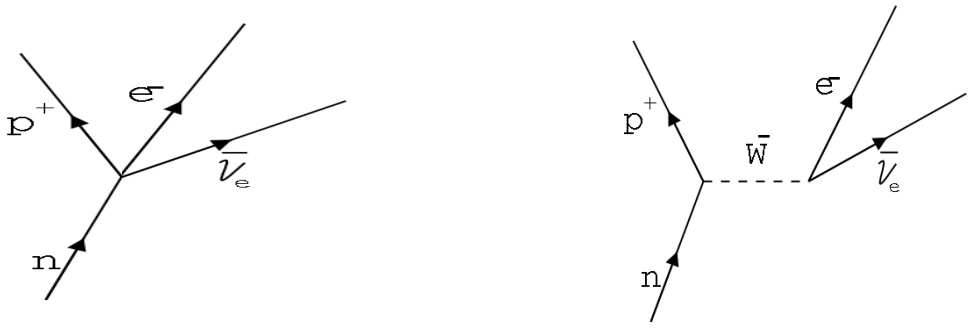

Figure 1.3. The description of neutron beta decay as a contact interaction (left). The description of a neutron beta decay according to the electroweak theory involving the exchange of a W^- boson (right).

one common constituent, the interaction between these constituents could be described as an effective four fermion contact interaction, as long as the collision energies between the particles remained well below the compositeness scale, M, which is usually denoted by Λ. The expression for a four fermion contact interaction, suppressed by the mass scale Λ, is a dimension 6 operator. It will therefore appear in the third term on the right-hand side of the Equation 1.1, and is consequently one of the possibilities for physics beyond the SM.

In this work, we have searched for evidence of 4-quark contact interactions, and therefore indirectly for evidence of quark compositeness, at the Large Hadron Collider (LHC) the

world's highest energy particle accelerator. The collisions at LHC began in 2009 at CERN, the European Center for Particle Physics in Geneva Switzerland. The LHC accelerates and collides beams of protons and beams of lead nuclei. The analysis described in this dissertation uses proton-proton data collected by the Compact Muon Solenoid (CMS) collaboration in 2011 when the total collision energy of the LHC was 7 TeV.

The goal of this work is to measure the transverse momentum (p_{T}) spectrum of jets, look for deviations of this spectrum from the prediction of the SM, and translate the experimental results into a statement about the existence, or otherwise, of 4-quark contact interactions.

Chapter 2 describes the parts of the SM that are relevant to the work, Chapter 3 describes the LHC and CMS experimental apparatus, Chapter 4 describes the event reconstruction, Chapter 5 describes the search for contact interactions and Chapter 6 contains a summary of this body of work. Appendix A contains the published documents of which I am the primary author.

CHAPTER 2

THEORY

The Standard Model (SM) is a compelling, consistent, computable theoretical framework that describes elementary fields and their interactions. The theory has been tested experimentally to high precision over the past decades. There are, however, strong arguments for why the SM cannot be the ultimate theory of nature. These arguments have inspired a wide range of new physics models to address the shortcomings of the SM. Some of these models predict quark compositeness, that is, that quarks like protons are composite particles. The subject of this dissertation is a search for evidence of quark compositeness. This chapter reviews the theoretical background and presents the motivation for the search.

2.1 Standard model

The Standard Model is a quantum field theory, based on a Lagrangian, that describes the electroweak and strong interactions between a set of fundamental fermion fields. The description of the electroweak and strong interactions are based on symmetries and the formalism of gauge theories. Each field exhibits quantized excitations that are interpreted as elementary particles. These elementary particles are divided into spin $\frac{1}{2}$ particles (leptons and quarks) that constitute matter and spin 1 particles (gauge bosons) that manifest the forces between the particles. Quarks are categorized based on their electric charge: as up-type ($Q = +\frac{2}{3}e$) and down-type ($Q = -\frac{1}{3}e$) quarks. The up-type quarks include the up (u), charm (c), and top (t) quarks, while the down-type quarks include the down (d), strange (s), and bottom (b) quarks. A simplified picture of all ordinary stable matter in the universe consists of electrons and quarks of the first generation (u, d, ν_e, e). The particles of the other two generations, (c, s, ν_μ, μ), and (t, b, ν_τ, τ), have identical properties to their first generation counterparts except for their masses. The leptons of the second and third

Table 2.1. The fermions of the SM, where "L" and "R" indices denote left and right chirality, respectively.

Fermions			
	1st generation	2nd generation	3rd generation
quarks	$\begin{pmatrix} u_L \\ d_L \end{pmatrix}$,$u_R$,$d_R$	$\begin{pmatrix} c_L \\ s_L \end{pmatrix}$, s_R, c_R	$\begin{pmatrix} t_L \\ b_L \end{pmatrix}$, t_R, b_R
leptons	$\begin{pmatrix} \nu_{eL} \\ e_L \end{pmatrix}$, e_R	$\begin{pmatrix} \nu_{\mu L} \\ \mu_L \end{pmatrix}$, μ_R	$\begin{pmatrix} \nu_{\tau L} \\ \tau_L \end{pmatrix}$, τ_R

generation are the muon ("μ") and the tau ("τ") as well as the corresponding neutrinos "ν_μ" and "ν_τ". The quarks of the second generation are charm ("c") and strange ("s"). The quarks of the third generation are top ("t") and bottom ("b").

The essence of the SM is that all fundamental interactions are a consequence of gauge invariance. The electromagnetic interaction follows from invariance under the $U(1)$ symmetry group with the electric charge as generator, while the relevant group for the weak interactions is $SU(2)$. $SU(2)_L$ transforms only the left-chiral parts of the fermion fields, denoted by the index L, consistent with the observed parity-violating nature of the weak interactions. As shown in Table 2.1, the left-chiral fermion fields are grouped into doublets, where flavor changes can only occur between the two states in one $SU(2)_L$ doublet. An example of flavor change: an electron transforms into an electron neutrino via emission of a W^-. Since the weak flavor eigenstates of fermions are different from their mass eigenstates, the $W^\pm$ can also couple to fermions of different generations. The physical bosons, γ and Z, correspond to a rotation in the $SU(2)$ flavor space by the Weinberg angle, θ_{W}, [3], where both Z and the photon couple to the left and right chiral states. The Standard Model incorporates three of the four fundamental interactions of nature: the electromagnetic, weak and strong interactions. Gravitational forces should also be included in the list of fundamental interactions. However, their impact on fundamental particle processes at the currently accessible energies is negligible. As noted, the fundamental interactions are mediated by gauge bosons. The neutral and massless photon (γ) is responsible for the

electromagnetic interaction acting between all electrically charged leptons and quarks. The heavy $W^{\pm}$ and Z^0 bosons mediate the weak interactions, which affect both the neutral and charged particles. Eight massless gluons (g), which are electrically neutral but carry color charge, are responsible for the strong interactions. Unlike leptons, quarks have color charge, allowing them to interact through the strong interaction in addition to the electromagnetic and weak interactions. The final critical component in the SM is the Higgs field, a neutral scalar field whose interaction with the other fields gives mass to them except for the photon and gluon fields. A Higgs like particle was discovered by the ATLAS and CMS Collaborations in July 2012 with a mass near 126 GeV [4, 5]. It has yet to be determined whether this particle is the postulated SM Higgs boson. However, current evidence supports this conclusion.

2.1.1 Key concepts of the Standard Model

In this section, we give a brief description of the main ideas of the Standard Model. Complete descriptions can be found elsewhere [6, 7]. The SM describes the electromagnetic, weak and strong interactions in terms of gauge theories. Gauge theories are quantum field theories for which the Lagrangian is invariant under some set of local transformations, separately valid at each space-time point, known as gauge transformations. These form a symmetry group of the theory. The quanta of the gauge fields are gauge bosons.

The Standard Model is a non-Abelian gauge theory, which means that the symmetry group is non-commutative. The Standard Model symmetry group is

$$SU(3)_{\mathrm{C}} \times SU(2)_{\mathrm{L}} \times U(1)_{\mathrm{Y}}, \tag{2.1}$$

where $SU(3)_{\mathrm{C}}$ is the symmetry group of the strong interactions with C being the associated conserved quantum number, color, and $SU(2)_{\mathrm{L}} \times U(1)_{\mathrm{Y}}$ describes the electroweak interaction, which unites the electromagnetic and weak interactions, where Y is the hypercharge and L indicates left-handed doublets. The conserved charge of $SU(2)$ is the weak isospin T, from which the electric charge Q is defined through the Gell-Mann-Nishijima formula $Q = T_3 + \frac{Y}{2}$ [8], with the third component of weak isospin written as T_3.

Electroweak interaction The electromagnetic interaction, described by Quantum Electrodynamics (QED), exists between all electrically charged particles and is mediated by

photons. The weak interaction is mediated by the $W^{\pm}$ and the Z^0 bosons and acts between quarks, charged and neutral leptons. The weak interaction also allows flavor-changing transitions of quarks and leptons. The electroweak interaction is described by $SU(2)_{\mathrm{L}} \times U(1)_{\mathrm{Y}}$ gauge group. The $U(1)_{\mathrm{Y}}$ group has one associated gauge field, B_μ, and its conserved quantum number is hypercharge Y. The $SU(2)_{\mathrm{L}}$ group has three gauge fields, A^a_μ where $a = 1, 2, 3$. The conserved quantity is the weak isospin T. The gauge fields B_μ and A^a_μ do not represent physical states. In this theory, all gauge bosons are massless. The photon and the gluons are indeed massless, however, the gauge bosons associated with the weak interactions are massive. To accommodate this fact, one could try adding a mass term for the gauge bosons to the Lagrangian. However, this violates the gauge invariance and leads to a non-renormalizable theory.

Strong interactions The strong interactions between quarks and gluons is described by Quantum Chromodynamics (QCD). QCD is a $SU(3)_{\mathrm{C}}$ gauge theory, invariant under local color transformations. The different color charges are typically referred to as blue, green and red. The local invariance introduces eight gauge fields, which correspond to the eight massless gluons that mediate the strong interactions. Since gluons carry color charge, they interact with quarks as well as with other gluons. The QCD Lagrangian can be written as,

$$\mathcal{L}^{\mathrm{QCD}}_{\mathrm{eff}} \left[\psi_f(\mathrm{x}), \bar{\psi}_{\mathrm{f}}(\mathrm{x}), \mathrm{A}(\mathrm{x}), \mathrm{c}(\mathrm{x}), \bar{\mathrm{c}}(\mathrm{x}); \mathrm{g}, \mathrm{m_f}\right] \;=\; \mathcal{L}_{\mathrm{invariant}} + \mathcal{L}_{\mathrm{gauge}} + \mathcal{L}_{\mathrm{ghost}}, \tag{2.2}$$

where: ψ_f denote quark fields, A the gluon field, c the ghost field, g the QCD strong coupling parameter and the parameters m_f allow for the possibility of non-zero quark masses, where f labels distinct quark fields. The $\mathcal{L}_{\mathrm{invariant}}$ is the classical Lagrangian density, invariant under local gauge transformations, $\mathcal{L}_{\mathrm{gauge}}$ is the Lagrangian gauge-fixing term, and $\mathcal{L}_{\mathrm{ghost}}$ ensures that gauge fixing does not spoil the unitarity of the physical scattering matrix that governs scattering of partons (quarks and gluons).

An important property of the strong interactions is the strength of the coupling constant (α_{s}). In order to compute observables, divergences that appear in the matrix element are regularized by introducing a cut-off to the momenta. The free parameters of the Lagrangian, such as the coupling constant, are then redefined, so that divergences no longer appear, which causes the coupling constant to become a function of an unphysical parameter called

the renormalization scale, μ_{R}. A reference value $\alpha(\mu_{\mathrm{R}}^2)$ has to be determined experimentally, which reflects the fact that the absolute scale of the coupling strength cannot be predicted by the SM. A typical choice for μ_{R} is the momentum transfer Q of the investigated process, such that $\alpha(Q^2)$ corresponds to the effective coupling strength in that process.

The QCD coupling parameter is given by [9]

$$\alpha_{\mathrm{s}}(Q^2) = \frac{12\pi}{(33 - 2n_f)\ln(\frac{Q^2}{\Lambda^2})}, \tag{2.3}$$

where n_f is the number of quark flavors, and Λ is defined by

$$\Lambda^2 = \mu_{\mathrm{R}}^2 \exp(\frac{-12\pi}{(33 - 2n_f)\alpha_s(\mu_{\mathrm{R}}^2)}). \tag{2.4}$$

The energy dependence of the strong coupling constant has two important consequences: asymptotic freedom and confinement.

Asymptotic freedom and confinement Asymptotic freedom refers to the decreasing interaction strength of the strong coupling parameter with increasing interaction energy. The result is that at high energies quarks and gluons can be treated as free particles. Confinement arises from the increasing interaction strength with increasing particle separation. The consequence is that the color charged particles such as quarks and gluons cannot exist as free particles but are confined to color-neutral composite particles (hadrons), for example mesons, containing a quark and an antiquark, or baryons, containing three quarks.

At the high energies of hadron colliders, quarks and gluons can be treated as free particles in interactions involving large momentum transfers. But quarks and gluons produced in the interactions do not appear as free particles in the detector because of confinement. Instead, they will appear as collimated collections of hadrons known as jets. The process of forming hadrons from the initial quarks and gluons is called hadronization. Although the strong interactions and asymptotic freedom are theoretically well described, the details of quark and gluon confinement are not fully understood [10]. The process of hadronization is similarly not a theoretically well understood process [9].

Higgs mechanism In the SM, the electroweak symmetry is broken through spontaneous symmetry breaking [11]. In spontaneous symmetry breaking, the Lagrangian remains invariant under the full symmetry group of the SM, while the lowest energy state, the vacuum,

is not invariant under the full gauge symmetry. Spontaneous electroweak symmetry breaking in the SM is governed by the Higgs mechanism [12]. The Higgs mechanism introduces four scalar fields written as a complex scalar doublet field, the Higgs field, $\phi = \frac{1}{\sqrt{2}}\begin{pmatrix} h_1 \\ h_2 \end{pmatrix}$. The scalar field is governed by a Lagrangian density with a global U(1) gauge symmetry. The vacuum state of the Higgs field lies on a circle in a complex two dimensional space described by $h_1^2 + h_2^2 = v^2/2$. The symmetry breaking occurs as the field ϕ acquires a non-zero vacuum expectation value (vev). Once the Higgs field acquires a vev, the gauge bosons gain mass through interactions with the Higgs field. Three of the fields of the Higgs doublet become the longitudinal components of three fields: the gauge bosons, $W^{\pm}$ and Z_μ^0. The vector field, A_μ, orthogonal to Z_μ^0 remains massless and is interpreted as the photon. The Higgs mechanism also provides mass to quarks and charged leptons via Yukawa interactions between the massless fermion fields and the Higgs field. The fourth field of the Higgs doublet emerges as a new massive scalar field, whose quanta are the Higgs bosons. The mass of the Higgs boson is not predicted by the theory.

2.1.2 Jets

The scattering process at the LHC can be classified as either hard or soft. Hard scattering, such as high p_{T} jet production, can be predicted with good precision using perturbation theory, however soft scattering, such as that which yields the underlying event, requires non-perturbative calculations. A key idea in QCD is factorization [13]. The factorization theorems show how to factorize long distance effects that cannot be calculated perturbatively from calculable short distance physics. The long distance physics is encapsulated in functions called parton distribution functions (PDFs) [13] that describe the distribution of partons in a hadron. These functions must be measured experimentally. The portion of the cross section that remains after the parton distribution functions have been factored out is the short distance cross section for hard scattering of partons. This portion of the cross section is perturbatively calculable.

First let us consider the proton-proton collision:

- Initially two hadrons, viewed as a collection of partons, collide.

Parton Model: The parton model [14] interprets hadrons as a collection of point like quasi-free particles. The model describes the cross section for high energy scattering of hadrons as an incoherent sum of the cross sections of the point like partons in a hadron. The three-quark-model of a proton, assumes that a proton is made of three free non-interacting valence quarks. However the picture is a bit more complex, since the valence quarks are embedded in a sea of virtual quark-antiquark pairs generated by the gluons which hold the quarks together. Partons are the collective name for quarks and gluons.

- Each parton can be characterized by a set of Parton Distribution Functions (PDFs).

  PDFs: The parton distribution functions give the probability densities to find a parton carrying a momentum fraction x of the proton at a given value of the square of the momentum transfer, Q^2. The number of partons goes up at low x with Q^2, and falls at high x. At high Q^2 there are a larger number of sea quark-antiquark pairs that carry a low momentum fraction x. The quarks and antiquarks carry about half of the nucleon momentum, while the remainder is carried by the gluons. The fraction of momentum carried by gluons increases with increasing Q^2.

- In a collision, particles that carry color charges can undergo bremsstrahlung emitting gluon radiation. Emissions that start from the two incoming colliding partons are called Initial-State Radiation (ISR). Emissions that are associated with outgoing partons are called Final-State Radiation (FSR).

- As partons recede, the color field strength increases, which causes the production of new quark-antiquark pairs in a process called hadronization.

  Hadronization: As the evolution of the event reaches $Q^2 \sim \Lambda_{QCD}$ [13], the coupling forces become significant and confinement takes place. This transforms all outgoing colored partons into colorless hadrons, a process that is modeled using fragmentation functions [15] that represent the probability of a parton to fragment into certain hadron final states. Many of these primary hadrons are unstable and decay further at various timescales. Those primary hadrons that are sufficiently long-lived

decay in the detector. There are several models of the hadronization process that attempt to connect the results of the parton shower with the final particle spectrum observed. These models are tuned using experimental observations. In this work, we use the string fragmentation model [16]. The string fragmentation model assumes a linear confinement, where the energy stored in the color field between quarks and antiquarks is assumed to increase linearly with the separation of color charges.

- Colliding protons are made up of a multitude of partons, so more than one parton may collide within a single proton-proton collision. The secondary collisions are referred to as multiple parton interactions (MPI). The additional products of the collision that are not explicitly related to the hard process of the collision: radiation, hadron remnants, products of multiple parton interactions, to list a few, are generally referred to as the underlying event.

QCD factorization As described above, a field theory of the strong interactions requires an energy-dependent coupling strength to harmonize the strength of the strong interaction at low energies with the weakness at high energy. This feature of the strong interactions is formalized in a factorization theorem, which states that the cross section, for example, for the production of a jet, can be factorized into two parts,

$$d\sigma(pp \to jet{+}X) = \sum_{ij} \int dx_1 dx_2 \overbrace{f_i^p(x_1,\mu_F) f_j^p(x_2,\mu_F)}^{\text{parton distribution functions}} \overbrace{d\hat{\sigma}(ij \to jet + X, x_1, x_2, Q^2, \mu_{\mathrm{F}}, \mu_{\mathrm{R}})}^{\text{partonic cross section}}, \tag{2.5}$$

where i and j run over the light quarks and gluons, f_i^p and f_j^p are parton distributions functions, $x_{1,2}$ are the fraction of hadron momentum carried by the parton i and j, respectively, $d\hat{\sigma}(ij \to jet + X)$ is the partonic cross section, μ_F is the factorization scale, and Q^2 is the hard scattering scale. Leaving the products, X, unspecified makes this process inclusive. Figure 2.1 shows a representation of a pp collision which results in a final state jet + X, where X can be any collection of particles. As Equation 2.5 shows, the hadronic cross section can be obtained by weighting the sub-process cross section with parton distribution

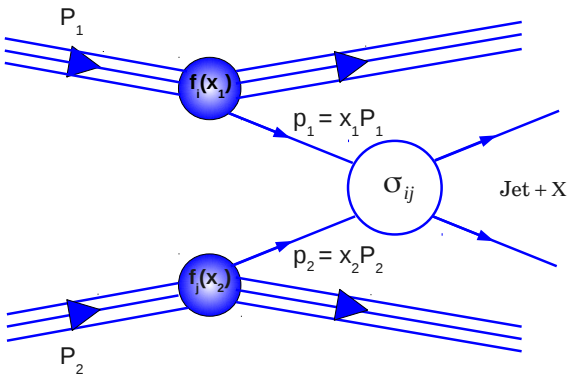

Figure 2.1. A pp collision which results in a jet + X, where X can be any collection of particles.

functions. These calculations showed very good agreement with the measured cross sections and confirmed the parton-model formalism. Problems seemed to arise when perturbative corrections were calculated from real and virtual gluon emissions. These calculations [9] showed large logarithms from gluons emitted collinearly with the incoming quarks, which seemed to spoil the convergence of the perturbative expansion. However, these logarithms were the same as those that arise in deep-inelastic scattering structure function calculations, and could therefore be absorbed into the definition of the parton distributions. It turned out that the finite corrections left behind after the logarithms had been factored into the PDFs were not universal and had to be calculated for each process separately [13].

Partonic cross section Perturbation theory can be used to calculate the partonic cross section. Perturbative predictions of the partonic cross section can be obtained by connecting the vertices, shown in Figure 2.2, and propagators derived from the Lagrangian, in all possible ways, using the Feynman rules. Predictions for collider experiments often require the computation of many thousands of Feynman diagrams. The simplest predictions can be obtained by calculating the lowest order in the perturbative expansion of the observable. The matrix elements are squared and integrated over the appropriate phase space. The diagrams with the smallest number of vertices contribute the most to the hard process. It is necessary

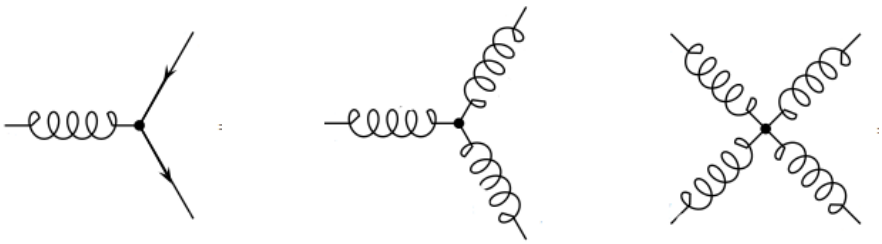

Figure 2.2. QCD Feynman diagrams for the quark-gluon vertex (left), the three-gluon vertex (center) and the four-gluon vertex (right).

to impose restrictions on the phase space in order to avoid divergences in the matrix elements. At each order in α_s, the strong coupling parameter, the cross section contains ultraviolet infinities that need to be removed in a procedure called renormalization. The perturbative prediction for the cross section, at finite order n, as well as α_s, depends on the factorization and the renormalization scales $\mu_{F,R}$ respectively, as shown in Equation 2.5. However, we expect that a complete calculation of the physical cross section would be independent of the choices of factorization or renormalization scales, which are artifacts of the calculation. In practice, since the calculations are always approximate there is, in general, a dependence of the calculated cross section on these scales. However, it is found that the dependence weakens as calculations are made more precise by going to higher order in α_{s}.

Parton distribution functions and factorization The calculations of the production cross sections at hadron colliders rely on the knowledge of the distribution of the momentum fraction x of the partons. The Q^2 dependence of the parton distribution functions (PDFs) is given by the Dokshitzer - Gribov - Lipatov - Altarelli - Parisi (DGLAP) QCD evolution equations [17]. The x dependence of the PDFs are obtained from global fits to data from deep-inelastic scattering, Drell-Yan and jet production. The factorization and renormalization scales for this work are set to $\mu_R = \mu_F =$ jet p_{T}.

2.2 Contact interactions

The understanding of PDFs at high parton momentum fraction over the past decade, has made it possible to consider the inclusive jet p_{T} spectrum as a competitive observable to

search for contact interactions. It has been 17 years since a comparable study was performed with this observable [18]. In this work, we consider the effective Lagrangian for the contact interaction model,

$$L = \zeta \frac{2\pi}{\Lambda^2}(\bar{q}_L\gamma^\mu q_L)(\bar{q}_L\gamma_\mu q_L), \tag{2.6}$$

where q_L denotes a left-handed quark field and $\zeta = +1$ or -1 for destructively or constructively interfering amplitudes, respectively. The amplitude for jet production is linear in λ, so the cross section of the k^{th} jet p_{T} bin, σ_k at leading order, is given by

$$\sigma_k \;=\; c_k + b_k\,\lambda + a_k\,\lambda^2, \tag{2.7}$$

where $\lambda \equiv 1/\Lambda^2$ and c_k, b_k, and a_k are jet p_{T}-dependent coefficients. The steps involved in measuring the inclusive jet p_{T} spectrum will be discussed in Chapter 5.

CHAPTER 3

LHC AND THE CMS DETECTOR

3.1 Large Hadron Collider

The Large Hadron Collider (LHC) [19] is built in a circular tunnel 26.7 km in circumference. The tunnel was constructed between 1984 and 1989 for the European Center for Particle Physics (CERN) Large Electron Positron machine. The tunnel is buried between 50 and 175 meters underground at the Swiss / French border on the outskirts of Geneva. The LHC is designed to collide two counter rotating beams of protons, inside a continuous vacuum system, guided by the field of 1232 dipole superconducting magnets, cooled by a huge cryogenics system. During 2011, the beams were made up of proton bunches spaced 25, 50 and 75 nanoseconds apart [20]. The protons in the bunches are obtained by removing electrons from hydrogen atoms, injecting the beam into the linear accelerator, LINAC2, then into the Proton Synchrotron Booster, then the Proton Synchrotron (PS), followed by the Super Proton Synchrotron (SPS), before finally reaching the Large Hadron Collider (LHC) [19]. At the interaction point each bunch, of 100 billion protons, is squeezed down to the width of a single human hair. At the luminosity of the LHC, prior to its long shutdown in early 2013, approximately 20 protons on average collided out of the 100 billion protons in each bunch. But, even with only 20 colliding protons per bunch, 600 million collisions occur per second. This is due to the very short time for bunch crossings. The LHC beam parameters, relevant to peak luminosity, for 2011 data [19], are shown in Table 3.1.

The total proton-proton cross section at 7 TeV is approximately 112 millibarns, with contributions from:

- inelastic (60 mbarn),

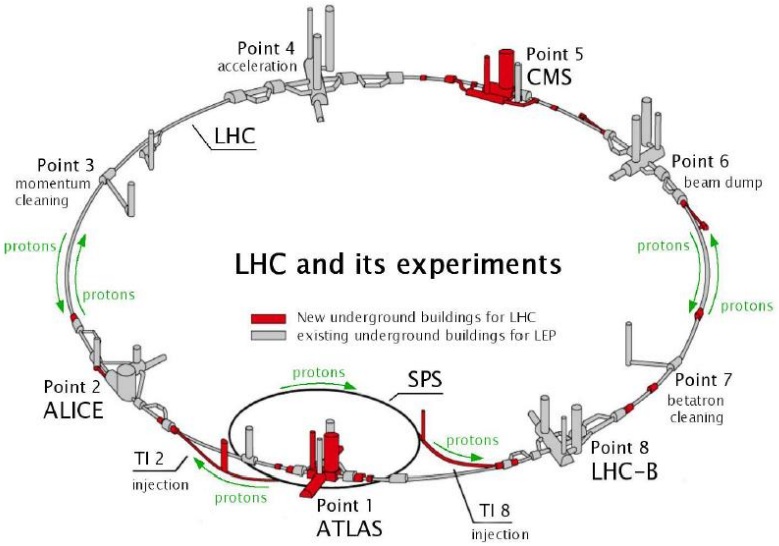

Figure 3.1. The Large Hadron Collider and its main detectors: CMS, ATLAS, LHCb, and ALICE.

Table 3.1. 2011 LHC beam peak luminosity design parameters.

Parameter	**Value**
Energy per proton beam	3.5 TeV
Number of particles per bunch	1.15×10^{11}
Number of bunches per beam	2808
Bunch spacing	25 ns
Bunch crossing rate	40 MHz
Peak luminosity	$1.0 \times 10^{34} \mathrm{cm}^{-2} \mathrm{sec}^{-1}$
Luminosity lifetime	14.9 hours

- single diffractive (12 mbarn),
- elastic (40 mbarn).

Elastic scattering of the protons and diffractive events will not be seen by the major components of the detector. It is only inelastic scatterings that gives rise to particles at sufficiently high angles with respect to the beam axis and therefore enter the major detector components.

Luminosity measures how many particles squeeze through a given area in a given time. At a proton-proton collider this can be expressed as:

$$L = \frac{f n_1 n_2}{2\pi\sqrt{\sigma_{x,1}^2 + \sigma_{x,2}^2}\sqrt{\sigma_{y,1}^2 + \sigma_{y,2}^2}}, \tag{3.1}$$

where f is the collision frequency, n_i is the number of protons in the bunch of beam i, and $\sigma_{\mathrm{x/y},i}$ is the transverse spread of beam i in the x and y directions. The total amount of data taken in a given time period is measured by the integrated luminosity, $\mathcal{L}$, which is defined by:

$$\mathcal{L} = \int L \, dt. \tag{3.2}$$

The luminosity, as determined from the CMS luminosity system is described in Ref. [21]. The total event rate per second for a physics process can be calculated from $R = \sigma L$, where σ is the cross section of the physics process and L is the luminosity of the collider. The first LHC

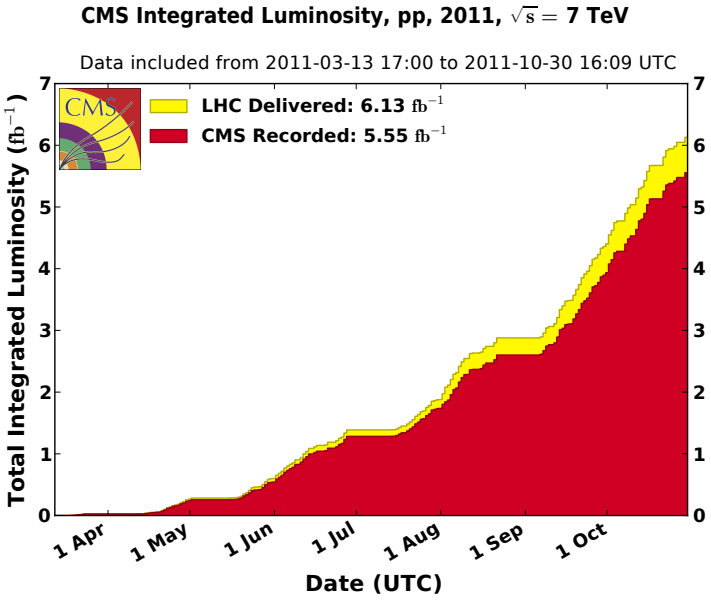

Figure 3.2. The integrated luminosity as a function of time, for 2011.

beams were circulated successfully on 10th September 2008. Unfortunately on the 19th of September, a serious fault developed damaging a number of superconducting magnets. The repair required a long technical intervention, providing beam again in November 2009. First collisions took place on 30th March 2010 with the rest of the year mainly devoted to

beam performance studies. 2011 was the first production year for collisions; the integrated luminosity for 2011 is shown in Figure 3.2.

At the LHC there are four main detectors: two general purposed detectors, the Compact Muon Solenoid (CMS) and A Toroidal Large Hadron Collider Apparatus (ATLAS), and two specialized detectors, the LHCb, which specializes in bottom quark physics, and ALICE, which is optimized to study heavy ion collisions.

3.2 Compact Muon Solenoid

The Compact Muon Solenoid (CMS) multi-purpose detector, shown in Figure 3.3, has a

Figure 3.3. The transverse view of the CMS detector during assembly.

diameter of 14.6 meters, a length of 21.6 meters, and a mass of 12.5 kilotonnes. Compact is a relative term; CMS is compact relative the ATLAS detector. A good description of the CMS detector requirements is given in the design specifications [22].

The main characteristics of the CMS detectors are:

- good muon identification and momentum resolution over a wide range of momenta and angles, good dimuon mass resolution ($\sim$1% at 100 GeV), and the ability to determine unambiguously the charge of muons with momenta, $p < 1$ TeV;

- good charged particle momentum resolution and reconstruction efficiency in the inner tracker. Efficient triggering and offline tagging of *taus* and b-quarks (requiring pixel detectors close to the interaction region);

- good electromagnetic energy resolution, good diphoton and dielectron mass resolution ($\sim$ 1% at 100 GeV), wide geometric coverage, π^0 rejection, and efficient photon and lepton isolation at high luminosities, and

- good missing transverse energy and dijet mass resolution, requiring hadron calorimeters with a large hermetic geometric coverage and with fine lateral segmentation.

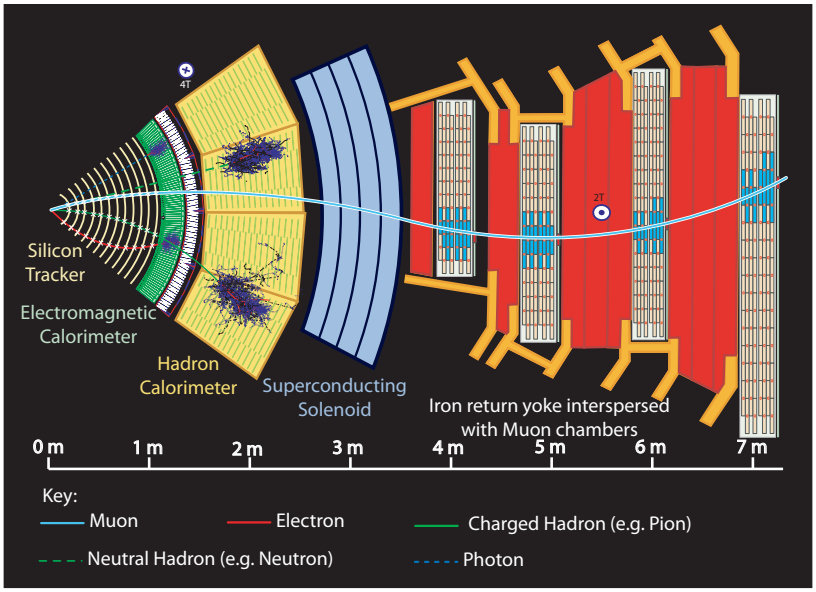

Figure 3.4. A slice of the transverse view of the CMS detector, showing particle trajectories traversing the detector material.

The coordinate system adopted by CMS has the origin centered at the nominal collision point, the y axis pointing vertically upward, and the x axis pointing radially inward toward the center of the LHC. The z axis points along the beam direction toward the Jura mountains from LHC point 5, see Figure 3.1. The azimuthal angle ϕ is measured from the x axis in the x-y plane and the radial coordinate in this plane is denoted by r. The polar angle θ is measured from the z axis. Pseudorapidity is defined as $\eta =$ -ln tan(θ/2)). The rapidity is defined as $y = 1/2\ \ln[(E + p_z)/(E - p_z)]$, where E denotes the energy and p_z is the

component of the momentum along the beam direction. In the limit of massless particles, $\eta = y$. The momentum and energy transverse to the beam direction are denoted by p_T and E_T, respectively. The imbalance of energy measured in the transverse plane is called missing transverse energy and is denoted by $\not\!\!E_T$.

The central feature of the CMS apparatus is a superconducting solenoid, of 6 meters internal diameter, operating with a magnetic field strength of 3.8 Tesla. Within the field volume are the silicon pixels, strip trackers, electromagnetic calorimeters (ECAL), followed by a brass-scintillator hadronic calorimeter (HCAL). The electromagnetic calorimeter and hadron calorimeter cells are grouped into towers, projecting radially outward from the origin. In the region $|\eta| < 1.74$, the barrel region, these projective calorimeter towers have segmentation $\Delta\eta = \Delta\phi = 0.087$, and the η and ϕ widths progressively increase at higher values of η. Figure 3.4 shows a transverse slice of the detector, with particle trajectories traversing the detector material. Further details about the CMS detector may be found elsewhere [23].

The large amount of data associated with collision events is impossible to store and process, therefore a dramatic rate reduction has to be achieved by choosing events of interest. This is obtained in two steps using two systems: the Level 1 Trigger [24] and the High Level Trigger (HLT) [25]. The Level 1 Trigger is based on custom and programmable electronics, while the HLT is implemented with software in a computer farm. The maximum allowed output rate for the Level 1 Trigger is 100 kHz. Level 1 Trigger uses information from the coarse segmentation of the calorimeters, the muon detectors, holding the high-resolution data in a pipeline until an acceptance or rejection decision is made. The HLT exploits all the data for each bunch crossing accepted by the Level 1 Trigger. Capable of complex calculations such as those done offline, the HLT algorithms typically undergo major changes as luminosity increases. The data from each event are processed through a world-wide computer network described in Appendix A.

CHAPTER 4

EVENT RECONSTRUCTION

This chapter describes the key elements of the CMS event reconstruction method. After hadronization, described in Chapter 2, and possible particle decay, the final state particles interact with the detector material differently for each type of particle. Each sub-detector has been designed to measure specific particle characteristics. By combining information from all sub-detectors one can make a more complete estimation of particle properties (see Section 4.1). These particles can be used to reconstruct jets, as described in Section 4.2, which are the objects used in this work.

4.1 Particle reconstruction

Particle Flow (PF) reconstruction, one of the CMS particle reconstruction methods, aims at reconstructing and identifying all stable particles by combining the information from all sub-detectors in an optimal determination of the particle's direction, energy and type. Particle Flow categorizes all particles into five types: muons, electrons, photons, charged and neutral hadrons. The list of particles is then used to build jets, determine the missing transverse energy, reconstruct and identify taus, quantify charged lepton isolation with respect to other particles and tag b-jets.

The reconstruction of each particle is based on a combination of one to three particle flow elements from various sub-detectors:

- charged-particle tracks,
- calorimeter clusters, and
- muon tracks.

These elements must be identified with high efficiency and low fake rate (i.e., false identification rate) in a high-track density environment. This task is accomplished by using an iterative tracking algorithm, described in Section 4.1.1, and the calorimeter clustering methods described in Section 4.1.2. The PF elements are used with a so-called link algorithm, described in Section 4.1.3, which fully reconstructs each particle object, while at the same time getting rid of possible double counting from different sub-detectors.

4.1.1 Iterative tracking algorithm

An iterative tracking strategy was adopted to achieve both high efficiency and a low rate of fake tracks. The iterative tracking steps are:

- Seed tracks with an initial track candidate, then reconstruct the track using tight (i.e., strict) criteria to reduce the track fake rate.

- Loosen the seeding criteria such that unambiguously assigned data from the previous iteration can be removed. The looser seeding criteria increase the tracking efficiency, while the removal of hits allows the fake rate to be kept low because of reduced combinatorics. During the first three iterations, tracks originating from within a thin cylinder around the beam axis are found with an efficiency of 99.5% for isolated muons and larger than 90% for charged hadrons in jets.

- The fourth and fifth iterations have relaxed constraints on the vertex. This allows for the reconstruction of secondary charged particles originating from photon conversions and nuclear interactions in the tracker material and from the decay of long-lived particles such as K^0_S.

The early steps have stricter requirements on tracks originating from the production vertex while the later steps have stricter requirements on the track quality. With this iterative technique, charged particles with as little as three hits, a p_T as small as 150 MeV and a vertex more than 50 cm away from the beam axis, are reconstructed with a track fake rate on the order of 1%.

4.1.2 Calorimeter clustering

The clustering algorithm was developed specifically for PF event reconstruction. The purposes of the algorithm are to:

- Detect and measure the energy and direction of stable neutral particles such as photons and neutral hadrons.
- Separate neutral particles from energy deposits due to charged hadrons.
- Reconstruct and identify electrons and all accompanying bremsstrahlung photons.
- Improve the energy measurement of charged hadrons for which the track parameters are not determined accurately, such as is the case for high-p_{T} tracks.
- Clearly separate energy deposits, which are in close proximity.

The clustering is performed separately in each sub-detector except the forward hadron calorimeter. The steps of the algorithm are:

1. Identify cluster seeds, defined as local maxima of energy in the calorimeter.
2. Grow clusters from the seeds by aggregating cells with at least one side in common with a cell already in the cluster and with energy in excess of a given threshold. These thresholds equal two standard deviations of the electronic noise: 80-300 MeV in the electromagnetic calorimeter and 800 MeV in the hadron calorimeter. The clustering algorithm gives rise to as many PF clusters as there are cluster seeds.
3. The calorimeter granularity is exploited by sharing the energy of each cell among all particle-flow clusters according to the cell-cluster distance, with an iterative determination of the cluster energies and positions.

4.1.3 Link algorithm

A link is measured in η and ϕ between any two elements in the event. The link algorithm [26] quantifies the connection quality between elements and creates blocks of

elements, linked directly or indirectly. The blocks contain one, two or three elements, and constitute inputs for the particle reconstruction and identification algorithm.

An example of the linking process between a charged particle track and a calorimeter cluster is as follows:

- The track is first extrapolated from its last measured hit in the tracker to the two layers of the electromagnetic calorimeter, and to the hadron calorimeter to a depth corresponding to one interaction length, typical of a hadron shower.
- The track is linked to one or more clusters in the calorimeter if the extrapolated position on the track lies within the cluster boundaries.
- The link distance is measured in the (η, ϕ) plane between the extrapolated track position and the cluster position.
- Tangents to the tracks are extrapolated to the electromagnetic calorimeter from the intersection points between the track and each of the track layers in order to collect the energy of all bremsstrahlung photons emitted by electrons.
- A cluster arising from a potential bremsstrahlung photon is linked to the track if the extrapolated tangent position is within the boundaries of the cluster.
- A link is established between the hadron calorimeter and the electromagnetic calorimeter.

In a similar fashion, links are made between tracks in the tracker and in the muon system.

4.1.4 Particle identification

Once the blocks are created, particles can be identified from each block of elements. The resulting list of reconstructed particles constitutes a global description of each event.

The following describes the algorithm which loops over each block, reconstructing particles:

- **Muons**: A PF candidate will become a muon when its momentum is within three standard deviations of that determined from the tracker alone. The corresponding track

is removed from the block. The energy deposited in the calorimeters was measured using cosmic rays.

- **Electrons**: Electrons tend to give rise to short tracks and to lose energy by bremsstrahlung in the tracker layers on their way to the calorimeter. Tracks are refit [26] in an attempt to follow their trajectories to the calorimeter. Electrons are identified by combining a number of tracking and calorimetric variables into a multivariate discriminant. The corresponding track and calorimeter clusters are then removed from the block.

- **Charged hadrons**: Tighter quality criteria are applied to the remaining tracks. These criteria require the relative uncertainty on the measured p_{T} be smaller than the relative calorimetric energy resolution expected for charged hadrons. This requirement rejects 0.2% of the tracks used for hadronic jets. However, out of the 0.2%, 90% are rejections of fake tracks. The hadron's energy is measured independently with more precision, by the calorimeters.

- **Photons and neutral hadrons**: The calibrated energy of the closest ECAL and HCAL clusters linked to the track(s) can be significantly larger than the total associated charged-particle momentum. If the relative energy excess is found to be larger than the expected calorimeter energy resolution, the cluster energy gives rise to a photon, and possibly to a neutral hadron. Precedence is given to photons over neutral hadrons in the ECAL, due to the observation that, in jets, 25% of the jet energy is carried by photons, while neutral hadrons carry only 3% of the jet energy.

There are rare cases where the total calibrated calorimetric energy is still smaller than the total track momentum by a large amount. When the difference is larger than three standard deviations, a relaxed search for muons and for fake tracks is performed. All muons, identified in both the tracker and the muon detector, which are not already selected by the algorithm and for which an estimate of the momentum exists with precision better than 25% are treated as muons. The redundancy of the measurements in the tracker and the calorimeter allows a few more muons to be found without increasing the fake-muon rate. This redundancy is

further exploited by progressively removing tracks from the block ordered according to their measured p_{T} uncertainty. The process stops either when all the tracks with a p_{T} uncertainty in excess of 1 GeV have been examined, or when the removal of a track would render the total track momentum smaller than the calibrated calorimetric energy.

Each of the remaining tracks in the block is presumed to be due to a charged hadron. If the calorimetric energy is comparable with the track momentum within uncertainties, the charged-hadron momenta are redefined by a fit of the measurements in the tracker and the calorimeters. This combination is relevant at very high energies where the track parameters are measured with larger uncertainties.

4.2 Jet reconstruction

Jets are produced when high-energy quarks or gluons from the colliding proton-proton scatter. Each of the outgoing quarks or gluons materializes as a jet of particles with its momentum distributed among the particles of the jet, shown in Figure 4.1. There are several types of jet, however this study is limited to two: particle flow jets (PFJets) and calorimeter jets (CaloJets), as described in Section 4.2.2. CaloJets use energies deposited in the calorimeter to reconstruct jets, while PFJets use particles to reconstruct jets.

4.2.1 Characteristics

On average, high p_{T} jets are narrower compared with low p_{T} jets: at 20 GeV ∼15% of the jet p_{T} is distributed in a radius of 0.1 $\eta \times \phi$ space around the initial parton while the fraction increases to ∼90% at 600 GeV. The properties of a jet's constituents depend on the initial parton type (jet flavor). Due to color factors, the parton emission rate of gluons is about twice as large as that of quarks. Gluons typically produce a higher multiplicity of softer particles during showering than quarks, which leads to broader jets [27].

4.2.2 Jet types

Calorimeter jets Calorimeter jets (CaloJets) are reconstructed from energy deposits in the calorimeter towers. A calorimeter tower consists of one or more hadron calorimeter cells

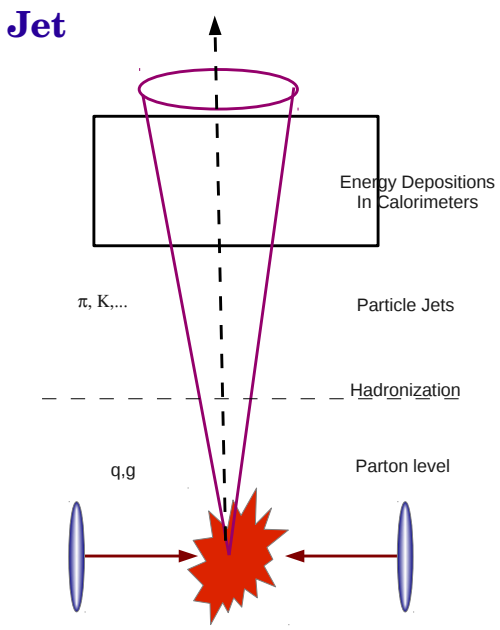

Figure 4.1. A jet is produced when high-energy quarks or gluons from the colliding proton-proton scatter. Each of the outgoing quarks or gluons materializes as a jet of particles with its momentum distributed among the particles of the jet. The particles of the jet leave energy depositions in the calorimeters.

and the corresponding electromagnetic calorimeter crystals. Specifically, in the central region of the detector, which is referred to as the barrel, a projective calorimeter tower is made up of the unweighted sum of a single hadron calorimeter cell and 5×5 array of electromagnetic calorimeter crystals. The association between calorimeters is more complex in the endcap regions. In the forward region, a different calorimeter technology is employed, which uses the light signals collected by short and long quartz readout fibers to aid the separation of electromagnetic and hadronic signals. A 4-momentum is associated with each tower deposit above a certain threshold, assuming zero mass, where the direction is the tower's angular position as seen from the interaction point.

Particle flow jets Particle-flow (PF) jets are clustered from the 4-momenta of the particle candidates reconstructed as described in Section 4.1. PF jets have superior performance compared to calorimeter jets in terms of response and resolution. One of the

main reasons is due to the hadron calorimeter where only about 15% of the jet energy is distributed among neutral hadrons [26]. Since particle candidates are used, the impact from the calorimeter non-linearity is also reduced. The typical energy fractions carried by charged particles, photons and neutral hadrons in jets are 65%, 25%, and 10%, respectively. These fractions ensure that 90% of the jet energy can be reconstructed with good precision by the particle-flow algorithm, while only 10% of the energy is affected by resolution and calibration corrections. As a consequence, jets made of reconstructed particles are similar to jets made of Monte Carlo generated particles, more so than jets made solely from calorimetric information. The reconstructed jet object properties include: energy, E, defined as the scalar sum of the constituent energies, momentum, $\overrightarrow{p}$, defined as the vector sum of the constituent momenta, and the transverse momentum, p_{T}, the component of the jet $\overrightarrow{p}$ in the transverse plane.

4.2.3 Clustering algorithm

The jets used in this work are reconstructed using the particle flow reconstruction method [26] and the anti-k_T algorithm [28]. The anti-k_T algorithm can be applied to calorimeter towers, particles or partons. A jet clustering algorithm associates objects based either on proximity in coordinate space or in momentum space. In this study, we use the anti-k_T algorithm with distance parameters of $D = 0.5$ and 0.7. The k_T algorithms are massless four-momenta clustering algorithms in momentum space, which have the virtue of being less sensitive to higher order perturbative QCD effects [29, 30, 31]. The k_T algorithms are based on pair-wise successive combinations of objects. The quantities $k_{T,i}^2 = p_{T,i}^2$ and $k_{T,(i,j)}^2 = \min(p_{T,i}^{a\times 2}, p_{T,j}^{a\times 2})\Delta R_{i,j}^2/D^2$ are computed for each object, where $p_{T,i}$ is the p_T of the i^{th} object, $\Delta R_{i,j}$ is the distance in (η,ϕ)-space between objects i and j and D is the parameter that controls the size of the object. The parameter $a = 1$ defines the k_T algorithm, and $a = -1$ defines the anti-k_T algorithm. When $k_{T,i}^2 < k_{T,(i,j)}^2$ for the i^{th} object, it is considered to be a jet and removed from the list of objects. When $k_{T,i}^2 > k_{T,(i,j)}^2$, the two objects are merged into a single object and the two original ones are removed from the list. The process is iterated until all objects become jets. The anti-k_T algorithm is infrared and collinear safe [32].

4.2.4 Jet energy scale corrections

The Jet Energy Scale Corrections (JEC) are chosen so that, on average, the p_T of a corrected jet is equal to the p_T of the corresponding particle level jet, that is, a jet prior to its interaction with the detector. These corrections are derived from MC and data driven methods as a function of the jet p_T and η, using dijet and photon/Z+jet p_T balancing [33]. The correction is applied as a multiplicative factor to the uncorrected jet p_T. CMS has 7 correction steps, however this search used the first three steps only. They are: L1 Pile up correction, L2 Relative jet correction, L3 Absolute jet correction [34]. [1]

[1]To access the JEC for this analysis, we use data keys: GR_R_42_V19 with JEC ak7PFL1FastL2L3.

CHAPTER 5

ANALYSIS

This chapter describes my search for contact interactions using the inclusive jet p_{T} spectrum in pp collisions at $\sqrt{s} = 7$ TeV. We begin with a description of the data used in our analysis. This is followed by a description of the models used to interpret the data, our results, and our interpretation of these results in terms of limits on the compositeness scale Λ.

5.1 Data

This section covers the data sets used in this work, the data quality and the data selection.

5.1.1 Data sets

The names of the data sets used in this work are listed in Table 5.1. A description of the format of the reconstructed data can be found in Appendix A.

Table 5.1. The CMS 2011 data sets used in this analysis.

Run Name	Run Numbers	Integrated Luminosity [pb^{-1}]
Run2011A	160329-163869	215
Run2011A	165071-168437	930
Run2011A	170053-172619	370
Run2011A	172620-173439	660
Run2011B	175000-180252	2490

In 2011, the data collection period was divided into two data eras: Run 2011A and Run 2011B. Run 2011A started in March and ended in August, while Run 2011B started in

September and ended in October. Out of an integrated luminosity of 4.6 fb^{-1}, 2.0 fb^{-1} was collected in Run 2011A and 2.6 fb^{-1} was collected in Run 2011B. Since the LHC luminosity rapidly increased over the year, Run 2011B was shorter than Run 2011A but more data were collected. The average number of pile-up events, see Section 5.1.2, increased from 5.5 in Run 2011A to 9.2 in Run 2011B.

5.1.2 Data quality

Some basic distributions, after the selection criteria described in Section 5.1.4 have been applied, are shown in the following figures. Figure 5.1 shows the photon energy fraction and the neutral hadronic energy fraction. Figure 5.2 shows the electron energy fraction and the charged hadronic fraction. An energy fraction is the object's energy in each sub-detector / total energy of the object.

Figure 5.3 shows the multiplicity distribution of charged hadrons, photons, muons, and electrons, reconstructed using the particle flow method described in Chapter 4. Figure 5.4 shows the multiplicity distribution of primary vertices, that is, the distribution of the number of vertices per beam crossing. Our selection criteria are indicated by the green and red vertical lines.

Pile-up During the majority of the 2011 data taking period, the LHC operated with 1380 bunches per beam with a nominal bunch crossing of 50 nanoseconds. In Figure 5.4, on average, 5.5 pp collisions occur per bunch crossing, an effect referred to as pile-up. Pile-up is a byproduct of high luminosity and poses significant challenges. As the luminosity increases, so does the pile-up. The challenge is to assign data to the correct pp interaction. In principle, pile-up could affect the jet p_{T} spectrum. In order to determine whether this is the case, we studied the dependence of the spectrum on the number of primary vertices. The left plot of Figure 5.5 shows the normalized jet p_{T} spectra for events with either 1 to 5 or 6 to 40 primary vertices. The right plot of the same figure shows the ratio of these spectra relative to the spectrum using all events. The spectrum is seen to be unaffected by pile-up.

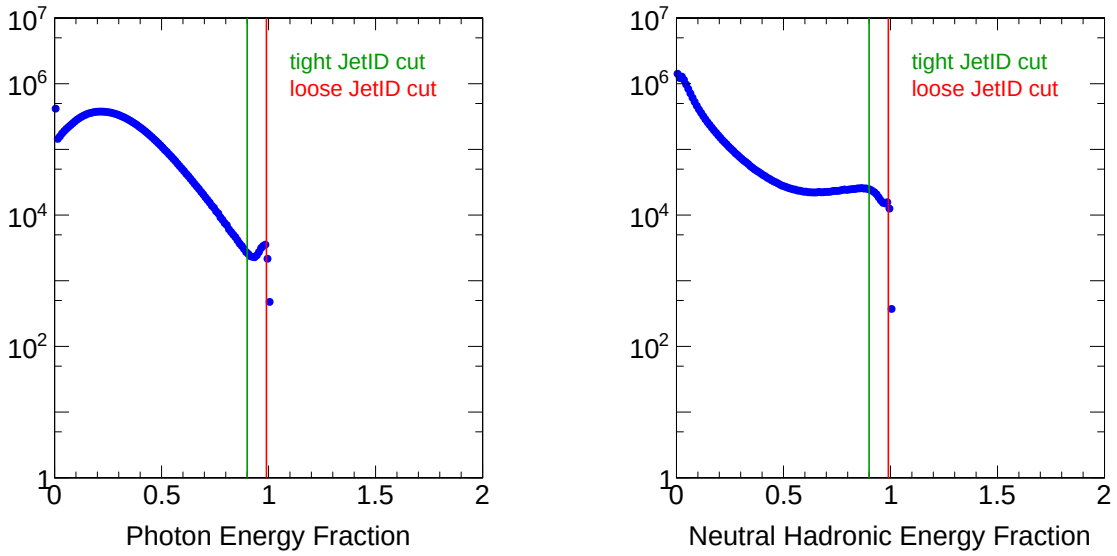

Figure 5.1. The photon energy fraction (left) and the neutral hadronic energy fraction (right).

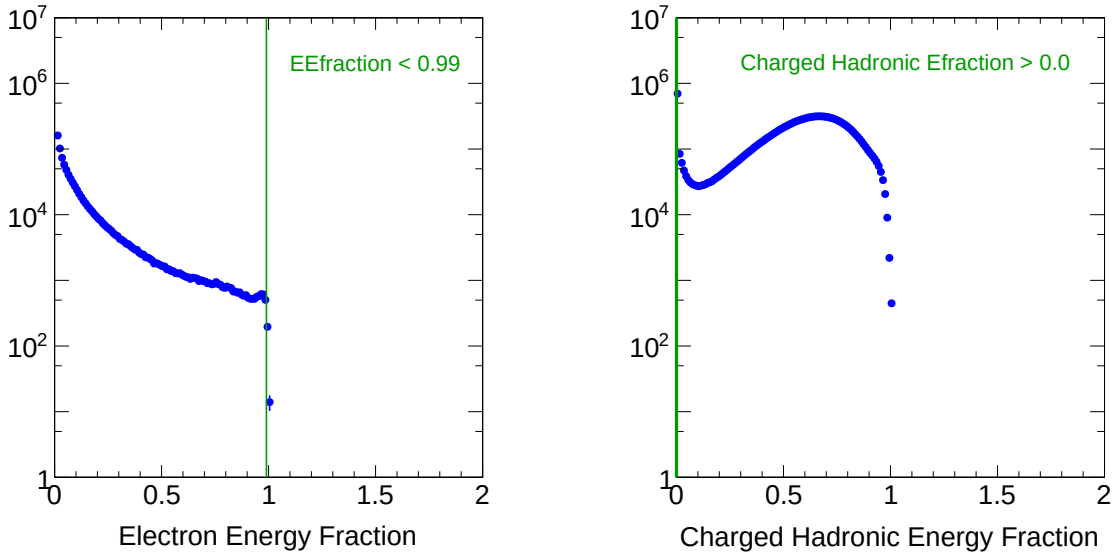

Figure 5.2. The electron energy fraction (left) and the charged hadronic energy fraction (right).

5.1.3 Data selection

Even though the CMS detector does an excellent job of collecting collision data (see Figure 3.2), not all sub-detectors were always fully functional. After collision data are

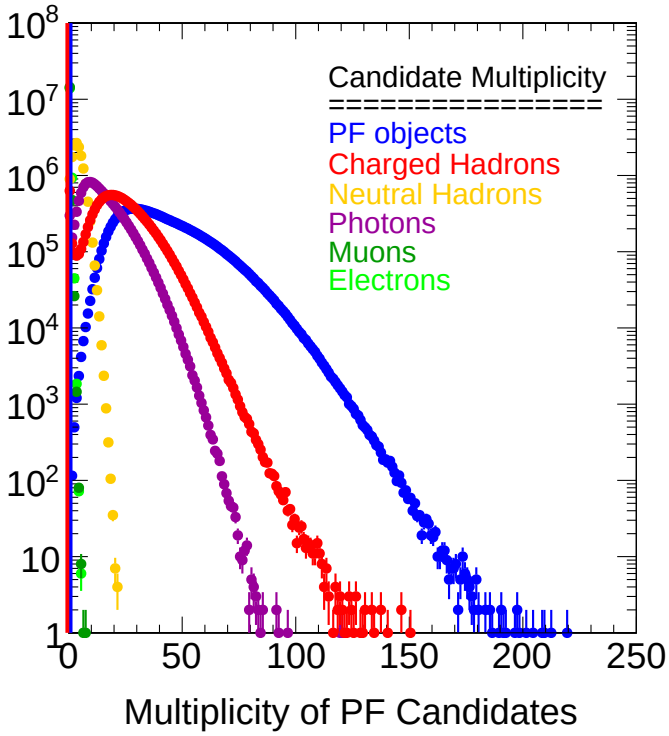

Figure 5.3. The particle flow candidate multiplicity for all five particle flow candidates, and the overall multiplicity of candidates.

collected, prior to physics analyses the data's quality is quantified. Good data are marked using an identifier called a *reference key*, which is created for the purpose of event selection depending on the type of physics analysis being performed. CMS records these keys in text files called JSON files. The acronym JSON stands for JavaScript Object Notation (JSON), which is a lightweight, software independent, text formatted notation, built on two structures: the first, a collection of name-value pairs and the second, an ordered list of values. This work uses the following JSON files to select data characterized as good:

- Cert_160404-163869_7TeV_May10ReReco_Collisions11_JSON_v3.txt,
- Cert_160404-180252_7TeV_PromptReco_Collisions11_JSON.txt,
- Cert_170249-172619_7TeV_ReReco5Aug_Collisions11_JSON_v3.txt,

where the naming convention is as follows: certified, run range, center-of-mass energy, data era, collision year, format type, iteration.

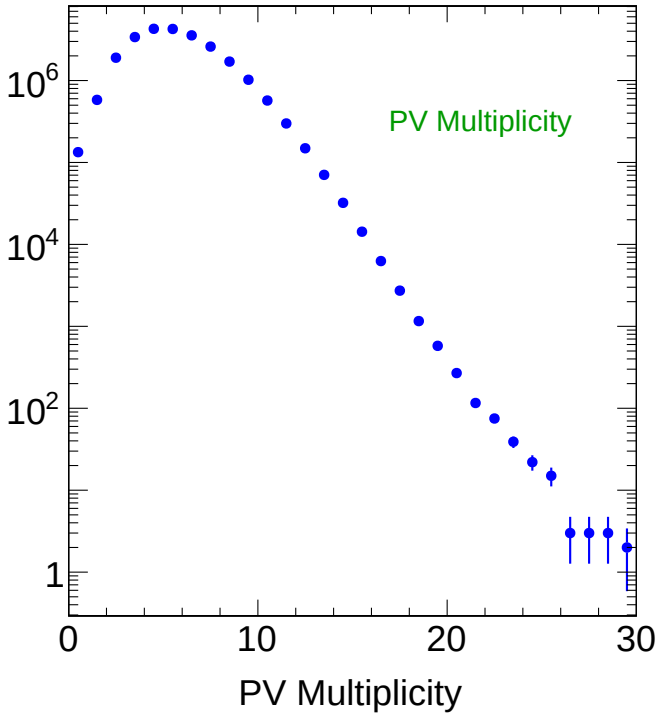

Figure 5.4. The primary vertex (PV) multiplicity distribution during Run2011A with, on average, 5.5 *pp* collisions per bunch crossing.

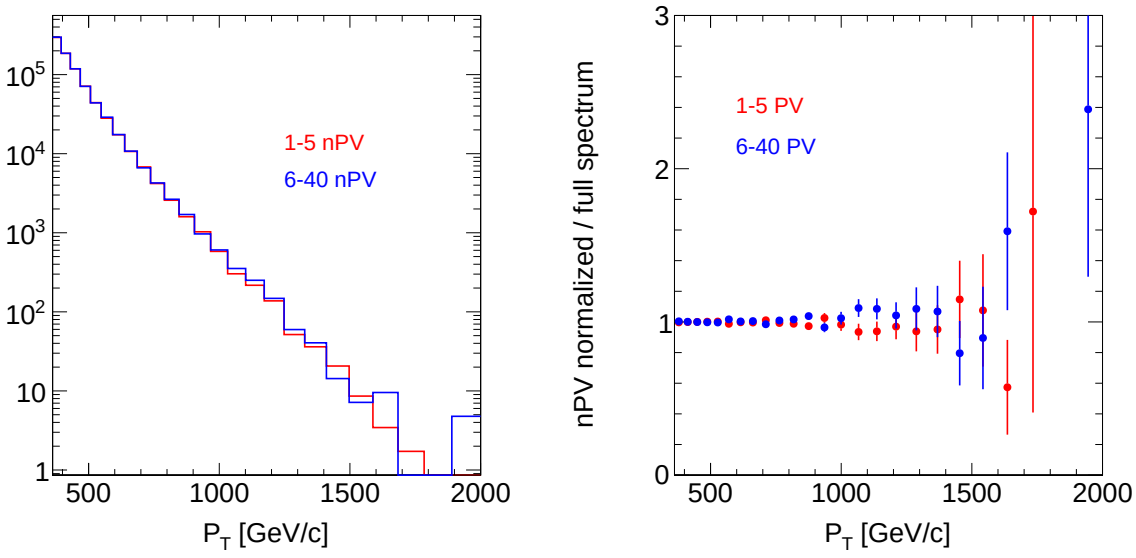

Figure 5.5. The normalized jet p_{T} spectra for events with either 1 to 5 or 6 to 40 primary vertices (left). The ratio of these spectra relative to the spectrum using all events (right).

Jet triggers Once good data are identified using the information in the JSON files, events are selected that satisfy a set of high level jet triggers (HLT_Jet). These triggers select events with at least one jet that has a transverse momentum above a specified value. The triggers used in this work are listed in Table 5.2. The version, v, of the trigger changes

Table 5.2. The high level jet triggers are listed, where the Jet240 notation describes the selection of an event which has at least one jet with a $p_{\mathrm{T}} > 240$ GeV.

Jet triggers	
240 GeV p_{T}	300 GeV p_{T}
HLT_Jet240_v1	HLT_Jet300_v1
HLT_Jet240_v2	HLT_Jet300_v2
HLT_Jet240_v3	HLT_Jet300_v3
HLT_Jet240_v4	HLT_Jet300_v4
HLT_Jet240_v5	HLT_Jet300_v5
HLT_Jet240_v6	

during data collection because of processing and storage limits. In order to maintain specific triggers for physics analyses as the signal bandwidth increases, only a portion of the events are recorded. This is achieved using "prescales". A trigger with a prescale value of 1 records all events passing the trigger. For a trigger with a prescale of n, only 1 in n triggered events are recorded. This work uses events with at least one jet per event and non-prescaled triggers, that is, triggers with a prescale value of 1. Figure 5.6 shows that the trigger efficiency for these triggers becomes independent of p_{T} above a jet p_{T} threshold of $\sim$ 400 GeV. This is important because the predicted spectra with which the observed spectrum is compared do not have to be corrected for trigger efficiency.

Jets are binned in a commonly used p_{T} binning shared among CMS inclusive-jet analyses. The jet p_{T} bin widths increase with jet p_{T}, corresponding approximately to the jet p_{T} resolution as a function of p_{T}. Figure 5.7 shows event displays featuring some of the highest p_{T} jets in our event sample.

5.1.4 Jet identification

Not all reconstructed jets are physics objects. The jets due to detector noise need to be rejected. Even though there are several algorithms implemented to reject noise at the

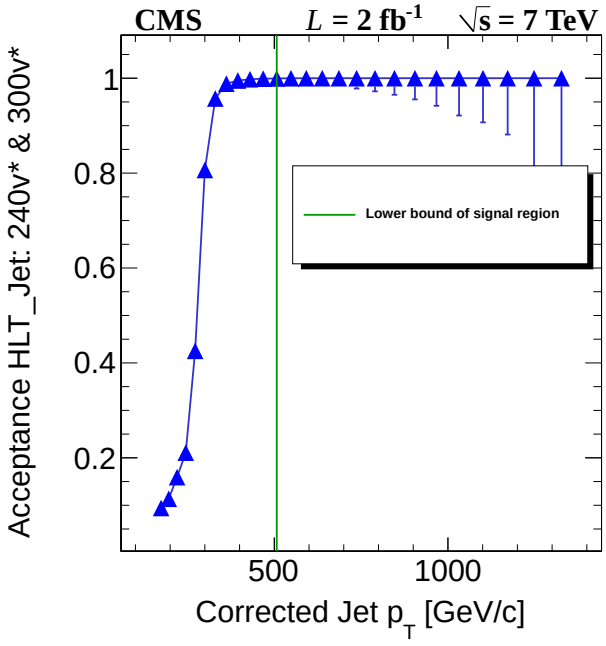

Figure 5.6. The efficiency of the HLT_Jet240v∗ and HLT_Jet300v∗ jet triggers, with a prescale of 1.0, for 2011 data as a function of the corrected jet p_{T}. The trigger becomes fully efficient at $\sim$ 400 GeV.

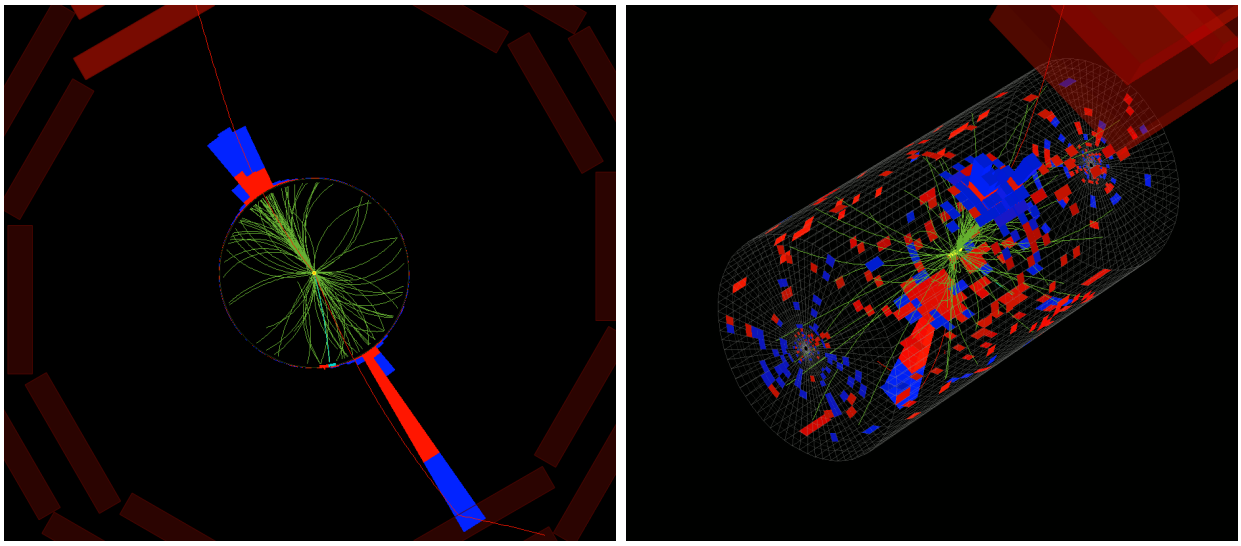

Figure 5.7. Two jets with jet p_T of 1921 and 1893 GeV in one event, shown with ρ ϕ view (left) and 3-d view (right).

detector level, not all cases reject the noise before the jet object is created. Jet identification is introduced to reject fake jets.

Jet background noise The main background event clean up method used in this analysis is the HCAL noise filter [35]. There are three main types of sporadic noise within the hadron calorimeter:

1. Hybrid PhotoDiode (HPD) Noise: misalignment between the electric field within an HPD and the external magnetic field can lower the voltage of the HPD, which results in occasional cascades where most of the 18 channels within a HPD report large energy deposits.

2. Single readout box (RBX) (electronics for data collection) noise: when signals from HPDs or photomultiplier tubes (PMTs) are digitized and most of the RBX channels report large energy deposits.

3. PMT Window Noise: charged particles can occasionally hit a PMT window directly.

There are three types of HCAL noise filter: loose, tight, and high-level. We use the loose HCAL noise filter in this analysis. If an event passes the loose noise filter the following is true:

1. all RBXs with more than 25 GeV of energy contain at least 70% of their total signal within 2 bunch crossings;

2. the reconstructed time falls within [-7, +6] ns of the trigger, and

3. the maximum number of channels reporting exactly 0 ADC counts within an RBX is fewer than 8 (a large number of 0 values is an indication of a noise-related RBX problem).

In order to filter out jets with background noise, we select events with at least one primary vertex and one jet, using the following requirements:

1. Events must pass the loose HCAL noise filter,

2. have a good primary vertex,

   (a) two or more good tracks,

(b) interactions are close to the geometric center of the detector ($|z|$ position ≤ 24 cm and $\rho = \sqrt{x^2 + y^2} \leq 0.2$ cm),

(c) and the jet is determined not to be a fake jet.

There are two types of jets used in our analysis, calorimeter jets (CaloJets) and particle flow jets (PFJets):

Calorimeter jet criteria

1. Electromagnetic energy fraction of a jet > 0.01 OR CaloJet $|\eta| > 2.6$

   Less than 90% of the jet energy is contained in a single calorimeter hit.

2. Tight jet criteria

   Less than 95% of the measured jet energy is associated with a single Hybrid PhotoDiode when the jet $p_{\mathrm{T}} > 25$ GeV.

Particle flow jet criteria

1. Number of particles > 1
2. Number of charged hadrons > 0
3. Charged hadronic energy fraction > 0
4. Electron energy fraction < 0.99
5. Corrected jet $p_T > 395$ GeV
6. $|y| < 0.5$
7. Tight Jet criteria
   (a) Neutral hadronic energy fraction < 0.90
   (b) Photonic energy fraction < 0.90

More details of the jet identification criteria can be found in Ref. [36].

5.2 Models

In this section, we describe the simulated data and models used in our analysis and the statistical interpretation of our results in terms of these models. As noted in Chapter 2, at leading order (LO) the amplitude is linear in $\lambda = 1/\Lambda^2$. Therefore, the LO cross section will depend on λ quadratically. In this analysis, we have chosen to calculate the QCD part of the cross section at next-to-leading (NLO) order, but to parametrize deviations from the QCD prediction using the LO contact interaction (CI) model; that is, we use cross section models of the form $\mathrm{QCD}_{\mathrm{NLO}} + \mathrm{CI}(\Lambda)$. In the following sections, we describe some of our studies of the CI model and we give details of the QCD + CI models.

5.2.1 Studies of contact interaction models

We use Pythia 6.422 [37], tune Z2, to model the inclusive jet p_{T} spectrum with, and without, contact interactions. A Pythia tune is a particular adjustment of the program's parameters in order to achieve a good match between the predictions of Pythia and data for a few standard processes. The meaning of the mass scale Λ is defined by the contact interaction model in Pythia. The Pythia configuration is given in Appendix C.

Since the jet p_{T} spectrum is extremely steep (it falls faster than p_{T}^{-5}) we produce simulated events in different jet p_{T} bins, to ensure that the high p_{T} bins are well-populated with events. Once the samples have been generated, events must be re-weighted by cross section / number of events generated in order to obtain the correct spectral shape. New physics such as quark compositeness or some new interaction at a high scale, Λ, can be modeled by a contact interaction at a scale much lower than Λ. The effects of contact interactions are predicted to be the largest at low jet pseudo-rapidity [38, 39, 40, 41].

In principle, an analysis could be based on both pseudo-rapidity and p_{T}. We investigate the predicted differential cross sections by generated models with $\Lambda = 3$ TeV for $|\eta| <= 3$ and jet p_{T} in the range $500 \leq p_{\mathrm{T}} \leq 2000$ GeV. The differential distributions are shown in Figure 5.8. We find that limiting our search region to $|\eta| < 0.5$ provides the best signal to noise ratio.

As noted, the cross section σ_k in the kth jet p_{T} bin is given by

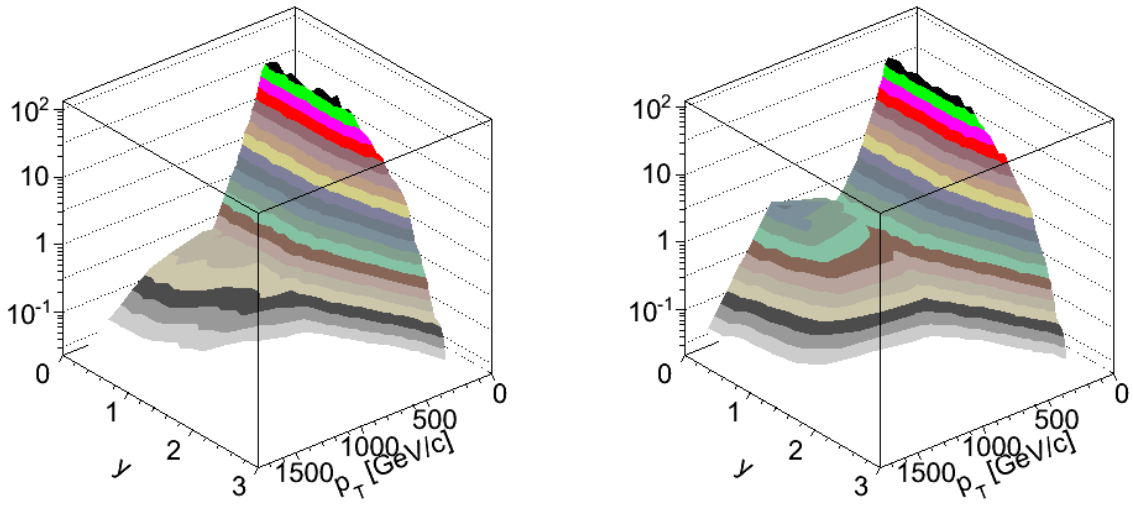

Figure 5.8. $\mathrm{QCD_{LO}}$ (left) and the $(\mathrm{QCD}+\mathrm{CI})_{\mathrm{LO}}$ (right) with Λ =3 TeV models generated by PYTHIA for $|\eta| <= 3$ and the jet p_{T} range $500 \leq p_{\mathrm{T}} \leq 2000$ GeV.

$$\sigma_k = c_k + b_k\,\lambda + a_k\,\lambda^2, \tag{5.1}$$

where c_k, b_k, and a_k are jet-p_{T}-dependent coefficients. Therefore, in principle, one need merely fit the quadratic to the PYTHIA prediction, bin-by-bin, as described in the following.

Study of quadratic dependence The quadratic dependence of the jet cross section on $\lambda = 1/\Lambda^2$ was studied using large samples of generator level events, as well as fully reconstructed events. Figure 5.9 shows the quadratic fits with generator level events and fully reconstructed events. The fits are done for multiple values of Λ. Each vertical sequence of points in Figure 5.9 pertains to a different value of Λ, while each curve corresponds to a different jet p_{T} bin, ranging from 395 GeV, the lowest curve on the vertical axis, to 2000 GeV, the highest curve on the vertical axis. The points range from $\lambda = 0$ TeV^{-2} , i.e., QCD, to $\lambda = 1/9$ TeV^{-2}. We conclude that the quadratic dependence is indeed a good model of the dependence of the cross section on λ. We, therefore, began this analysis by performing quadratic fits to the cross section, bin by bin, making no assumption about the p_{T} dependence of the coefficients c, b, and a. Figure 5.10 shows the bin by bin fit results for the coefficients b and a as a function of jet p_{T} at both the generator and reconstruction levels. The points with error bars are the results of the bin by bin fits. The curves are

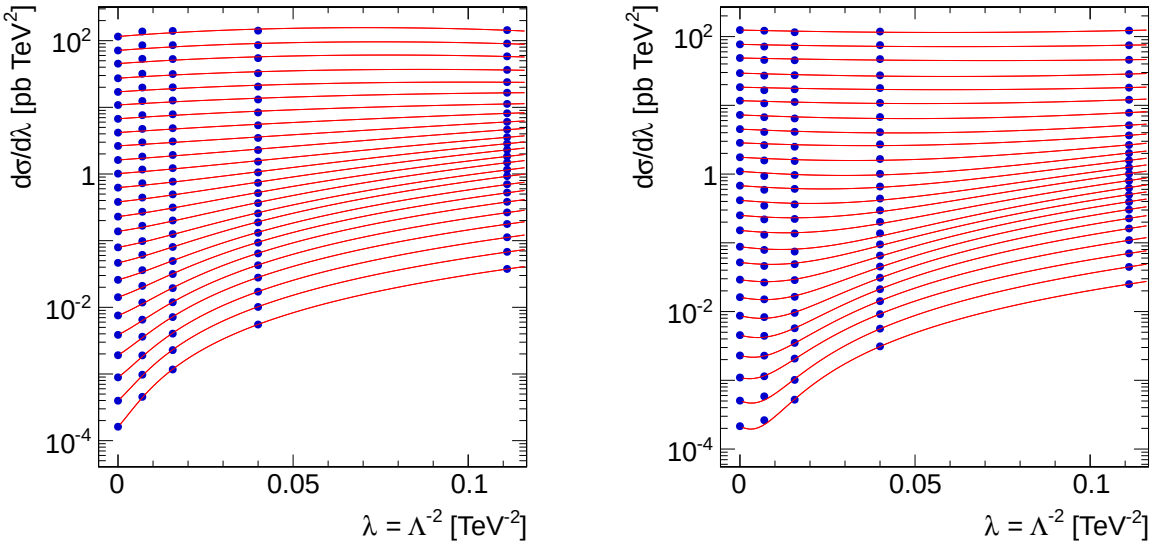

Figure 5.9. Quadratic fits with high statistics generator level events (left) and fully reconstructed events (right). The fits are done for multiple values of Λ.

the results of a fit using a p_{T}-dependent ansatz that was subsequently introduced into the analysis (see Section 5.2.2). The ansatz was introduced to circumvent the inaccuracy of the bin by bin fits below $\sim$ 800 GeV.

5.2.2 QCD and contact interaction models

We use models characterized by the cross section $\mathrm{QCD}_{\mathrm{NLO}} + \mathrm{CI}(\Lambda)$, where $\mathrm{QCD}_{\mathrm{NLO}} = c_k$ is the inclusive jet cross section computed at next-to-leading order, and $\mathrm{CI}(\Lambda) = b_k\,\lambda + a_k\,\lambda^2$ parameterizes the deviation of the inclusive jet cross section from the QCD prediction. The $\mathrm{QCD}_{\mathrm{NLO}}$ cross section is calculated with version 2.1.0-1062 of the fastNLO program with scenario table fnl2332y0.tab [42] using the NLO CTEQ6.6 PDFs [43]. The NLO QCD jet p_{T} spectrum is convolved with the CMS jet response function [44], where the jet energy resolution (JER) $\sigma_{p_{\mathrm{T}}}$ is given by

$$\sigma_{p_{\mathrm{T}}} \;=\; p_{\mathrm{T}}\sqrt{-\frac{n^2}{{p_{\mathrm{T}}}^2}+\frac{s^2{p_{\mathrm{T}}}^m}{p_{\mathrm{T}}}+c^2}, \tag{5.2}$$

with $n = 5.09$, $s = 0.512$, $m = 0.325$, $c = 0.033$, and

$$f(p_{\mathrm{T}}) = \int G(p_{\mathrm{T}}|p'_{\mathrm{T}},\sigma_{p_{\mathrm{T}}})\,f'(p'_{\mathrm{T}})\,dp'_{\mathrm{T}},$$

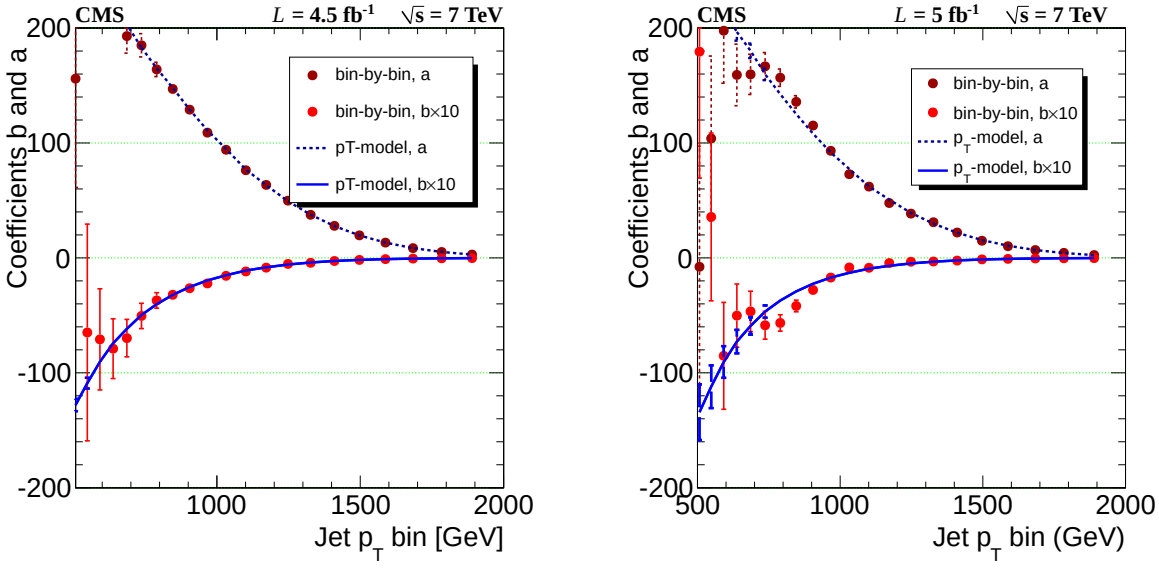

Figure 5.10. The bin by bin fit results for the coefficients b and a at the generator level (left) and the reconstruction level (right). The curves are computed from the 4-parameter p_{T} dependent model. We see that below ∼800 GeV, the bin by bin fits become unreliable. Note that a much larger event sample was used for our generator level studies. Consequently, the bin by bin fits for this sample are more reliable. We conclude that there is nothing intrinsically wrong with performing bin by bin fits, but because of the small signal to background ratio it is necessary to compute the spectra below 800 GeV with adequate statistical precision to yield reliable fits, or limit the search to $p_{\mathrm{T}} > 800$ GeV.

where f and f' are the smeared and unsmeared spectra respectively, G is a Gaussian jet response function, and the integration is with respect to the true jet p_{T}.

The signal term CI(Λ) is modeled by subtracting the leading-order (LO) QCD jet cross section ($\mathrm{QCD_{LO}}$) from the LO jet cross section computed with a contact interaction term. The leading-order jet p_{T} spectra are computed by generating events with and without a CI term as described earlier. The generated events are processed with the full CMS detector simulation program, based on GEANT4 [45]. Interactions between all quarks are included and we consider models both with destructive and constructive interference between the QCD and CI amplitudes. The PYTHIA configuration is given in Table C.1.

In the previous section, we noted the inaccuracy of the bin by bin fits below 800 GeV. That approach had the virtue of avoiding an assumption about the p_{T}-dependence of the quadratic coefficients b_k and c_k. But, we opted to assume an ansatz for the p_{T}-dependence and thereby avoid the inaccuracy of the fits below 800 GeV. The jet p_{T} dependence of

CI(Λ) is modeled by fitting the ratio $f = [\mathrm{QCD}_{\mathrm{NLO}} + \mathrm{CI}(\Lambda)]/\mathrm{QCD}_{\mathrm{NLO}}$ simultaneously to four PYTHIA CI models with $\Lambda = 3, 5, 8$, and 12 TeV. The fit is performed in this manner in order to construct a smooth interpolation over the four cross section ratios. Several functional forms were investigated. We chose the simplest ansatz [46]:

$$f = 1 + p_1 \left(\frac{p_{\mathrm{T}}}{100\ \mathrm{GeV}}\right)^{p_2} \left(\frac{\lambda}{1\ \mathrm{TeV}^{-2}}\right) + p_3 \left(\frac{p_{\mathrm{T}}}{100\ \mathrm{GeV}}\right)^{p_4} \left(\frac{\lambda}{1\ \mathrm{TeV}^{-2}}\right)^2. \qquad (5.3)$$

The results of a fit to models with destructive interference are shown in Figure 5.11. The fit shown in Figure 5.11 uses the central values of the jet energy scale (JES), jet energy resolution (JER), and PDF parameters and the renormalization (μ_{r}) and factorization (μ_{f}) scales set to $\mu_{\mathrm{r}} = \mu_{\mathrm{f}} = \text{jet}\, p_{\mathrm{T}}$. Models with constructive interference are obtained by reversing the sign of the parameter p_1. The fit parameters are given in Table 5.3. Figures 5.12 and

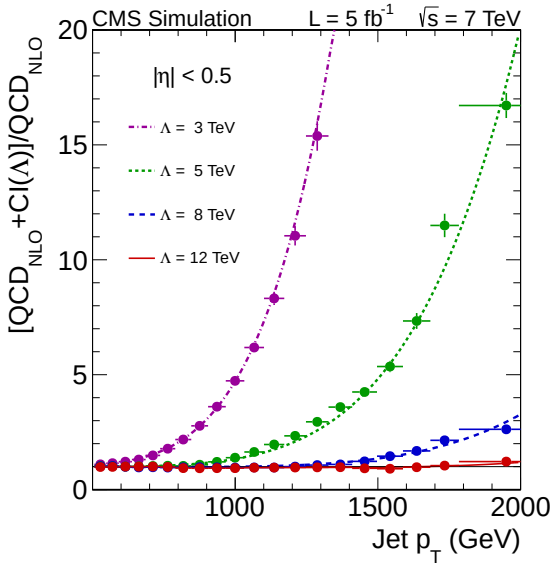

Figure 5.11. The cross section ratios, $f = [\mathrm{QCD}_{\mathrm{NLO}} + \mathrm{CI}(\Lambda)]/\mathrm{QCD}_{\mathrm{NLO}}$, with $\Lambda = 3, 5, 8$, and 12 TeV. The points with error bars are the theoretical values of the cross section ratios. The curves are the results of a fit of Equation 5.3 simultaneously to the four cross section ratios. The NLO QCD jet p_{T} spectrum is calculated using the nominal values of the JES, JER, PDF, renormalization and factorization scales for models with destructive interference. The values of the parameters of the fit are given in Table 5.3.

5.13 show model spectra for different values of Λ in the jet p_{T} range $500 \leq p_{\mathrm{T}} \leq 2000$ GeV. Figure 5.12 shows that the jet production cross section is enhanced at sufficiently high jet p_{T}. However, for interactions that interfere destructively, the cross section can decrease relative

Table 5.3. The fit parameters associated with Figure 5.11. The first row lists the values of the parameters p_1, p_2, p_3, and p_4, while the remaining rows list the elements of the associated covariance matrix.

	p_1	p_2	p_3	p_4
	-1.5×10^{-3}	3.6	1.9×10^{-3}	5.23
p_1	1.4×10^{-6}	3.6×10^{-4}	-3.4×10^{-7}	6.8×10^{-5}
p_2	3.6×10^{-4}	9.2×10^{-2}	-8.4×10^{-5}	1.7×10^{-2}
p_3	-3.4×10^{-7}	-8.4×10^{-5}	1.0×10^{-7}	-2.0×10^{-5}
p_4	6.8×10^{-5}	1.7×10^{-2}	-2.0×10^{-5}	4.1×10^{-3}

to the NLO QCD prediction. For example, for $\Lambda = 10$ TeV, the QCD_{NLO}+CI cross section is lower than the QCD_{NLO} cross section for jet $p_{\text{T}} < 1.3$ TeV. Figure 5.13 shows the contact interaction signal, CI(Λ), as a function of jet p_{T}.

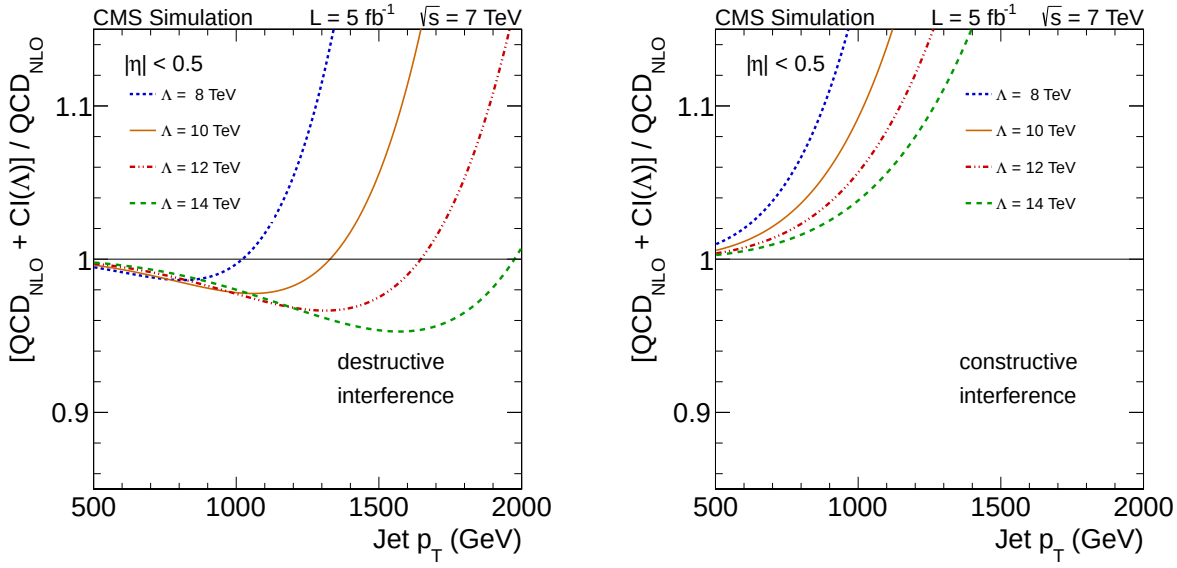

Figure 5.12. The cross section ratios, $f = [\text{QCD}_{\text{NLO}} + \text{CI}(\Lambda)]/\text{QCD}_{\text{NLO}}$, with $\Lambda = 8, 10, 12$, and 14 TeV, for models with destructive (left) and constructive (right) interference.

5.3 Results

We now come to the results of our analysis, that is, the inclusive jet p_{T} spectrum in the search region $507 \leq p_{\text{T}} \leq 2116$ GeV and $|\eta| < 0.5$ at 7 TeV. In Figure 5.14 we compare the observed inclusive jet p_{T} spectrum with the NLO QCD jet p_{T} spectrum, which

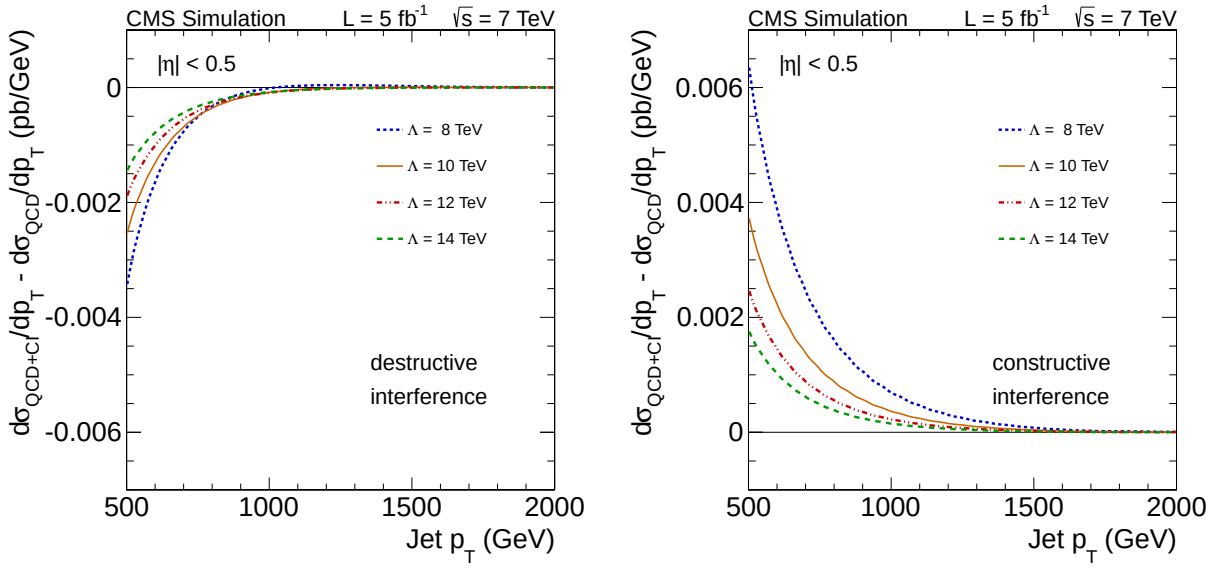

Figure 5.13. The CI signal spectra, defined as $d\sigma_{\mathrm{QCD+CI}}/dp_{\mathrm{T}} - d\sigma_{\mathrm{QCD}}/dp_{\mathrm{T}}$ (pb/GeV) with $\Lambda = 8, 10, 12$ and 14 TeV, for models with destructive (left) and constructive (right) interference.

is normalized to the total observed jet count in the search region using the normalization factor $4.007 \pm 0.009\,\mathrm{fb}^{-1}$ (see Section 5.4). The normalization is the ratio of the observed jet count to the predicted cross section in the search region. The data and the prediction are in good agreement with a Kolmogorov-Smirnov probability Pr(KS) of 0.66 and a χ^2 per number of degrees of freedom (NDF) of 23.5/19. Table 5.4 lists the observed jet counts. Figure 5.15 compares the observed jet p_{T} spectrum in the search region with model spectra for different values of Λ, for models with destructive interference. Figure 5.16 compares the data with models with constructive interference.

5.4 Interpretation

We find no significant deviations between the observed and predicted spectra, therefore, the results are interpreted in terms of lower limits on the CI scale Λ using the models described in Section 5.2.1. In the search region, the inclusive jet spectrum has a range of five orders of magnitude, which causes the limits on Λ to be sensitive to the choice of the normalization factor and the size of the data sets. We have found that a few percent change in the normalization factor can cause limits to change by as much as 50%. Therefore, for

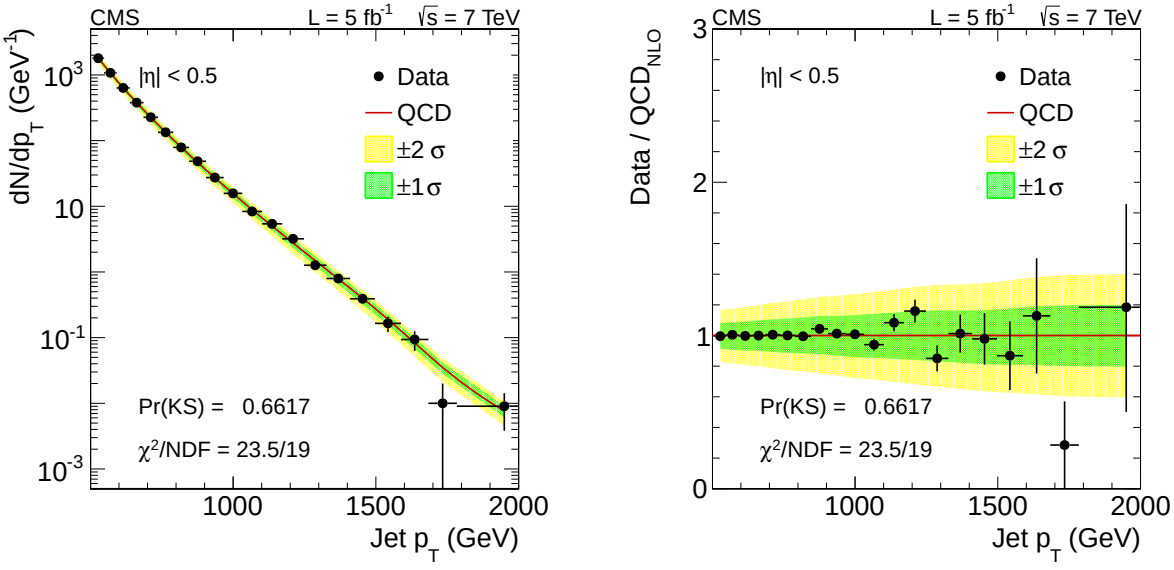

Figure 5.14. The observed jet p_{T} spectrum compared with the NLO QCD jet p_{T} spectrum (left). The bands represent the total uncertainty in the prediction and incorporate the uncertainties in the PDFs, jet energy scale, jet energy resolution, the renormalization and factorization scales, and the modeling of the jet p_{T} dependence of the parameters in Equation 5.3. The ratio of the observed to the predicted spectrum (right). The error bars represent the statistical uncertainties in the expected bin count.

Table 5.4. The observed jet count for each jet p_{T} bin in the range 507–2116 GeV.

Bin	p_{T} (GeV)	Jets	Bin	p_{T} (GeV)	Jets
1	507–548	73792	11	1032–1101	576
2	548–592	47416	12	1101–1172	384
3	592–638	29185	13	1172–1248	243
4	638–686	18187	14	1248–1327	100
5	686–737	11565	15	1327–1410	66
6	737–790	7095	16	1410–1497	34
7	790–846	4413	17	1497–1588	15
8	846–905	2862	18	1588–1684	9
9	905–967	1699	19	1684–1784	1
10	967–1032	1023	20	1784–2116	3

the purpose of computing limits, we consider only the shape of the jet p_{T} spectrum. This we achieve by using a multinomial distribution, which is the probability to observe K counts, N_j, $j = 1, \cdots, K$, given the observation of a total count $N = \sum_{j=1}^{K} N_j$. Our likelihood is then defined by

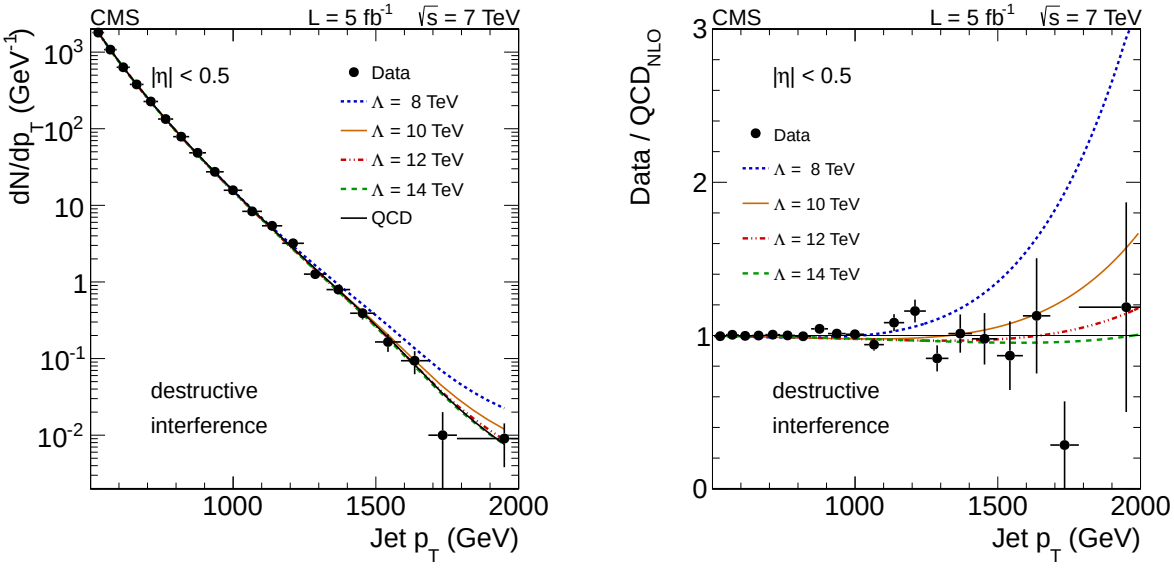

Figure 5.15. The data compared with model spectra for different values of Λ for models with destructive interference (left). The ratio of these spectra to the NLO QCD jet p_{T} spectrum (right).

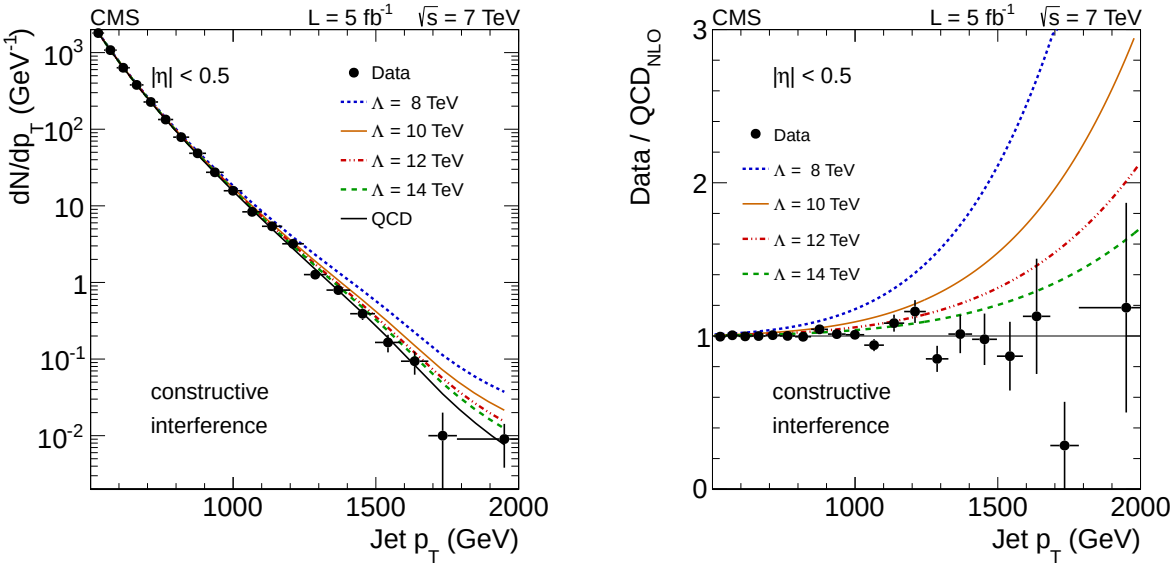

Figure 5.16. The data compared to model spectra for different values of Λ for models with constructive interference (left). The ratio of these spectra to the NLO QCD jet p_{T} spectrum (right).

$$p(D|\lambda,\omega) \;=\; \frac{N!}{N_1!\cdots N_K!}\prod_{j=1}^{K}\left(\frac{\sigma_j}{\sigma}\right)^{N_j}, \tag{5.4}$$

where $K = 20$ is the number of bins in the search region, N_j is the jet count in the jth jet p_{T} bin, $D \equiv N_1, \cdots, N_K$, $\sigma = \sum_{j=1}^{K} \sigma_j$ and N are the total cross section and total observed count, respectively, in the search region, and the symbol ω denotes the nuisance parameters $p_1, \cdots, p_4$ in Equation 5.3.

We account for systematic uncertainties by integrating the likelihood with respect to a nuisance prior $\pi(\omega)$ constructed as described in Section 5.4.1. This calculation yields the marginal likelihood

$$\begin{aligned} p(D|\lambda) &= \int p(D|\lambda, \omega)\, \pi(\omega)\, d\omega, \\ &\approx \frac{1}{M} \sum_{m=1}^{M} p(D|\lambda, \omega_m), \end{aligned} \tag{5.5}$$

where $M = 500$ is the number of points $\omega = p_1, p_2, p_3, p_4$ sampled from the nuisance prior $\pi(\omega)$ described in Section 5.4.2. The marginal likelihood $p(D|\lambda)$ is the basis of the limit calculations. The likelihood functions for models with destructive and constructive interference are shown in Figure 5.17.

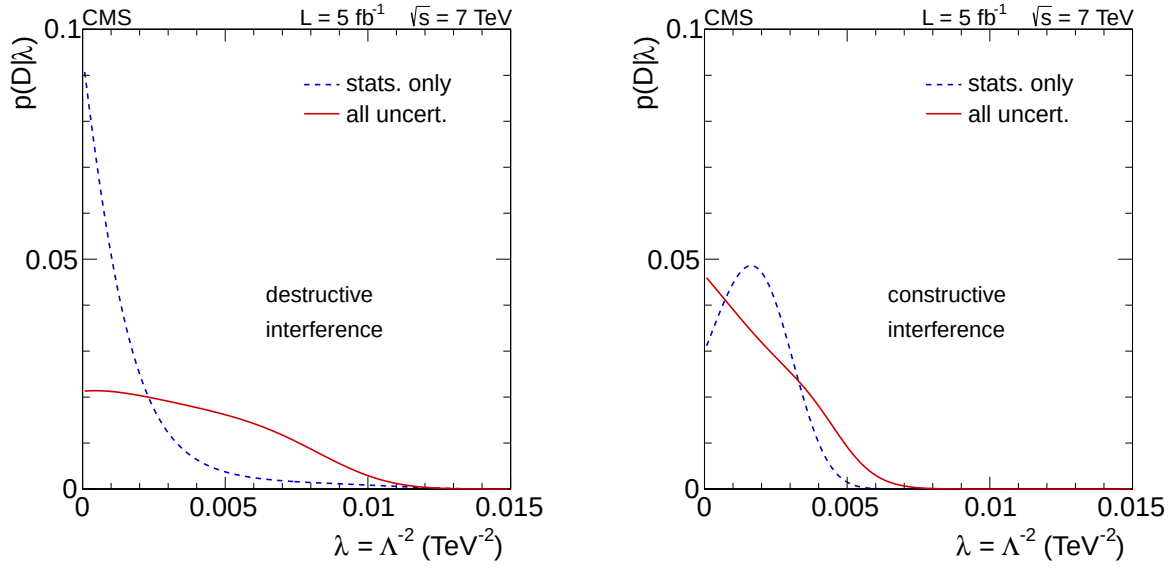

Figure 5.17. The likelihood functions assuming a model with either destructive (left) or constructive (right) interference. The dashed curve is the likelihood function including statistical uncertainties only and the central values of all nuisance parameters. The solid curve is the likelihood marginalized over all systematic uncertainties.

5.4.1 Uncertainties

The dominant sources of systematic uncertainties are associated with the JES, the PDFs, the JER, the renormalization (μ_r) and factorization (μ_f) scales, and the modeling parameters of Equation 5.3. Non-perturbative corrections are less than 1% for transverse momenta above ~400 GeV [44], are negligible compared with other uncertainties, and are therefore not applied to our analysis.

Jet Energy Scale The jet energy scale is sampled using 16 Gaussians each with zero mean and unit variance that are used to calculate a coherent shift of the jet energy scale for every jet, in every event, in every simulated sample. If we denote by x a Gaussian variate and by δ one of the 16 components of the jet energy scale uncertainty [34] for a given jet, the p_T of the jet is shifted by $x\sigma$. We sum all 16 contributions in quadrature to form an overall shift to the jet p_T.

The effect of shifting the jet energy scale up or down is illustrated in Figure 5.18. The figure illustrates the effect of an upwards or downwards shift in the jet energy scale for a pure QCD spectrum (upper plot), which has a steeply falling spectrum, and for a pure CI component (lower plot), which rises as a function of p_T. An upwards shift in the JES causes a rightwards shift to the spectrum and therefore an upwards shift in the count per bin, while the converse is true for a downwards shift in the JES. An upwards shift in the JES causes the CI component of the spectrum to shift rightwards. However, in this case, the count per bin shifts downwards because of the rising spectrum. A 1 TeV jet has approximately a 10% JES uncertainty.

Jet Energy Resolution The measured jet energy resolution (JER) is about 10% worse than the value extracted from MC simulations. Therefore, the uncertainty on the JER uses the data-driven estimates shown in Table 5.5 [47], where the jet p_T resolutions for data are estimated using dijet asymmetry and photon+jet p_T balancing. This study focuses on the

Table 5.5. Data-driven estimates for JER uncertainties.

$\lvert y\rvert < 0.5$	$0.5 \leq \lvert y\rvert < 1$	$1 \leq \lvert y\rvert < 1.5$	$1.5 \leq \lvert y\rvert < 2$	$2 \leq \lvert y\rvert < 2.5$
10%	10%	10%	15%	25%

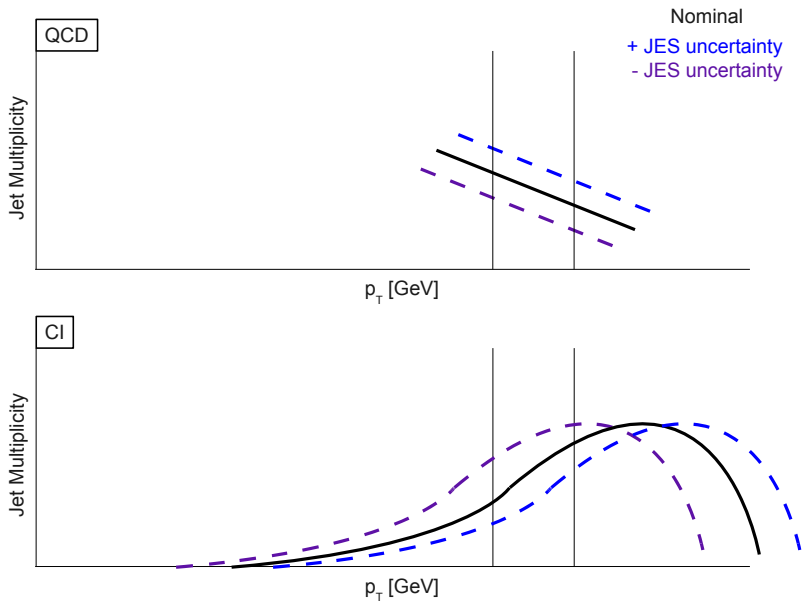

Figure 5.18. The figure illustrates the effect of an upwards or downwards shift in the jet energy scale (JES) for a pure QCD spectrum (top), which has a steeply falling spectrum, and for a pure CI component (bottom), which rises as function of p_T. An upwards shift in the JES causes a rightwards shift to the spectrum and therefore an upwards shift in the count per bin, while the converse is true for a downwards shift in the JES. An upwards shift in the JES causes the CI component of the spectrum to shift rightwards. However, in this case, the count per bin shifts downwards because of the rising spectrum.

central barrel region, $|y| < 0.5$. We sample the JER using a method identical to that used to sample the JES.

Parton Distribution Functions The CTEQ Collaboration currently provides PDF sets with each parameter shifted by "$\pm$ 1.64 standard deviation" [48]. This is adequate for standard error propagation, but not for error propagation through marginalization, (see Section 5.4.2).

The effects of the JES, JER, PDF, and NLO scale uncertainties are illustrated in Figure 5.19, which shows the uncertainty bands in the spectrum arising from the three sets of systematic uncertainties. As expected, the uncertainties due to the JES and PDF are dominant.

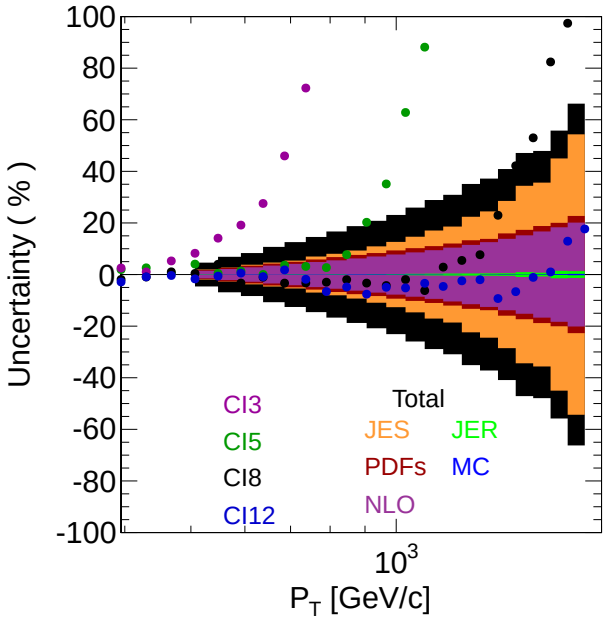

Figure 5.19. The relative uncertainty in the jet p_T spectrum arising from JES, PDF, JER, and fitting uncertainties. In this plot, the systematic uncertainties are added in quadrature. This plot also shows the ratio (QCD+CI)/QCD as a function of p_T for Λ = 3, 5, 8 and 12 TeV.

5.4.2 Nuisance prior

In principle, a discrete representation of the nuisance prior $\pi(\omega)$ can be constructed by sampling simultaneously the JES, JER, PDFs, and the three values of $\mu_{\rm f}$ and $\mu_{\rm r}$: $p_{\rm T}/2$, $p_{\rm T}$, and $2p_{\rm T}$. However, the CTEQ collaboration [43] does not provide a sampling of PDFs. Instead, CTEQ6.6 contains 44 PDF sets in which the 22 PDF parameters are shifted by approximately ± 1.64 standard deviations. If we assume the Gaussian approximation to be valid, we can construct approximate 20×20 covariance matrices for the jet spectra from the 44 PDF sets. Using these matrices, we generate ensembles of six correlated spectra: $\mathrm{QCD}_{\rm NLO}$, $\mathrm{QCD}_{\rm LO}$, and $(\mathrm{QCD} + \mathrm{CI}(\Lambda))_{\rm LO}$ with $\Lambda = 3, 5, 8$, and 12 TeV. The generation is performed for models both with destructive and constructive interference. We approximate the nuisance prior $\pi(\omega)$ starting with two sets of ensembles. In the first, the six 20-bin model spectra $\mathrm{QCD}_{\rm NLO}$, $\mathrm{QCD}_{\rm LO}$, and $[\mathrm{QCD} + \mathrm{CI}(\Lambda)]_{\rm LO}$ with $\Lambda = 3, 5, 8$, and 12 TeV are varied, reflecting random variations in the PDF parameters as well as random choices of the three $\mu_{\rm r}$ and $\mu_{\rm f}$ scales, while keeping the JES and JER parameters fixed at their central values; we

call these the PDF ensembles. In the second set of ensembles, the JES and JER parameters are varied simultaneously, while keeping the PDF parameters fixed to their central values and the renormalization and factorization scales at their nominal values; we call these the JES/JER ensembles.

Generating the PDF ensembles In the PDF ensembles, each of the six model spectra is sampled from a multivariate Gaussian distribution using the associated 20×20 covariance matrix. For each model spectrum, the covariance matrix is approximated by

$$C_{nm} = \sum_{i=1}^{22} \sum_{j=1}^{22} \Delta X_{ni} \, \Delta X_{mj}, \tag{5.6}$$

where $\Delta X_{ni} = max(\Delta X^{+}_{ni_{max}}, \Delta X^{-}_{ni_{max}}, 0)$, $\Delta X^{+}_{ni_{max}} = max(X^{+}_{ni} - X_0, X^{-}_{ni} - X_0, 0)$, $\Delta X^{-}_{ni_{max}} = max(X_0 - X^{+}_{ni}, X_0 - X^{-}_{ni}, 0)$ with X_0 as the central value and $X^{\pm}_{ni}$ are the cross section values for nth jet bin associated with the $+$ and $-$ variations of the ith pair of CTEQ6.6 PDF sets [49]. CTEQ [43] publishes approximate 90% intervals. We therefore approximate 68% intervals by dividing each ΔX by 1.64. The correlation induced by the PDF uncertainties across all six model spectra is maintained by using the same set of underlying Gaussian variates during the sampling of the spectra.

Generating the JES/JER ensembles In the JES/JER ensembles, the JES and JER parameters are sampled simultaneously for the five model spectra $\mathrm{QCD}_{\mathrm{LO}}$, and $(\mathrm{QCD{+}CI})_{\mathrm{LO}}$ with $\Lambda = 3, 5, 8$, and 12 TeV, yielding ensembles of correlated shifts from the central JES, JER, and PDF values of the $\mathrm{QCD}_{\mathrm{LO}}$ and $(\mathrm{QCD{+}CI})_{\mathrm{LO}}$ spectra. For example, we compute the spectral residuals $\delta\sigma = \mathrm{QCD}' - \mathrm{QCD}_{\mathrm{central}}$, where QCD$'$ is the shifted jet p_{T} spectrum and $\mathrm{QCD}_{\mathrm{central}}$ is the jet p_{T} spectrum computed using the central values of the JES, JER, and PDF parameters. Coherent shifts of the jet energy scale are calculated for every jet in every simulated event. The jet p_{T} is shifted by $x\delta$ for each component of the jet energy scale uncertainty, of which there are sixteen, where x is a Gaussian variate of zero mean and unit variance, and δ is a jet-dependent uncertainty for a given component. The contributions from all uncertainty components are summed to obtain an overall shift in the jet p_{T}. From studies of dijet asymmetry and photon+jet p_{T} balancing, the uncertainty in the jet energy resolution is estimated to be 10% in the pseudorapidity $|\eta| < 0.5$ [44]. We sample the jet

energy resolution using a procedure identical to that used to sample the jet energy scale, but using a single Gaussian variate.

Generating the JES/JER/PDF ensemble Another ensemble is created, from the PDF ensembles and the JES/JER ensembles, that approximates simultaneous sampling from the JES, JER, PDF, renormalization, and factorization parameters. We pick at random a correlated set of six spectra from the PDF ensembles, and a correlated set of five spectral residuals from the JES/JER ensembles. The JES/JER spectral residuals $\delta\sigma$ are added to the corresponding shifted spectrum from the PDF ensembles, thereby creating a spectrum in which the JES, JER, PDF, μ_{r}, and μ_{f} parameters have been randomly shifted. The NLO QCD spectrum (from the PDF ensembles) is shifted using the LO QCD JES/JER spectral residuals in order to approximate the effect of the JES and JER uncertainties in this spectrum.

The result of the above procedure is an ensemble of sets of properly correlated spectra $\mathrm{QCD}_{\mathrm{NLO}} + \mathrm{CI}(\Lambda)$ with $\Lambda = 3, 5, 8$, and 12 TeV, in which the JES, JER, PDF, μ_{r} and μ_{f} parameters vary randomly. The ansatz in Equation 5.3 is then fitted to the quartet of ratios $[\mathrm{QCD}_{\mathrm{NLO}} + \mathrm{CI}(\Lambda)]$ / $\mathrm{QCD}_{\mathrm{NLO}}$ as described in Section 5.4.1 to obtain parameter values for p_1, p_2, p_3, and p_4. Five hundred sets of these parameters are generated, constituting a discrete approximation to the prior $\pi(\omega) \equiv \pi(p_1, p_2, p_3, p_4)$.

5.4.3 Lower limits on Λ

We compute limits with a Bayesian method using the marginal likelihood $p(D|\lambda)$, Equation 5.5, and two different priors for λ: a prior flat in λ and a reference prior [50, 51, 52]. An upper limit on λ, λ^*, is found by solving

$$\int_0^{\lambda^*} p(D|\lambda)\,\pi(\lambda)\,d\lambda/p(D) = 0.95, \tag{5.7}$$

where $p(D)$ is a normalization constant. The integrals are performed using numerical quadrature. Using a reference prior, we find lower limits on Λ of 10.1 TeV and 14.1 TeV for models with destructive and constructive interference, respectively. The corresponding limits using the flat prior are 10.6 TeV and 14.6 TeV, respectively. The CMS collaboration

required that limits for this analysis be calculated using CLs. For completeness, we describe this calculation below.

CL_s calculation A CL_s limit calculation requires two elements: a test statistic Q that depends on the quantity of interest and its sampling distribution for two different hypotheses, here $\lambda > 0$, which we denote by H_λ, and $\lambda = 0$, which we denote by H_0. H_λ is the signal plus background hypothesis while H_0 is the background-only hypothesis. For this study, we use the statistic

$$Q(\lambda) = t(D, \lambda) \equiv -2 \ln \left[p(D|\lambda) / p(D|0) \right], \tag{5.8}$$

where $p(D|\lambda)$ is the marginal likelihood 5.5. We compute the sampling distributions

$$p(Q|H_\lambda) = \int \delta[Q - t(D, \lambda)] \, p(D|\lambda) \, dD, \tag{5.9}$$

and

$$p(Q|H_0) = \int \delta[Q - t(D, \lambda)] \, p(D|0) \, dD, \tag{5.10}$$

pertaining to the hypotheses H_λ and H_0, respectively, and solve

$$\mathrm{CL_s} \equiv p(\lambda)/p(0) = 0.05, \tag{5.11}$$

to obtain a 95 % confidence level (CL_s) upper limit on λ, where the p-value $p(\lambda)$ is defined by

$$p(\lambda) = \Pr[Q(\lambda) > Q_0(\lambda)], \tag{5.12}$$

and Q_0 is the observed value of Q.

In practice, the CL_s limits are approximated as follows:

1. Choose a value of λ, say λ^*, and compute the observed value of Q, $Q_0(\lambda^*)$.

2. Choose at random one of the $M = 500$ sets of nuisance parameters p_1, p_2, p_3, and p_4.

3. Generate a spectrum of $K = 20$ counts, D, according to the multinomial distribution, Equation 5.4, with $\lambda = \lambda^*$, which corresponds to the hypothesis H_λ. Compute $Q = t(D, \lambda^*)$ and keep track of how often $Q(\lambda^*) > Q_0(\lambda^*)$. Call this count n_λ.

4. Generate another set of 20 counts, D, but with $\lambda = 0$, corresponding to the hypothesis H_0. Compute $Q = t(D, \lambda^*)$ and keep track of how often $Q(\lambda^*) > Q_0(\lambda^*)$. Call this count n_0.

5. Repeat $25,000$ times steps 2 to 4, compute $\mathrm{CL_s} \approx n_\lambda / n_0$ and report $\lambda = \lambda^*$ as the upper limit on λ at 95% CL if $\mathrm{CL_s}$ is sufficiently close to 0.05; otherwise, keep repeating steps 1 to 4 with different values of λ. The algorithm starts with two values of λ that are likely to bracket the solution and the solution is found using a binary search, which typically requires about 10 to 15 iterations.

5.4.4 Further Studies

It has become conventional to provide some measure of the sensitivity of an experiment, such as the expected limit, typically defined as the average limit over a suitable ensemble of pseudo experiments.

Pseudo Experiments Figures 5.20 (left) and 5.20 (right) show the ensembles used to estimate the expected limits. On average, the limits with systematic uncertainties included are lower than the limits without. For models with constructive interference, when the systematic uncertainties are included all pseudo experiments yield a limit that is "worse" than the limit without. However, we find that about 20% of the pseudo experiments analyzed using a model with destructive interference yield an "observed" limit with systematic uncertainties included that is lower than the limit computed without. That is, experiments of lower sensitivity can sometimes yield better limits than an experiment with higher sensitivity. This behavior is analogous to the following well-known situation. A low-background experiment is generally considered to be more sensitive than one with higher background, but for the same observation the better experiment may yield a "worse" limit on the signal cross section than the one obtained with the experiment of lower sensitivity. That this can happen is the reason why it has become common practice to quote some measure of the sensitivity of an experiment, such as expected limits, along with the observed limits. While the limits are indeed worse *on average* when systematic uncertainties are included than when they are not, this may not be true for all experiments.

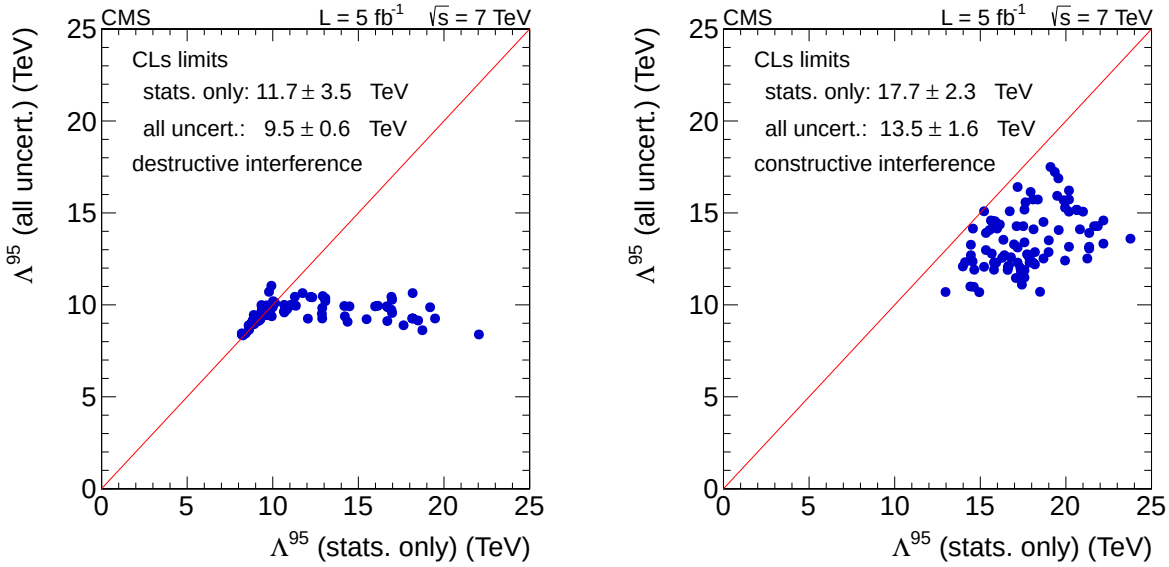

Figure 5.20. (left) Limits for pseudo experiments analyzed using a model with destructive interference. Each point represents the limits without and with systematic uncertainties for one pseudo experiment. As expected, on average, the limit with systematic uncertainties are lower than those without. (right) Limits for pseudo experiments analyzed using a model with constructive interference.

CHAPTER 6

SUMMARY

It has been 17 years since a study comparable to the one described in this dissertation was performed with the inclusive jet p_{T} spectrum [18]. Our analysis officially started on February 1st 2011. The final approval was on January 18th, 2013. The final reading of the paper by the CMS Publication Committee was one of the shortest on record, due to all the preparation. The publication proofs were completed on March 18th, 2013 and paper was published March 26th, 2013.

The inclusive jet p_{T} spectrum of 7 TeV proton-proton collision events in the range $507 \leq p_{\mathrm{T}} \leq 2116$ GeV and $|\eta| < 0.5$ has been studied using a data set corresponding to an integrated luminosity of 5.0 fb^{-1}. The data are in excellent agreement with the jet p_{T} spectrum predicted using perturbative QCD at NLO when the predicted spectrum is convolved with the CMS jet response function and normalized to the observed spectrum in the search region. The Kolmogorov-Smirnov probability Pr(KS) is 0.66 and the χ^2 per number of degrees of freedom (NDF) is 23.5/19) Unfortunately, this means that we find no evidence of contact interactions (CI).

We therefore use our null result to set the lower limits on the CI scale Λ listed in Table 6.1. It is noteworthy that the limits reported in this dissertation, which are the most sensitive limits published to date, have been obtained reprising the classic method to search for contact interactions: namely, searching for deviations from QCD at high jet transverse momentum.

This work has been well-received by our colleagues in CMS as evidenced by the following quotes from the CMS Exotica Multijet conveners.

Robert Harris "... for the first time in 20 years the jet pt distribution is being used to set the best limits on contact interactions, more than just competitive with the angular distribution. This is a triumph of the CMS understanding of the Jet Energy Scale, and

HEP understanding of parton distribution uncertainties ... Further, I believe this result is so interesting to the community searching for new physics with jets that it warrants a paper, despite the fact that it is 2011 data. It is both the new limits and also the reintroduction of this classic technique that is of interest to the community."

Table 6.1. Lower limits on the contact interaction scale, based on the analysis described in this dissertation, using different statistical methods: a Bayesian method using a reference prior and a flat prior and the CLs criterion.

Limits						
		reference prior	flat prior	CL_s		
Destructive Interference						
Observed	$\Lambda >$	10.1	10.6	9.9	TeV	all systematics
Expected	$\Lambda >$			9.5 $\pm$ 0.6	TeV	all systematics
Constructive Interference						
Observed	$\Lambda >$	14.1	14.6	14.3	TeV	all systematics
Expected	$\Lambda >$			13.6 $\pm$ 1.6	TeV	all systematics

Sung-Won Lee "Big congratulations to the authors (Jeff and Harrison; you two did an EXCELLENT work), ARC (Anwar, Tommaso, Jim, Jane, Dave), and all involved! ... and many thanks to the EXO conveners and especially to the PC(Greg et al) + (EXO)PubComm (Paris, Bob, Dave, Giovanni, Claudia- Elisabeth) for helping to get this out today!! Once again, we would like to reiterate the importance of this paper ... Also, note that searching for contact interactions in the inclusive jet pt spectrum is the hardest jet analysis in Exotic and inclusive jet pT spectrum has not been used by hadron colliders for the 19 years since CDF released an excess at high pt (attributed to the gluon distribution not being adequately modeled in PDFs)."

6.1 Future use of results

In this work, we modeled possible deviations from QCD using the contact interaction model in Pythia. No claim is made that this is the best, or the most general, way to model

a putative deviation from QCD. Different models of new physics could in principle yield different forms of deviation. In order to make our results as useful as possible, subject to the constraints imposed by the CMS collaboration, we have chosen to disseminate as much information as possible. It should be possible for theorists to use our results to test models of new physics other than the one we used in this dissertation.

We have published the observed jet counts, the jet resolution function, and details of the models we have used. What is missing in the published paper is the covariance matrix of the nuisance parameters $p_1, \cdots, p_4$, computed using only the JES, JER, and modeling uncertainties. If this matrix were publicly available, it would be possible for a theorist to take account of experimental systematic uncertainties in a straightforward manner. We hope that in future work this matrix will also be made available.

There is considerable interest within parts of CMS to extend this analysis to the full 8 TeV data set. This work is underway. One significant change with respect to the published analysis is the plan to use the NLO calculation of the CI cross section by Gao *et al.* [53], for which a program to compute this cross section has recently become available [54].

APPENDIX A

PUBLICATIONS

This Appendix contains three papers:

1. CMS-EXO-11-010, CERN-PH-EP-2013-002, Phys. Rev. D 87, 052017 (2013),

   For readers with CADI access: EXO-11-010

2. CMS-CR-2010-273, Journal of Physics: Conference Series, 331(7):072019, 2011,

3. CMS-DN-2009-021,

where the authors are the CMS collaboration. The copyright permissions are listed in Appendix D.

Search for contact interactions paper

This is a publication based on my research at CMS as a member of the Exotica Multijet group from 2011 through 2013.

CMS computing paper

This is a publication based on my experience as a member of Fermilab's Tier-1 data processing team. In October, 2010, I was invited to talk at the International Conferences on Computing in High Energy and Nuclear Physics (CHEP), CMS Distributed Computing Workflow Experience Presentation, slides. CHEP is a major series of international conferences for physicists and computing professionals from the high energy and nuclear physics community, computer science, and information technology. CHEP provides an international forum to exchange the experience and needs of the community, and to review recent, ongoing, and future activities. The conference, organized by Academia Sinica Grid

Computing Center, was held at Academia Sinica in Taipei, Taiwan on 18-22 October 2010. The CMS Conference report which follows, CR2010_273, has been published in the open access Journal of Physics: Conference Series (JPCS), published by IOP Publishing [55].

Hardware paper

This is a public detector note [56] regarding the CMS hadron calorimeter photon detector upgrade [57]. The detector note was presented as a parallel talk at CAM: Canadian American Mexican Graduate Student Physics Conference, on October 22-24 2009, in Acapulco Mexico. This was the joint meeting of the Canadian (CAP), American (APS) and Mexican (SMF) Physical Societies.

Publication permissions

CMS Publications Committee chair, CERN

March 25, 2013
Paris Sphicas

Dear Jeff;
I had to check with the CERN library, for the request to include a CERN document (the preprint) on an "as is" basis in a thesis was a new one to me. I am told there is no problem, as long as you indicate clearly that the pdf in question is on CDS server, with the CMS collaboration as author (and provide the reference). With this, then, you have our (CMS) permission. Please let me know if you need anything else from our side.

With my best regards,
Paris Sphicas
CMS Publications Committee chair

Rights & Permissions Officer, IOP Publishing Ltd

March 19, 2013

Laura Sharples

Dear Jeff,

Not challenging at all! Articles published in our conference series are published under licence. The authors retain copyright and grant us a non-exclusive licence to publish the paper. Therefore you do not need to gain our permission to reuse the paper in your thesis. We would be grateful if you could include citation details and, for electronic use, a link via DOI to the version of record. You can see the full terms of the licence here: License If you have any questions, please let me know. In the meantime, I wish you the best of luck with the completion of your thesis.

Kind regards,

Laura

Laura Sharples

Rights & Permissions Officer

IOP Publishing Ltd

Temple Circus, Temple Way, Bristol BS1 6HG

Publications Marketing Coordinator, American Physical Society

April 8, 2013

Dear Mr. Haas,

Thank you for your email. As the author, you have the right to use the article or a portion of the article in a thesis or dissertation without requesting permission from APS, provided

the bibliographic citation and the APS copyright credit line are given on the appropriate pages. This applies to adding an appendix as well. Please call if you have any problems, but you may proceed with your request.

Best wishes,

Alex Menendez
Publications Marketing Coordinator
American Physical Society
http://librarians.aps.org/

PHYSICAL REVIEW D **87,** 052017 (2013)

Search for contact interactions using the inclusive jet p_T spectrum in pp collisions at $\sqrt{s} = 7$ TeV

S. Chatrchyan *et al.**
(CMS Collaboration)

(Received 21 January 2013; published 26 March 2013)

Results are reported of a search for a deviation in the jet production cross section from the prediction of perturbative quantum chromodynamics at next-to-leading order. The search is conducted using a 7 TeV proton-proton data sample corresponding to an integrated luminosity of 5.0 fb^{-1}, collected with the Compact Muon Solenoid detector at the Large Hadron Collider. A deviation could arise from interactions characterized by a mass scale Λ too high to be probed directly at the LHC. Such phenomena can be modeled as contact interactions. No evidence of a deviation is found. Using the CL_s criterion, lower limits are set on Λ of 9.9 TeV and 14.3 TeV at 95% confidence level for models with destructive and constructive interference, respectively. Limits obtained with a Bayesian method are also reported.

DOI: 10.1103/PhysRevD.87.052017 PACS numbers: 13.85.Rm

I. INTRODUCTION

Interactions at an energy scale much lower than the mass of the mediating particle can be modeled by contact interactions (CI) [1–4] governed by a single mass scale conventionally denoted by Λ. A search for contact interactions is therefore a search for interactions whose detailed characteristics become manifest only at higher energies. Contact interactions can affect the jet angular distributions as well as the jet transverse momentum (p_T) spectra, particularly for low-rapidity jets. Lower limits on Λ have been set by the CDF [5], D0 [6], and ATLAS [7] collaborations. The Compact Muon Solenoid (CMS) collaboration has previously measured the dijet angular distribution [8] using a data set of $\sqrt{s} = 7$ TeV proton-proton collisions corresponding to an integrated luminosity of 2.2 fb^{-1}, and found $\Lambda > 8.4$ TeV and $\Lambda > 11.7$ TeV at 95% confidence level (C.L.), for models with destructively and constructively interfering amplitudes, respectively.

The inclusive jet p_T spectrum, i.e., the spectrum of jets in $p + p \rightarrow$ jet $+ X$ events, where X can be any collection of particles, is generally considered to be less sensitive to the presence of contact interactions than the jet angular distribution. This perception is due to the jet p_T spectrum's greater dependence on the jet energy scale (JES) and on the parton distribution functions (PDF), which are difficult to determine accurately. However, considerable progress has been made by the CMS collaboration in understanding the JES [9]. The understanding of PDFs has also improved greatly at high parton momentum fraction [10–12], in part because of the important constraints on the gluon PDF provided by measurements at the Tevatron [13,14]. These developments have made the jet p_T spectrum a competitive observable to search for phenomena described by contact interactions, reprising the method that was used in searches by CDF [15] and D0 [16].

In this paper, we report the results of a search for a deviation in the jet production cross section from the next-to-leading-order (NLO) quantum chromodynamics (QCD) prediction of jets produced at low-rapidity with transverse momenta >500 GeV. The analysis is based on a 7 TeV proton-proton data sample corresponding to an integrated luminosity of 5.0 fb^{-1}, collected with the CMS detector at the Large Hadron Collider (LHC).

II. THEORETICAL MODELS

The experimental results are interpreted in terms of a CI model described by the effective Lagrangian [3,17]

$$L = \zeta \frac{2\pi}{\Lambda^2} (\bar{q}_L \gamma^\mu q_L)(\bar{q}_L \gamma_\mu q_L), \tag{1}$$

where q_L denotes a left-handed quark field and $\zeta = +1$ or -1 denote destructively or constructively interfering amplitudes, respectively. The amplitude for jet production can be written as

$$a = a_{SM} + \lambda a_{CI},$$

where a_{SM} and a_{CI} are the standard model (SM) and contact interaction amplitudes, respectively. Since the amplitude is linear in $\lambda = 1/\Lambda^2$, the cross section σ_k in the kth jet p_T bin is given by

$$\sigma_k = c_k + b_k \lambda + a_k \lambda^2, \tag{2}$$

where c_k, b_k, and a_k are jet-p_T-dependent coefficients.

We use models characterized by the cross section $QCD_{NLO} + CI(\Lambda)$, where $QCD_{NLO} = c_k$ is the inclusive jet cross section computed at next-to-leading order, and $CI(\Lambda) = b_k \lambda + a_k \lambda^2$ parametrizes the deviation of the inclusive jet cross section from the QCD prediction arising from the hypothesized contact interactions. The QCD_{NLO} cross section is calculated with version 2.1.0-1062 of the

*Full author list given at the end of the article.

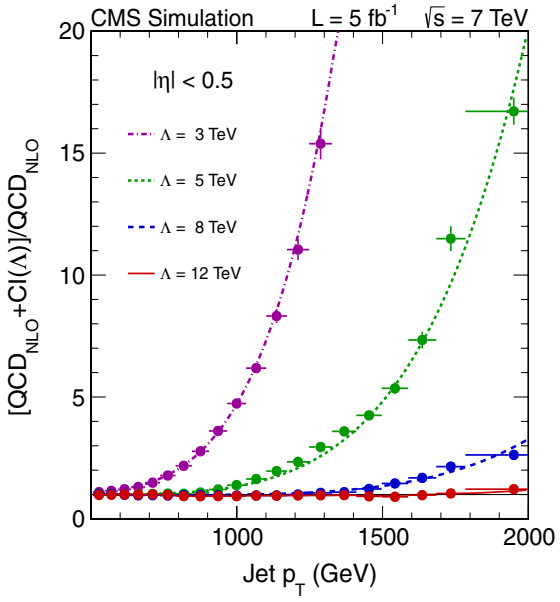

FIG. 1 (color online). The cross section ratios, $f = [\mathrm{QCD_{NLO}} + \mathrm{CI}(\Lambda)]/\mathrm{QCD_{NLO}}$, with $\Lambda = 3$, 5, 8, and 12 TeV. The points with error bars are the theoretical values of the cross section ratios. The curves are the results of a fit of Eq. (4) simultaneously to the four cross section ratios. The NLO QCD jet p_{T} spectrum is calculated using the nominal values of the JES, JER, PDF, renormalization and factorization scales for models with destructive interference. The values of the parameters of the fit are given in Table I.

fastNLO program with scenario table fnl2332y0.tab [18] using the NLO CTEQ6.6 PDFs [19]. We do not unfold the observed inclusive jet p_{T} spectrum. Instead, the NLO QCD jet p_{T} spectrum is convolved with the CMS jet response function, where the jet energy resolution (JER) $\sigma_{p_{\mathrm{T}}}$ for low-rapidity jets is given by

$$\sigma_{P_{\mathrm{T}}} = P_{\mathrm{T}}\sqrt{-\frac{n^2}{p_{\mathrm{T}}^2} + \frac{s^2 p_{\mathrm{T}}^m}{p_{\mathrm{T}}} + c^2}, \qquad (3)$$

with $n = 5.09$, $s = 0.512$, $m = 0.325$, $c = 0.033$, and compared directly with the observed spectrum using a likelihood function. Equation (3) is the standard form for the calorimeter resolution function, modified to account for a weak p_{T} dependence of the coefficient of the (p_{T}^{-1}) stochastic term and to model better the resolution of low p_{T} jets by using a negative coefficient for the (p_{T}^{-2}) noise term. For brevity, we shall refer to the smeared spectrum as the NLO QCD jet p_{T} spectrum.

TABLE I. The fit parameters associated with Fig. 1. The first row lists the values of the parameters p_1, p_2, p_3, and p_4, while the remaining rows list the elements of the associated covariance matrix.

	p_1	p_2	p_3	p_4
	-1.5×10^{-3}	3.6	1.9×10^{-3}	5.2
p_1	1.4×10^{-6}	3.6×10^{-4}	-3.4×10^{-7}	6.8×10^{-5}
p_2	3.6×10^{-4}	9.2×10^{-2}	-8.4×10^{-5}	1.7×10^{-2}
p_3	-3.4×10^{-7}	-8.4×10^{-5}	1.0×10^{-7}	-2.0×10^{-5}
p_4	6.8×10^{-5}	1.7×10^{-2}	-2.0×10^{-5}	4.1×10^{-3}

The signal term $\mathrm{CI}(\Lambda)$ is modeled by subtracting the leading-order (LO) QCD jet cross section ($\mathrm{QCD_{LO}}$) from the LO jet cross section computed with a contact term. The leading-order jet p_{T} spectra are computed by generating events with and without a CI term using the program PYTHIA 6.422, the Z2 underlying event tune [17,20], and the same CTEQ PDFs used to calculate $\mathrm{QCD_{NLO}}$. The generated events are processed with the full CMS detector

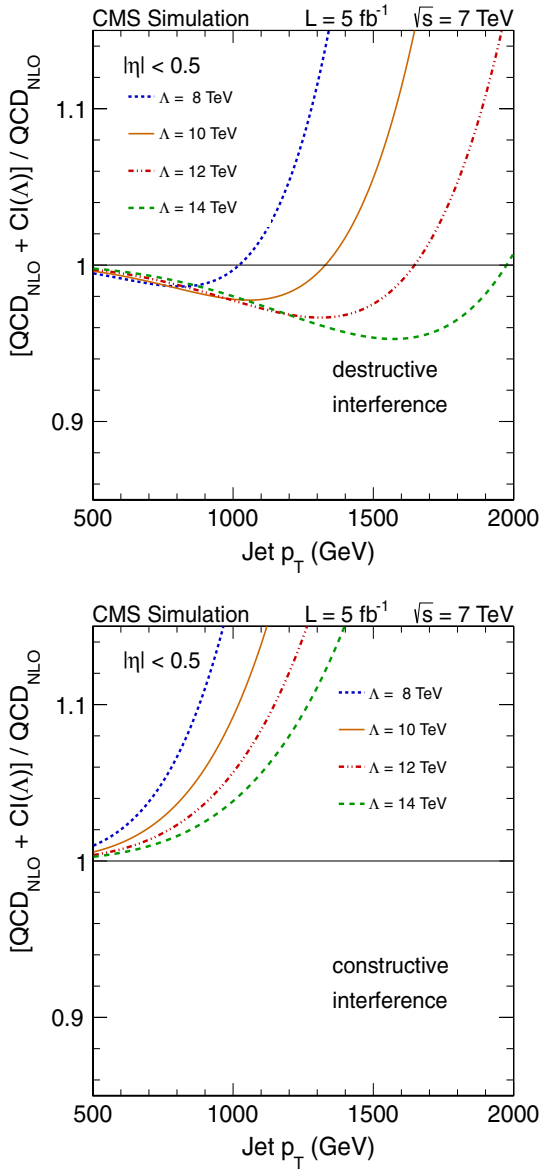

FIG. 2 (color online). The cross section ratios, $f = [\mathrm{QCD_{NLO}} + \mathrm{CI}(\Lambda)]/\mathrm{QCD_{NLO}}$, with $\Lambda = 8$, 10, 12, and 14 TeV, for models with destructive (top) and constructive (bottom) interference.

simulation program, based on GEANT4 [21]. Interactions between all quarks are included (Appendix A) and we consider models both with destructive and constructive interference between the QCD and CI amplitudes. We note that NLO corrections to the contact interaction model have recently become available [22], and we plan to use these results in future studies. These corrections are expected to change the results by less than 5%.

The jet p_T dependence of CI(Λ) is modeled by fitting the ratio $f = [\mathrm{QCD_{NLO}} + \mathrm{CI}(\Lambda)]/\mathrm{QCD_{NLO}}$ simultaneously to four PYTHIA CI models with $\Lambda = 3$, 5, 8, and 12 TeV. The fit is performed in this manner in order to construct a smooth interpolation over the four cross section ratios.

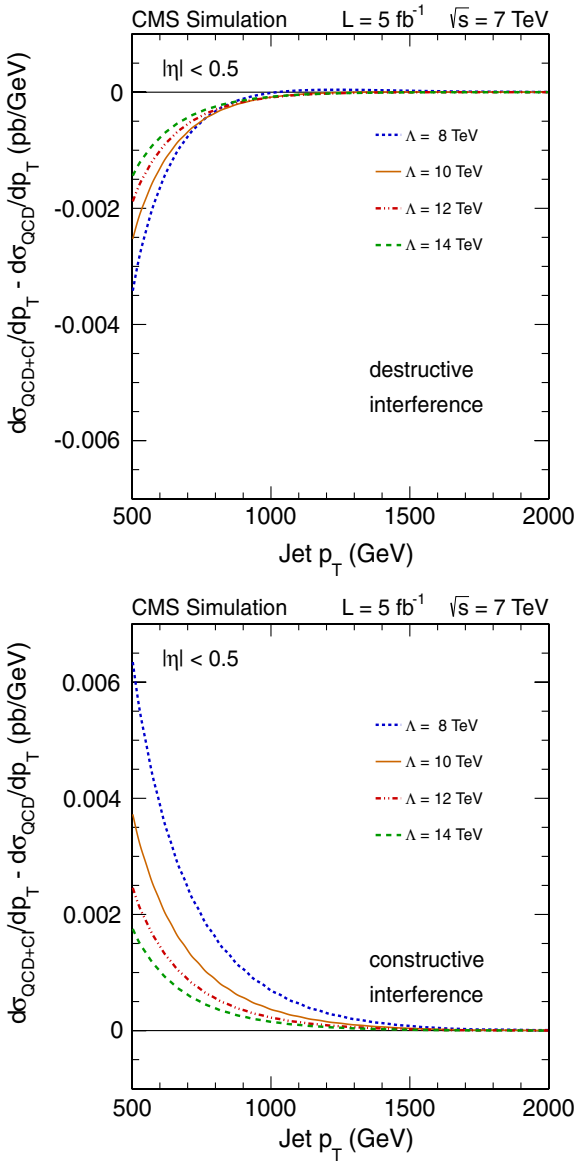

FIG. 3 (color online). The CI signal spectra, defined as $d\sigma_{\mathrm{QCD+CI}}/dp_T - d\sigma_{\mathrm{QCD}}/dp_T$ (pb/GeV) with $\Lambda = 8$, 10, 12, and 14 TeV, for models with destructive (top) and constructive (bottom) interference.

Several functional forms were investigated that gave satisfactory fits, including the ansatz [23]

$$f = 1 + p_1\left(\frac{p_T}{100\ \mathrm{GeV}}\right)^{p_2}\left(\frac{\lambda}{1\ \mathrm{TeV}^{-2}}\right) + p_3\left(\frac{p_T}{100\ \mathrm{GeV}}\right)^{p_4}\left(\frac{\lambda}{1\ \mathrm{TeV}^{-2}}\right)^2. \quad (4)$$

In a generator-level study, we verified the adequacy of the extrapolation of Eq. (4) up to 25 TeV. The results of fitting Eq. (4) to models with destructive interference are shown in Fig. 1. The fit shown in Fig. 1 uses the central values of the JES, JER, and PDF parameters and the renormalization (μ_r) and factorization (μ_f) scales set to $\mu_r = \mu_f = \mathrm{jet}p_T$. Models with constructive interference are obtained by reversing the sign of the parameter p_1. The fit parameters are given in Table I. Figures 2 and 3 show model spectra in the jet p_T range $500 \le p_T \le 2000$ GeV for values of Λ that are close to the limits reported in this paper. Figure 2 shows that the jet production cross section is enhanced at sufficiently high jet p_T. However, for interactions that interfere destructively, the cross section can decrease relative to the NLO QCD prediction. For example, for $\Lambda = 10$ TeV, the $\mathrm{QCD_{NLO}} + \mathrm{CI}$ cross section is lower than the $\mathrm{QCD_{NLO}}$ cross section for jet $p_T < 1.3$ TeV. Figure 3 shows the contact interaction signal, CI(Λ), as a function of jet p_T.

III. EXPERIMENTAL SETUP

The CMS coordinate system is right-handed with the origin at the center of the detector, the x axis directed toward the center of the LHC ring, the y axis directed upward, and the z axis directed along the counterclockwise proton beam. We define ϕ to be the azimuthal angle, θ to be the polar angle, and the pseudorapidity to be $\eta \equiv -\ln[\tan(\theta/2)]$. The central feature of the CMS apparatus is a superconducting solenoid of 6 m internal diameter, operating with a magnetic field strength of 3.8 T. Within the field volume are the silicon pixel and strip trackers and the barrel and endcap calorimeters with $|\eta| < 3$. Outside the field volume, in the forward region, there is an iron/quartz-fiber hadron calorimeter ($3 < |\eta| < 5$). Further details about the CMS detector may be found elsewhere [24].

Jets are built from the five types of reconstructed particles: photons, neutral hadrons, charged hadrons, muons, and electrons, using the CMS particle-flow reconstruction method [25] and the anti-k_T algorithm with a distance parameter of 0.7 [26–28]. The jet energy scale correction is derived as a function of the jet p_T and η, using a p_T-balancing technique [9], and applied to all components of the jet four momentum.

The results reported are based on data collected using unprescaled single-jet triggers with p_T thresholds that were changed in steps from 240 to 300 GeV during the data-taking period. The trigger thresholds were changed in response to the increase in instantaneous luminosity.

The jet trigger efficiency is constant, ~98.8%, above ~400 GeV, well below the search region. Events with hadron calorimeter noise are removed [29] and each selected event must have a primary vertex within 24 cm of the geometric center of the detector along the z axis and within 0.2 cm in the transverse x-y plane, defined by criteria described in [30]. The search is restricted to $|\eta| < 0.5$ where the effects of contact interactions are predicted to be the largest [1–4]. The jet p_T spectrum is divided into 20 p_T bins in the search region $507 \leq p_T \leq 2116$ GeV, where the bin width is approximately equal to the jet resolution σ_{p_T} given in Eq. (3). No jets are observed above 2000 GeV transverse energy.

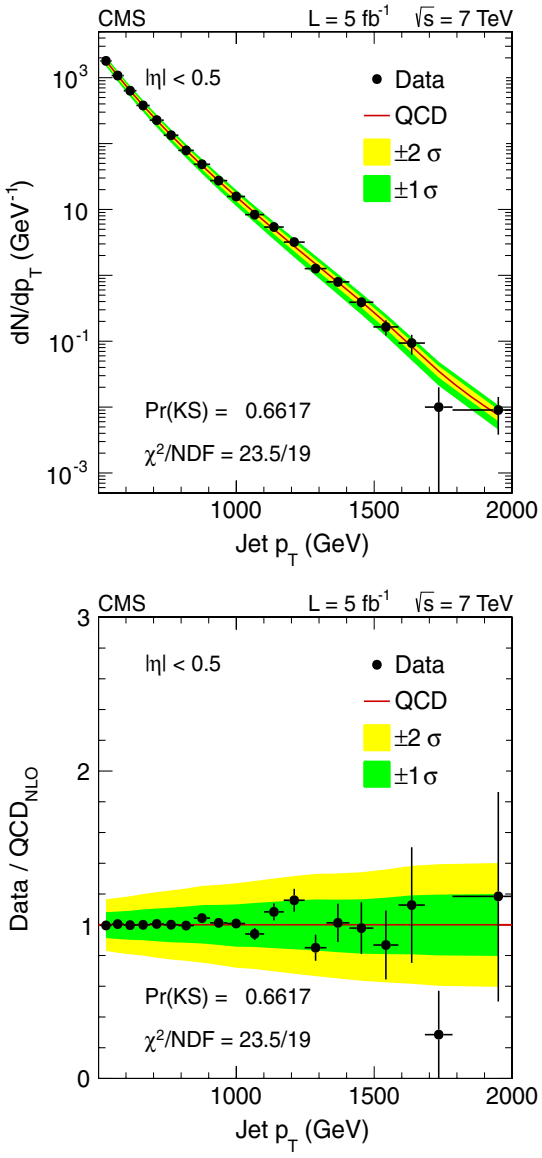

FIG. 4 (color online). The observed jet p_T spectrum compared with the NLO QCD jet p_T spectrum (top). The bands represent the total uncertainty in the prediction and incorporate the uncertainties in the PDFs, jet energy scale, jet energy resolution, the renormalization and factorization scales, and the modeling of the jet p_T dependence of the parameters in Eq. (4). The ratio of the observed to the predicted spectrum (bottom). The error bars represent the statistical uncertainties in the expected bin count.

TABLE II. The observed jet count for each jet p_T bin in the range 507–2116 GeV.

Bin	p_T (GeV)	Jets	Bin	p_T (GeV)	Jets
1	507–548	73792	11	1032–1101	576
2	548–592	47416	12	1101–1172	384
3	592–638	29185	13	1172–1248	243
4	638–686	18187	14	1248–1327	100
5	686–737	11565	15	1327–1410	66
6	737–790	7095	16	1410–1497	34
7	790–846	4413	17	1497–1588	15
8	846–905	2862	18	1588–1684	9
9	905–967	1699	19	1684–1784	1
10	967–1032	1023	20	1784–2116	3

IV. RESULTS

In Fig. 4 we compare the observed inclusive jet p_T spectrum with the NLO QCD jet p_T spectrum, which is normalized to the total observed jet count in the search region using the normalization factor $4.007 \pm 0.009(\text{stat})\ \text{fb}^{-1}$ (Sec. V). The normalization is the ratio of the observed jet count to the predicted cross section in the search region. The data and the prediction are in good agreement as indicated by two standard criteria, the Kolmogorov-Smirnov probability Pr(KS) of 0.66, and the χ^2 per number of degrees of freedom of 23.5/19. Table II lists the observed jet counts. Figure 5 compares the observed jet p_T spectrum in the search region with model spectra for different values of Λ, for models with destructive interference. Figure 6 compares the data with models with constructive interference.

V. STATISTICAL ANALYSIS

Since there are no significant deviations between the observed and predicted spectra, the results are interpreted in terms of lower limits on the CI scale Λ using the models described in Sec. II. The dominant sources of systematic uncertainties are associated with the JES, the PDFs, the JER, the renormalization (μ_r) and factorization (μ_f) scales, and the modeling parameters of Eq. (4). Nonperturbative corrections are less than 1% for transverse momenta above ~400 GeV [30], negligible compared with other uncertainties, and are therefore not applied to our analysis.

In the search region, the inclusive jet spectrum has a range of 5 orders of magnitude, which causes the limits on Λ to be sensitive to the choice of the normalization factor and the size of the data sets. We have found that a few percent change in the normalization factor can cause limits to change by as much as 50%. Therefore, for the purpose of

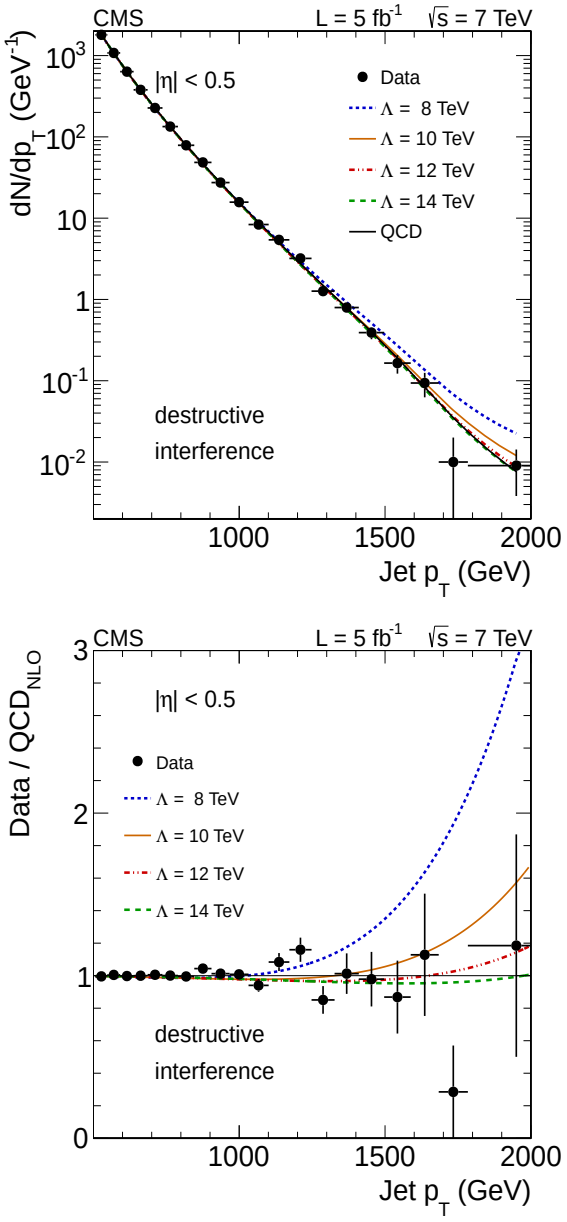

FIG. 5. The data compared with model spectra for different values of Λ for models with destructive interference (top). The ratio of these spectra to the NLO QCD jet p_{T} spectrum (bottom).

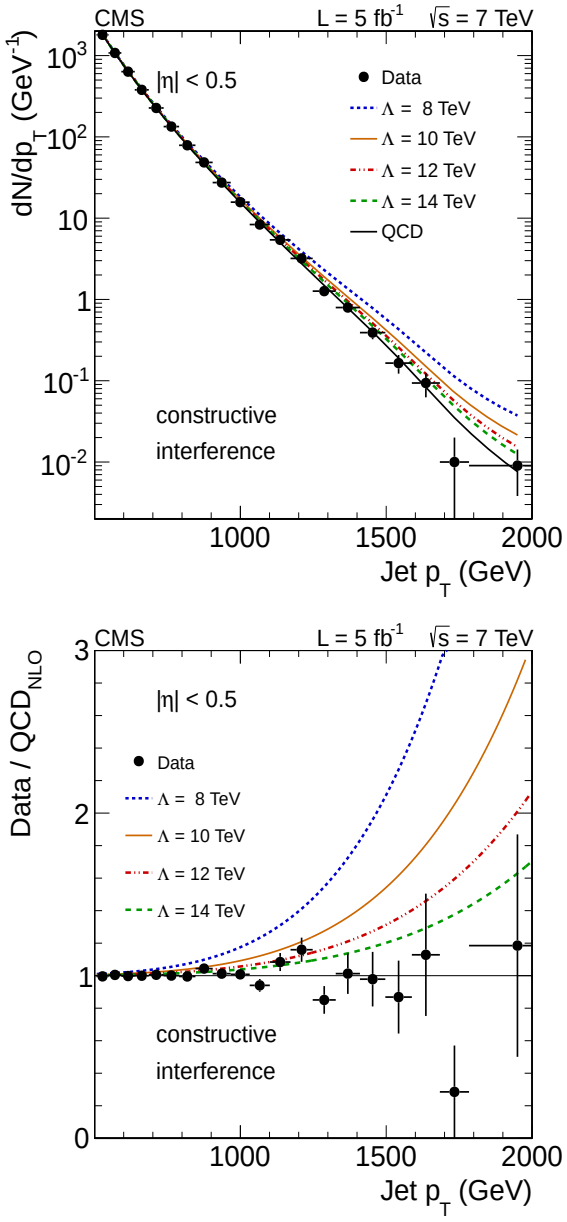

FIG. 6. The data compared to model spectra for different values of Λ for models with constructive interference (top). The ratio of these spectra to the NLO QCD jet p_{T} spectrum (bottom).

preted in terms of lower limits on the CI scale Λ using the models described in Section II. The dominant sources of systematic uncertainties are associated with the JES, the PDFs, the JER, the renormalization (μ_{r}) and factorization (μ_{f}) scales, and the modeling parameters of Eq. (4). Non-perturbative corrections are less than 1% for transverse momenta above ~400 GeV [30], are negligible compared with other uncertainties, and are therefore not applied to our analysis.

In the search region, the inclusive jet spectrum has a range of five orders of magnitude, which causes the limits on Λ to be sensitive to the choice of the normalization factor and the size of the data sets. We have found that a few percent change in the normalization factor can cause limits to change by as much as 50%. Therefore, for the purpose of computing limits, we have chosen to sidestep the issue of normalization by considering only the shape of the jet p_{T} spectrum. This we achieve by using a multi-

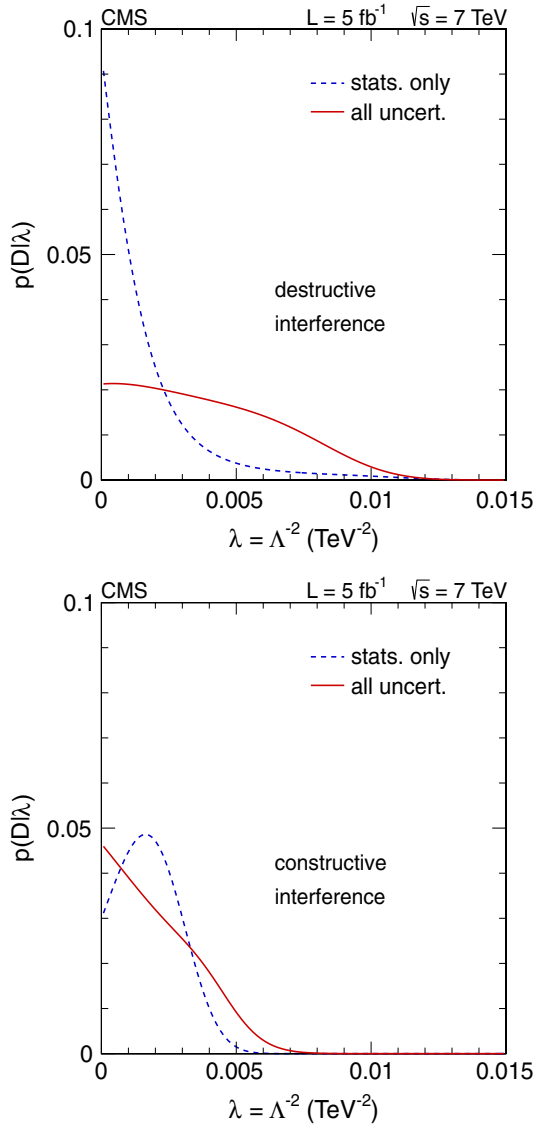

FIG. 7 (color online). The likelihood functions assuming a model with either destructive (top) or constructive (bottom) interference. The dashed curve is the likelihood function including statistical uncertainties only and the central values of all nuisance parameters. The solid curve is the likelihood marginalized over all systematic uncertainties.

A. Uncertainties

In principle, a discrete representation of the nuisance prior $\pi(\omega)$ can be constructed by sampling simultaneously the JES, JER, PDFs, and the three values of μ_f and μ_r: $p_T/2$, p_T, and $2p_T$. However, the CTEQ collaboration [19] does not provide a sampling of PDFs. Instead, CTEQ6.6 contains 44 PDF sets in which the 22 PDF parameters are shifted by approximately ± 1.64 standard deviations. If we assume the Gaussian approximation to be valid, we can construct approximate 20×20 covariance matrices for the jet spectra from the 44 PDF sets. Using these matrices, we generate ensembles of six correlated spectra: $\mathrm{QCD}_{\mathrm{NLO}}$, $\mathrm{QCD}_{\mathrm{LO}}$, and $(\mathrm{QCD} + \mathrm{CI}(\Lambda))_{\mathrm{LO}}$ with $\Lambda = 3$, 5, 8, and 12 TeV. The generation is performed for models both with destructive and constructive interference. The details of our procedure, which also includes simultaneous sampling of the JES and JER parameters, are given in Appendix B 1.

For a given set of values for the JES, JER, PDF, μ_r, and μ_f parameters, Eq. (4) is fitted to the ratio $(\mathrm{QCD}_{\mathrm{NLO}} + \mathrm{CI})/\mathrm{QCD}_{\mathrm{NLO}}$ simultaneously to the four models with $\Lambda = 3$, 5, 8, and 12 TeV. We then sample a single set of the four nuisance parameters $\omega = p_1, p_2, p_3, p_4$ from a multivariate Gaussian using the fitted values and the associated 4×4 covariance matrix. The sampling and fitting procedure is repeated 500 times, thereby generating a discrete representation of the nuisance prior $\pi(\omega)$ that incorporates all uncertainties. We have verified that our conclusions are robust with respect to variations in the size of the sample that represents $\pi(\omega)$.

B. Lower limits on Λ

We use the CL_s criterion [31,32] to compute upper limits on λ. For completeness, we give the details of these calculations in Appendix B 2. Using the procedure described in the Appendix, we obtain 95% lower limits on Λ of 9.9 TeV and 14.3 TeV for models with destructive and constructive interference, respectively. These more stringent limits supersede those published by CMS based on a measurement of the dijet angular distribution [8]. The current search is more sensitive than the earlier dijet search as evidenced by the expected limits, which for this analysis are 9.5 ± 0.6 TeV and 13.6 ± 1.6 TeV, respectively, obtained using 5 fb^{-1} of data.

Limits are also computed with a Bayesian method (Appendix B 3) using the marginal likelihood $p(D|\lambda)$ and two different priors for λ: a prior flat in λ and a reference prior [33–35]. Using a flat prior, we find lower limits on Λ of 10.6 TeV and 14.6 TeV at 95% C.L. for models with destructive and constructive interference, respectively. The corresponding limits using the reference prior are 10.1 TeV and 14.1 TeV at 95% C.L., respectively.

VI. SUMMARY

The inclusive jet p_T spectrum of 7 TeV proton-proton collision events in the ranges $507 \leq p_T \leq 2116$ GeV and $|\eta| < 0.5$ has been studied using a data set corresponding to an integrated luminosity of 5.0 fb^{-1}. The observed jet p_T spectrum is found to be in agreement with the jet p_T spectrum predicted using perturbative QCD at NLO when the predicted spectrum is convolved with the CMS jet response function and normalized to the observed spectrum in the search region. Should additional interactions exist that can be modeled as contact interactions with either destructive or constructive interference, their scale Λ is above 9.9 TeV and 14.3 TeV, respectively, at 95% C.L. We plan to extend this study to the full 8 TeV CMS data set, making use of a recently released program [36] to calculate

B. Lower limits on Λ

We use the CL_s criterion [31, 32] to compute upper limits on λ. For completeness, we give the details of these calculations in Appendix B 2. Using the procedure described in the Appendix, we obtain 95% lower limits on Λ of 9.9 TeV and 14.3 TeV for models with destructive and constructive interference, respectively. These more stringent limits supersede those published by CMS based on a measurement of the dijet angular distribution [8]. The current search is more sensitive than the earlier dijet search as evidenced by the expected limits, which for this analysis are 9.5 ± 0.6 TeV and 13.6 ± 1.6 TeV, respectively, obtained using $5\,\text{fb}^{-1}$ of data.

Limits are also computed with a Bayesian method (Appendix B 3) using the marginal likelihood $p(D|\lambda)$ and two different priors for λ: a prior flat in λ and a reference prior [33–35]. Using a flat prior, we find lower limits on Λ of 10.6 TeV and 14.6 TeV at 95% confidence level for models with destructive and constructive interference, respectively. The corresponding limits using the reference prior are 10.1 TeV and 14.1 TeV at 95% confidence level, respectively.

VI. SUMMARY

The inclusive jet p_T spectrum of 7 TeV proton-proton collision events in the ranges $507 \leq p_T \leq 2116$ GeV and $|\eta| < 0.5$ has been studied using a data set corresponding to an integrated luminosity of $5.0\,\text{fb}^{-1}$. The observed jet p_T spectrum is found to be in agreement with the jet p_T spectrum predicted using perturbative QCD at NLO when the predicted spectrum is convolved with the CMS jet response function and normalized to the observed spectrum in the search region. Should additional interactions exist that can be modeled as contact interactions with either destructive or constructive interference, their scale Λ is above 9.9 TeV and 14.3 TeV, respectively, at 95% confidence level. We plan to extend this study to the full 8 TeV CMS data set, making use of a recently released program [36] to calculate at next-to-leading order the inclusive jet p_T spectrum with contact interactions.

It is noteworthy that the limits reported in this paper, which are the most sensitive limits published to date, have been obtained reprising the classic method to search for contact interactions: namely, searching for deviations from QCD at high jet transverse momentum.

ACKNOWLEDGMENTS

We congratulate our colleagues in the CERN accelerator departments for the excellent performance of the LHC and thank the technical and administrative staffs at CERN and at other CMS institutes for their contributions to the success of the CMS effort. In addition, we gratefully acknowledge the computing centers and personnel of the Worldwide LHC Computing Grid for delivering so effectively the computing infrastructure essential to our analyses. Finally, we acknowledge the enduring support for the construction and operation of the LHC and the CMS detector provided by the following funding agencies: BMWF and FWF (Austria); FNRS and FWO (Belgium); CNPq, CAPES, FAPERJ, and FAPESP (Brazil); MEYS (Bulgaria); CERN; CAS, MoST, and NSFC (China); COLCIENCIAS (Colombia); MSES (Croatia); RPF (Cyprus); MoER, SF0690030s09 and ERDF (Estonia); Academy of Finland, MEC, and HIP (Finland); CEA and CNRS/IN2P3 (France); BMBF, DFG, and HGF (Germany); GSRT (Greece); OTKA and NKTH (Hungary); DAE and DST (India); IPM (Iran); SFI (Ireland); INFN (Italy); NRF and WCU (Korea); LAS (Lithuania); CINVESTAV, CONACYT, SEP, and UASLP-FAI (Mexico); MSI (New Zealand); PAEC (Pakistan); MSHE and NSC (Poland); FCT (Portugal); JINR (Armenia, Belarus, Georgia, Ukraine, Uzbekistan); MON, RosAtom, RAS and RFBR (Russia); MSTD (Serbia); SEIDI and CPAN (Spain); Swiss Funding Agencies (Switzerland); NSC (Taipei); ThEP, IPST and NECTEC (Thailand); TUBITAK and TAEK (Turkey); NASU (Ukraine); STFC (United Kingdom); DOE and NSF (USA).

[1] E. J. Eichten, K. D. Lane, and M. E. Peskin, Phys. Rev. Lett. **50**, 811 (1983).
[2] E. Eichten, I. Hinchliffe, K. Lane, and C. Quigg, Rev. Mod. Phys. **56**, 579 (1984).
[3] P. Chiappetta and M. Perrottet, Phys. Lett. B **253**, 489 (1991).
[4] K. Lane, "Electroweak and flavor dynamics at hadron colliders," (1996), arXiv:hep-ph/9605257 [hep-ph].
[5] F. Abe *et al.* (CDF), Phys. Rev. Lett. **79**, 2198 (1997).
[6] B. Abbott *et al.* (D0), Phys. Rev. Lett. **82**, 4769 (1999).
[7] Phys. Rev. D **87**, 015010 (2013).
[8] Chatrchyan *et al.* (CMS), JHEP **05**, 055 (2012).
[9] S. Chatrchyan *et al.* (CMS), J. Instrum. **6**, P11002 (2011).
[10] P. M. Nadolsky, H.-L. Lai, Q.-H. Cao, J. Huston, J. Pumplin, D. Stump, W.-K. Tung, and C.-P. Yuan, Phys. Rev. D **78**, 013004 (2008), arXiv:0802.0007 [hep-ph].
[11] R. Ball, V. Bertone, F. Cerutti, L. Debbio, S. Forte, A. Guffanti, J. Latorre, Rojo, and M. Ubiali, Nucl. Phys. B **849**, 296 (2011).
[12] G. Watt and R. Thorne, JHEP **08**, 052 (2012), arXiv:1205.4024.
[13] V. M. Abazov *et al.* (D0), Phys. Rev. D **85**, 052006 (2012), arXiv:1110.3771 [hep-ex].

jet in every simulated event. The jet p_T is shifted by $x\delta$ for each component of the jet energy scale uncertainty, of which there are 16, where x is a Gaussian variate of zero mean and unit variance, and δ is a jet-dependent uncertainty for a given component. The contributions from all uncertainty components are summed to obtain an overall shift in the jet p_T. From studies of dijet asymmetry and photon + jet p_T balancing, the uncertainty in the jet energy resolution is estimated to be 10% in the pseudorapidity range $|\eta| < 0.5$ [30]. We sample the jet energy resolution using a procedure identical to that used to sample the jet energy scale but using a single Gaussian variate.

C. Generating the JES/JER/PDF ensemble

Another ensemble is created, from the PDF ensembles and the JES/JER ensembles, that approximates simultaneous sampling from the JES, JER, PDF, renormalization, and factorization parameters. We pick at random a correlated set of six spectra from the PDF ensembles and a correlated set of five spectral residuals from the JES/JER ensembles. The JES/JER spectral residuals $\delta\sigma$ are added to the corresponding shifted spectrum from the PDF ensembles, thereby creating a spectrum in which the JES, JER, PDF, μ_r, and μ_f parameters have been randomly shifted. The NLO QCD spectrum (from the PDF ensembles) is shifted using the LO QCD JES/JER spectral residuals in order to approximate the effect of the JES and JER uncertainties in this spectrum.

The result of the above procedure is an ensemble of sets of properly correlated spectra $\mathrm{QCD_{NLO}} + \mathrm{CI}(\Lambda)$ with $\Lambda = 3$, 5, 8, and 12 TeV, in which the JES, JER, PDF, μ_r, and μ_f parameters vary randomly. The ansatz in Eq. (4) is then fitted to the quartet of ratios $[\mathrm{QCD_{NLO}} + \mathrm{CI}(\Lambda)]/\mathrm{QCD_{NLO}}$ as described in Sec. VA to obtain parameter values for p_1, p_2, p_3, and p_4. Five hundred sets of these parameters are generated, constituting a discrete approximation to the prior $\pi(\omega) \equiv \pi(p_1, p_2, p_3, p_4)$.

2. $\mathrm{CL_s}$ calculation

Since $\mathrm{CL_s}$ is a criterion rather than a method, it is necessary to document exactly how a $\mathrm{CL_s}$ limit is calculated. Such a calculation requires two elements: a test statistic Q that depends on the quantity of interest and its sampling distribution for two different hypotheses, here $\lambda > 0$, which we denote by H_λ, and $\lambda = 0$, which we denote by H_0. H_λ is the signal plus background hypothesis while H_0 is the background-only hypothesis. For this study, we use the statistic

$$Q(\lambda) = t(D, \lambda) \equiv -2\ln[p(D|\lambda)/p(D|0)], \quad \text{(B2)}$$

where $p(D|\lambda)$ is the marginal likelihood

$$p(D|\lambda) = \int p(D|\lambda, \omega)\pi(\omega)\, d\omega \approx \frac{1}{M}\sum_{m=1}^{M} p(D|\lambda, \omega_m), \quad \text{(B3)}$$

where $M = 500$ is the number of points $\omega = p_1, p_2, p_3, p_4$ sampled from the nuisance prior $\pi(\omega)$ described in Appendix B 1. We compute the sampling distributions

$$p(Q|H_\lambda) = \int \delta[Q - t(D, \lambda)]p(D|\lambda)dD, \quad \text{(B4)}$$

and

$$p(Q|H_0) = \int \delta[Q - t(D, \lambda)]p(D|0)dD, \quad \text{(B5)}$$

pertaining to the hypotheses H_λ and H_0, respectively, and solve

$$\mathrm{CL_s} \equiv p(\lambda)/p(0) = 0.05, \quad \text{(B6)}$$

to obtain a 95% confidence level ($\mathrm{CL_s}$) upper limit on λ, where the p-value $p(\lambda)$ is defined by

$$p(\lambda) = \Pr[Q(\lambda) > Q_0(\lambda)], \quad \text{(B7)}$$

and Q_0 is the observed value of Q.

In practice, the $\mathrm{CL_s}$ limits are approximated as follows:

(1) Choose a value of λ, say λ^*, and compute the observed value of Q, $Q_0(\lambda^*)$.
(2) Choose at random one of the $M = 500$ sets of nuisance parameters p_1, p_2, p_3, and p_4.
(3) Generate a spectrum of $K = 20$ counts, D, according to the multinomial distribution, Eq. (5), with $\lambda = \lambda^*$, which corresponds to the hypothesis H_λ. Compute $Q = t(D, \lambda^*)$ and keep track of how often $Q(\lambda^*) > Q_0(\lambda^*)$. Call this count n_λ.
(4) Generate another set of 20 counts, D, but with $\lambda = 0$, corresponding to the hypothesis H_0. Compute $Q = t(D, \lambda^*)$ and keep track of how often $Q(\lambda^*) > Q_0(\lambda^*)$. Call this count n_0.
(5) Repeat 25 000 times steps 2 to 4, compute $\mathrm{CL_s} \approx n_\lambda/n_0$, and report $\lambda = \lambda^*$ as the upper limit on λ at 95% C.L. if $\mathrm{CL_s}$ is sufficiently close to 0.05; otherwise, keep repeating steps 1 to 4 with different values of λ. The algorithm starts with two values of λ that are likely to bracket the solution and the solution is found using a binary search, which typically requires about 10–15 iterations.

3. Bayesian calculation

The Bayesian limit calculations use the marginal likelihood, Eq. (B3), and two different (formal) priors $\pi(\lambda)$: a prior flat in λ and a reference prior [33–35], which we calculate numerically [35]. An upper limit on λ, λ^* is computed by solving

$$\int_0^{\lambda^*} p(D|\lambda)\pi(\lambda)d\lambda/p(D) = 0.95, \quad \text{(B8)}$$

where $p(D)$ is a normalization constant. The integrals are performed using numerical quadrature.

[1] E. J. Eichten, K. D. Lane, and M. E. Peskin, Phys. Rev. Lett. **50**, 811 (1983).
[2] E. Eichten, I. Hinchliffe, K. Lane, and C. Quigg, Rev. Mod. Phys. **56**, 579 (1984).
[3] P. Chiappetta and M. Perrottet, Phys. Lett. B **253**, 489 (1991).
[4] K. Lane, arXiv:hep-ph/9605257.
[5] F. Abe *et al.* (CDF Collaboration), Phys. Rev. Lett. **79**, 2198 (1997).
[6] B. Abbott *et al.* (D0 Collaboration), Phys. Rev. Lett. **82**, 4769 (1999).
[7] ATLAS Collaboration, Phys. Rev. D **87**, 015010 (2013).
[8] CMS Collaboration, J. High Energy Phys. 05 (2012) 055.
[9] CMS Collaboration, JINST **6**, P11002 (2011).
[10] P. M. Nadolsky, H.-L. Lai, Q.-H. Cao, J. Huston, J. Pumplin, D. Stump, W.-K. Tung, and C.-P. Yuan, Phys. Rev. D **78**, 013004 (2008).
[11] R. Ball, V. Bertone, F. Cerutti, L. Debbio, S. Forte, A. Guffanti, J. Latorre, Rojo, and M. Ubiali, Nucl. Phys. **B849**, 296 (2011).
[12] G. Watt and R. Thorne, J. High Energy Phys. 08 (2012) 052.
[13] V. M. Abazov *et al.* (D0 Collaboration), Phys. Rev. D **85**, 052006 (2012).
[14] T. Aaltonen *et al.* (CDF Collaboration), Phys. Rev. D **78**, 052006 (2008).
[15] F. Abe *et al.* (CDF Collaboration), Phys. Rev. Lett. **77**, 438 (1996).
[16] B. Abbott *et al.* (D0 Collaboration), Phys. Rev. D **62**, 031101 (2000).
[17] K. Lane and S. Mrenna, Phys. Rev. D **67**, 115011 (2003).
[18] T. Kluge, K. Rabbertz, and M. Wobisch, arXiv:hepph/0609285.
[19] H. Lai, J. Huston, Z. Li, P. Nadolsky, J. Pumplin, D. Stump, and C.-P. Yuan, Phys. Rev. D **82**, 054021 (2010).
[20] T. Sjöstrand, S. Mrenna, and P. Skands, J. High Energy Phys. 05 (2006) 026.
[21] S. Agostinelli *et al.* (GEANT4 Collaboration), Nucl. Instrum. Methods Phys. Res., Sect. A **506**, 250 (2003).
[22] J. Gao, C. S. Li, J. Wang, H. X. Zhu, and C.-P. Yuan, Phys. Rev. Lett. **106**, 142001 (2011).
[23] J. F. Owens (private communication).
[24] CMS Collaboration, J. Phys. G **34**, 995 (2007).
[25] CMS Collaboration, CMS Physics Analysis Summary Report No CMS-PAS-JME-10-003, 2010, http://cds.cern.ch/record/1279362.
[26] G. C. Blazey, J. R. Dittmann, S. D. Ellis, V. D. Elvira, K. Frame, S. Grinstein, R. Hirosky, R. Piegaia, H. Schellman, R. Snihur, V. Sorin, and D. Zeppenfeld, Proceedings of the Run II QCD and Weak Boson Physics Workshop (2000), arXiv:hep-ex/0005012.
[27] S. Ellis, J. Huston, K. Hatakeyama, P. Loch, and M. Toennesmann, Prog. Part. Nucl. Phys. **60**, 484 (2008).
[28] C. Buttar *et al.*, arXiv:0803.0678.
[29] CMS Collaboration, JINST **5**, T03014 (2009).
[30] CMS Collaboration, Phys. Rev. Lett. **107**, 132001 (2011).
[31] A. Read, J. Phys. G **28**, 2693 (2002).
[32] T. Junk, Nucl. Instrum. Methods Phys. Res., Sect. A **434**, 435 (1999).
[33] J. Berger, J. Bernardo, and D. Sun, Ann. Stat. **37**, 905 (2009).
[34] D. Sun and J. Berger, Biometrika **85**, 55 (1998).
[35] L. Demortier, S. Jain, and H. B. Prosper, Phys. Rev. D **82**, 034002 (2010).
[36] J. Gao, arXiv:1301.7263.

S. Chatrchyan,[1] V. Khachatryan,[1] A. M. Sirunyan,[1] A. Tumasyan,[1] W. Adam,[2] E. Aguilo,[2] T. Bergauer,[2] M. Dragicevic,[2] J. Erö,[2] C. Fabjan,[2,b] M. Friedl,[2] R. Frühwirth,[2,b] V. M. Ghete,[2] N. Hörmann,[2] J. Hrubec,[2] M. Jeitler,[2,b] W. Kiesenhofer,[2] V. Knünz,[2] M. Krammer,[2,b] I. Krätschmer,[2] D. Liko,[2] I. Mikulec,[2] M. Pernicka,[2,a] D. Rabady,[2,c] B. Rahbaran,[2] C. Rohringer,[2] H. Rohringer,[2] R. Schöfbeck,[2] J. Strauss,[2] A. Taurok,[2] W. Waltenberger,[2] C.-E. Wulz,[2,b] V. Mossolov,[3] N. Shumeiko,[3] J. Suarez Gonzalez,[3] M. Bansal,[4] S. Bansal,[4] T. Cornelis,[4] E. A. De Wolf,[4] X. Janssen,[4] S. Luyckx,[4] L. Mucibello,[4] S. Ochesanu,[4] B. Roland,[4] R. Rougny,[4] M. Selvaggi,[4] H. Van Haevermaet,[4] P. Van Mechelen,[4] N. Van Remortel,[4] A. Van Spilbeeck,[4] F. Blekman,[5] S. Blyweert,[5] J. D'Hondt,[5] R. Gonzalez Suarez,[5] A. Kalogeropoulos,[5] M. Maes,[5] A. Olbrechts,[5] W. Van Doninck,[5] P. Van Mulders,[5] G. P. Van Onsem,[5] I. Villella,[5] B. Clerbaux,[6] G. De Lentdecker,[6] V. Dero,[6] A. P. R. Gay,[6] T. Hreus,[6] A. Léonard,[6] P. E. Marage,[6] A. Mohammadi,[6] T. Reis,[6] L. Thomas,[6] C. Vander Velde,[6] P. Vanlaer,[6] J. Wang,[6] V. Adler,[7] K. Beernaert,[7] A. Cimmino,[7] S. Costantini,[7] G. Garcia,[7] M. Grunewald,[7] B. Klein,[7] J. Lellouch,[7] A. Marinov,[7] J. Mccartin,[7] A. A. Ocampo Rios,[7] D. Ryckbosch,[7] N. Strobbe,[7] F. Thyssen,[7] M. Tytgat,[7] S. Walsh,[7] E. Yazgan,[7] N. Zaganidis,[7] S. Basegmez,[8] G. Bruno,[8] R. Castello,[8] L. Ceard,[8] C. Delaere,[8] T. du Pree,[8] D. Favart,[8] L. Forthomme,[8] A. Giammanco,[8,d] J. Hollar,[8] V. Lemaitre,[8] J. Liao,[8] O. Militaru,[8] C. Nuttens,[8] D. Pagano,[8] A. Pin,[8] K. Piotrzkowski,[8] J. M. Vizan Garcia,[8] N. Beliy,[9] T. Caebergs,[9] E. Daubie,[9] G. H. Hammad,[9] G. A. Alves,[10] M. Correa Martins Junior,[10] T. Martins,[10] M. E. Pol,[10] M. H. G. Souza,[10] W. L. Aldá Júnior,[11] W. Carvalho,[11] A. Custódio,[11] E. M. Da Costa,[11] D. De Jesus Damiao,[11] C. De Oliveira Martins,[11] S. Fonseca De Souza,[11] H. Malbouisson,[11] M. Malek,[11] D. Matos Figueiredo,[11] L. Mundim,[11] H. Nogima,[11] W. L. Prado Da Silva,[11] A. Santoro,[11] L. Soares Jorge,[11] A. Sznajder,[11] A. Vilela Pereira,[11] T. S. Anjos,[12b] C. A. Bernardes,[12b] F. A. Dias,[12a,e] T. R. Fernandez Perez Tomei,[12a] E. M. Gregores,[12b] C. Lagana,[12a] F. Marinho,[12a] P. G. Mercadante,[12b] S. F. Novaes,[12a] Sandra S. Padula,[12a] V. Genchev,[13,c] P. Iaydjiev,[13,c] S. Piperov,[13] M. Rodozov,[13] S. Stoykova,[13] G. Sultanov,[13] V. Tcholakov,[13] R. Trayanov,[13] M. Vutova,[13] A. Dimitrov,[14] R. Hadjiiska,[14] V. Kozhuharov,[14]

L. Litov,[14] B. Pavlov,[14] P. Petkov,[14] J. G. Bian,[15] G. M. Chen,[15] H. S. Chen,[15] C. H. Jiang,[15] D. Liang,[15] S. Liang,[15] X. Meng,[15] J. Tao,[15] J. Wang,[15] X. Wang,[15] Z. Wang,[15] H. Xiao,[15] M. Xu,[15] J. Zang,[15] Z. Zhang,[15] C. Asawatangtrakuldee,[16] Y. Ban,[16] Y. Guo,[16] W. Li,[16] S. Liu,[16] Y. Mao,[16] S. J. Qian,[16] H. Teng,[16] D. Wang,[16] L. Zhang,[16] W. Zou,[16] C. Avila,[17] J. P. Gomez,[17] B. Gomez Moreno,[17] A. F. Osorio Oliveros,[17] J. C. Sanabria,[17] N. Godinovic,[18] D. Lelas,[18] R. Plestina,[18,f] D. Polic,[18] I. Puljak,[18,c] Z. Antunovic,[19] M. Kovac,[19] V. Brigljevic,[20] S. Duric,[20] K. Kadija,[20] J. Luetic,[20] D. Mekterovic,[20] S. Morovic,[20] A. Attikis,[21] M. Galanti,[21] G. Mavromanolakis,[21] J. Mousa,[21] C. Nicolaou,[21] F. Ptochos,[21] P. A. Razis,[21] M. Finger,[22] M. Finger, Jr.,[22] Y. Assran,[23,g] S. Elgammal,[23,h] A. Ellithi Kamel,[23,i] M. A. Mahmoud,[23,j] A. Mahrous,[23,k] A. Radi,[23,l,m] M. Kadastik,[24] M. Müntel,[24] M. Raidal,[24] L. Rebane,[24] A. Tiko,[24] P. Eerola,[25] G. Fedi,[25] M. Voutilainen,[25] J. Härkönen,[26] A. Heikkinen,[26] V. Karimäki,[26] R. Kinnunen,[26] M. J. Kortelainen,[26] T. Lampén,[26] K. Lassila-Perini,[26] S. Lehti,[26] T. Lindén,[26] P. Luukka,[26] T. Mäenpää,[26] T. Peltola,[26] E. Tuominen,[26] J. Tuominiemi,[26] E. Tuovinen,[26] D. Ungaro,[26] L. Wendland,[26] K. Banzuzi,[27] A. Karjalainen,[27] A. Korpela,[27] T. Tuuva,[27] M. Besancon,[28] S. Choudhury,[28] M. Dejardin,[28] D. Denegri,[28] B. Fabbro,[28] J. L. Faure,[28] F. Ferri,[28] S. Ganjour,[28] A. Givernaud,[28] P. Gras,[28] G. Hamel de Monchenault,[28] P. Jarry,[28] E. Locci,[28] J. Malcles,[28] L. Millischer,[28] A. Nayak,[28] J. Rander,[28] A. Rosowsky,[28] M. Titov,[28] S. Baffioni,[29] F. Beaudette,[29] L. Benhabib,[29] L. Bianchini,[29] M. Bluj,[29,n] P. Busson,[29] C. Charlot,[29] N. Daci,[29] T. Dahms,[29] M. Dalchenko,[29] L. Dobrzynski,[29] A. Florent,[29] R. Granier de Cassagnac,[29] M. Haguenauer,[29] P. Miné,[29] C. Mironov,[29] I. N. Naranjo,[29] M. Nguyen,[29] C. Ochando,[29] P. Paganini,[29] D. Sabes,[29] R. Salerno,[29] Y. Sirois,[29] C. Veelken,[29] A. Zabi,[29] J.-L. Agram,[30,o] J. Andrea,[30] D. Bloch,[30] D. Bodin,[30] J.-M. Brom,[30] M. Cardaci,[30] E. C. Chabert,[30] C. Collard,[30] E. Conte,[30,o] F. Drouhin,[30,o] J.-C. Fontaine,[30,o] D. Gelé,[30] U. Goerlach,[30] P. Juillot,[30] A.-C. Le Bihan,[30] P. Van Hove,[30] F. Fassi,[31] D. Mercier,[31] S. Beauceron,[32] N. Beaupere,[32] O. Bondu,[32] G. Boudoul,[32] J. Chasserat,[32] R. Chierici,[32,c] D. Contardo,[32] P. Depasse,[32] H. El Mamouni,[32] J. Fay,[32] S. Gascon,[32] M. Gouzevitch,[32] B. Ille,[32] T. Kurca,[32] M. Lethuillier,[32] L. Mirabito,[32] S. Perries,[32] L. Sgandurra,[32] V. Sordini,[32] Y. Tschudi,[32] P. Verdier,[32] S. Viret,[32] Z. Tsamalaidze,[33,p] C. Autermann,[34] S. Beranek,[34] B. Calpas,[34] M. Edelhoff,[34] L. Feld,[34] N. Heracleous,[34] O. Hindrichs,[34] R. Jussen,[34] K. Klein,[34] J. Merz,[34] A. Ostapchuk,[34] A. Perieanu,[34] F. Raupach,[34] J. Sammet,[34] S. Schael,[34] D. Sprenger,[34] H. Weber,[34] B. Wittmer,[34] V. Zhukov,[34,q] M. Ata,[35] J. Caudron,[35] E. Dietz-Laursonn,[35] D. Duchardt,[35] M. Erdmann,[35] R. Fischer,[35] A. Güth,[35] T. Hebbeker,[35] C. Heidemann,[35] K. Hoepfner,[35] D. Klingebiel,[35] P. Kreuzer,[35] M. Merschmeyer,[35] A. Meyer,[35] M. Olschewski,[35] P. Papacz,[35] H. Pieta,[35] H. Reithler,[35] S. A. Schmitz,[35] L. Sonnenschein,[35] J. Steggemann,[35] D. Teyssier,[35] S. Thüer,[35] M. Weber,[35] M. Bontenackels,[36] V. Cherepanov,[36] Y. Erdogan,[36] G. Flügge,[36] H. Geenen,[36] M. Geisler,[36] W. Haj Ahmad,[36] F. Hoehle,[36] B. Kargoll,[36] T. Kress,[36] Y. Kuessel,[36] J. Lingemann,[36,c] A. Nowack,[36] L. Perchalla,[36] O. Pooth,[36] P. Sauerland,[36] A. Stahl,[36] M. Aldaya Martin,[37] J. Behr,[37] W. Behrenhoff,[37] U. Behrens,[37] M. Bergholz,[37,r] A. Bethani,[37] K. Borras,[37] A. Burgmeier,[37] A. Cakir,[37] L. Calligaris,[37] A. Campbell,[37] E. Castro,[37] F. Costanza,[37] D. Dammann,[37] C. Diez Pardos,[37] G. Eckerlin,[37] D. Eckstein,[37] G. Flucke,[37] A. Geiser,[37] I. Glushkov,[37] P. Gunnellini,[37] S. Habib,[37] J. Hauk,[37] G. Hellwig,[37] H. Jung,[37] M. Kasemann,[37] P. Katsas,[37] C. Kleinwort,[37] H. Kluge,[37] A. Knutsson,[37] M. Krämer,[37] D. Krücker,[37] E. Kuznetsova,[37] W. Lange,[37] J. Leonard,[37] W. Lohmann,[37,r] B. Lutz,[37] R. Mankel,[37] I. Marfin,[37] M. Marienfeld,[37] I.-A. Melzer-Pellmann,[37] A. B. Meyer,[37] J. Mnich,[37] A. Mussgiller,[37] S. Naumann-Emme,[37] O. Novgorodova,[37] J. Olzem,[37] H. Perrey,[37] A. Petrukhin,[37] D. Pitzl,[37] A. Raspereza,[37] P. M. Ribeiro Cipriano,[37] C. Riedl,[37] E. Ron,[37] M. Rosin,[37] J. Salfeld-Nebgen,[37] R. Schmidt,[37,r] T. Schoerner-Sadenius,[37] N. Sen,[37] A. Spiridonov,[37] M. Stein,[37] R. Walsh,[37] C. Wissing,[37] V. Blobel,[38] H. Enderle,[38] J. Erfle,[38] U. Gebbert,[38] M. Görner,[38] M. Gosselink,[38] J. Haller,[38] T. Hermanns,[38] R. S. Höing,[38] K. Kaschube,[38] G. Kaussen,[38] H. Kirschenmann,[38] R. Klanner,[38] J. Lange,[38] F. Nowak,[38] T. Peiffer,[38] N. Pietsch,[38] D. Rathjens,[38] C. Sander,[38] H. Schettler,[38] P. Schleper,[38] E. Schlieckau,[38] A. Schmidt,[38] M. Schröder,[38] T. Schum,[38] M. Seidel,[38] J. Sibille,[38,s] V. Sola,[38] H. Stadie,[38] G. Steinbrück,[38] J. Thomsen,[38] L. Vanelderen,[38] C. Barth,[39] J. Berger,[39] C. Böser,[39] T. Chwalek,[39] W. De Boer,[39] A. Descroix,[39] A. Dierlamm,[39] M. Feindt,[39] M. Guthoff,[39,c] C. Hackstein,[39] F. Hartmann,[39,c] T. Hauth,[39,c] M. Heinrich,[39] H. Held,[39] K. H. Hoffmann,[39] U. Husemann,[39] I. Katkov,[39,q] J. R. Komaragiri,[39] P. Lobelle Pardo,[39] D. Martschei,[39] S. Mueller,[39] Th. Müller,[39] M. Niegel,[39] A. Nürnberg,[39] O. Oberst,[39] A. Oehler,[39] J. Ott,[39] G. Quast,[39] K. Rabbertz,[39] F. Ratnikov,[39] N. Ratnikova,[39] S. Röcker,[39] F.-P. Schilling,[39] G. Schott,[39] H. J. Simonis,[39] F. M. Stober,[39] D. Troendle,[39] R. Ulrich,[39] J. Wagner-Kuhr,[39] S. Wayand,[39] T. Weiler,[39] M. Zeise,[39] G. Anagnostou,[40] G. Daskalakis,[40] T. Geralis,[40] S. Kesisoglou,[40] A. Kyriakis,[40] D. Loukas,[40] I. Manolakos,[40] A. Markou,[40] C. Markou,[40] E. Ntomari,[40] L. Gouskos,[41] T. J. Mertzimekis,[41] A. Panagiotou,[41] N. Saoulidou,[41] I. Evangelou,[42] C. Foudas,[42] P. Kokkas,[42]

N. Manthos,[42] I. Papadopoulos,[42] V. Patras,[42] G. Bencze,[43] C. Hajdu,[43] P. Hidas,[43] D. Horvath,[43,t] F. Sikler,[43] V. Veszpremi,[43] G. Vesztergombi,[43,u] N. Beni,[44] S. Czellar,[44] J. Molnar,[44] J. Palinkas,[44] Z. Szillasi,[44] J. Karancsi,[45] P. Raics,[45] Z. L. Trocsanyi,[45] B. Ujvari,[45] S. B. Beri,[46] V. Bhatnagar,[46] N. Dhingra,[46] R. Gupta,[46] M. Kaur,[46] M. Z. Mehta,[46] N. Nishu,[46] L. K. Saini,[46] A. Sharma,[46] J. B. Singh,[46] Ashok Kumar,[47] Arun Kumar,[47] S. Ahuja,[47] A. Bhardwaj,[47] B. C. Choudhary,[47] S. Malhotra,[47] M. Naimuddin,[47] K. Ranjan,[47] V. Sharma,[47] R. K. Shivpuri,[47] S. Banerjee,[48] S. Bhattacharya,[48] S. Dutta,[48] B. Gomber,[48] Sa. Jain,[48] Sh. Jain,[48] R. Khurana,[48] S. Sarkar,[48] M. Sharan,[48] A. Abdulsalam,[49] D. Dutta,[49] S. Kailas,[49] V. Kumar,[49] A. K. Mohanty,[49,c] L. M. Pant,[49] P. Shukla,[49] T. Aziz,[50] S. Ganguly,[50] M. Guchait,[50,v] A. Gurtu,[50,w] M. Maity,[50,x] G. Majumder,[50] K. Mazumdar,[50] G. B. Mohanty,[50] B. Parida,[50] K. Sudhakar,[50] N. Wickramage,[50] S. Banerjee,[51] S. Dugad,[51] H. Arfaei,[52,y] H. Bakhshiansohi,[52] S. M. Etesami,[52,z] A. Fahim,[52,y] M. Hashemi,[52,aa] H. Hesari,[52] A. Jafari,[52] M. Khakzad,[52] M. Mohammadi Najafabadi,[52] S. Paktinat Mehdiabadi,[52] B. Safarzadeh,[52,bb] M. Zeinali,[52] M. Abbrescia,[53a,53b] L. Barbone,[53a,53b] C. Calabria,[53a,53b,c] S. S. Chhibra,[53a,53b] A. Colaleo,[53a] D. Creanza,[53a,53c] N. De Filippis,[53a,53c,c] M. De Palma,[53a,53b] L. Fiore,[53a] G. Iaselli,[53a,53c] G. Maggi,[53a,53c] M. Maggi,[53a] B. Marangelli,[53a,53b] S. My,[53a,53c] S. Nuzzo,[53a,53b] N. Pacifico,[53a] A. Pompili,[53a,53b] G. Pugliese,[53a,53c] G. Selvaggi,[53a,53b] L. Silvestris,[53a] G. Singh,[53a,53b] R. Venditti,[53a,53b] P. Verwilligen,[53a] G. Zito,[53a] G. Abbiendi,[54a] A. C. Benvenuti,[54a] D. Bonacorsi,[54a,54b] S. Braibant-Giacomelli,[54a,54b] L. Brigliadori,[54a,54b] P. Capiluppi,[54a,54b] A. Castro,[54a,54b] F. R. Cavallo,[54a] M. Cuffiani,[54a,54b] G. M. Dallavalle,[54a] F. Fabbri,[54a] A. Fanfani,[54a,54b] D. Fasanella,[54a,54b] P. Giacomelli,[54a] C. Grandi,[54a] L. Guiducci,[54a,54b] S. Marcellini,[54a] G. Masetti,[54a] M. Meneghelli,[54a,54b,c] A. Montanari,[54a] F. L. Navarria,[54a,54b] F. Odorici,[54a] A. Perrotta,[54a] F. Primavera,[54a,54b] A. M. Rossi,[54a,54b] T. Rovelli,[54a,54b] G. P. Siroli,[54a,54b] N. Tosi,[54a] R. Travaglini,[54a,54b] S. Albergo,[55a,55b] G. Cappello,[55a,55b] M. Chiorboli,[55a,55b] S. Costa,[55a,55b] R. Potenza,[55a,55b] A. Tricomi,[55a,55b] C. Tuve,[55a,55b] G. Barbagli,[56a] V. Ciulli,[56a,56b] C. Civinini,[56a] R. D'Alessandro,[56a,56b] E. Focardi,[56a,56b] S. Frosali,[56a,56b] E. Gallo,[56a] S. Gonzi,[56a,56b] M. Meschini,[56a] S. Paoletti,[56a] G. Sguazzoni,[56a] A. Tropiano,[56a,56b] L. Benussi,[57] S. Bianco,[57] S. Colafranceschi,[57,cc] F. Fabbri,[57] D. Piccolo,[57] P. Fabbricatore,[58a] R. Musenich,[58a] S. Tosi,[58a,58b] A. Benaglia,[59a] F. De Guio,[59a,59b] L. Di Matteo,[59a,59b,c] S. Fiorendi,[59a,59b] S. Gennai,[59a,c] A. Ghezzi,[59a,59b] S. Malvezzi,[59a] R. A. Manzoni,[59a,59b] A. Martelli,[59a,59b] A. Massironi,[59a,59b] D. Menasce,[59a] L. Moroni,[59a] M. Paganoni,[59a,59b] D. Pedrini,[59a] S. Ragazzi,[59a,59b] N. Redaelli,[59a] S. Sala,[59a] T. Tabarelli de Fatis,[59a,59b] S. Buontempo,[60a] C. A. Carrillo Montoya,[60a] N. Cavallo,[60a,60c] A. De Cosa,[60a,60b,c] O. Dogangun,[60a,60b] F. Fabozzi,[60a,60c] A. O. M. Iorio,[60a,60b] L. Lista,[60a] S. Meola,[60a,60d,dd] M. Merola,[60a] P. Paolucci,[60a,c] P. Azzi,[61a] N. Bacchetta,[61a,c] D. Bisello,[61a,61b] A. Branca,[61a,61b,c] R. Carlin,[61a,61b] P. Checchia,[61a] T. Dorigo,[61a] U. Dosselli,[61a] F. Gasparini,[61a,61b] A. Gozzelino,[61a] K. Kanishchev,[61a,61c] S. Lacaprara,[61a] I. Lazzizzera,[61a,61c] M. Margoni,[61a,61b] A. T. Meneguzzo,[61a,61b] J. Pazzini,[61a,61b] N. Pozzobon,[61a,61b] P. Ronchese,[61a,61b] F. Simonetto,[61a,61b] E. Torassa,[61a] M. Tosi,[61a,61b] S. Vanini,[61a,61b] P. Zotto,[61a,61b] A. Zucchetta,[61a,61b] G. Zumerle,[61a,61b] M. Gabusi,[62a,62b] S. P. Ratti,[62a,62b] C. Riccardi,[62a,62b] P. Torre,[62a,62b] P. Vitulo,[62a,62b] M. Biasini,[63a,63b] G. M. Bilei,[63a] L. Fanò,[63a,63b] P. Lariccia,[63a,63b] G. Mantovani,[63a,63b] M. Menichelli,[63a] A. Nappi,[63a,63b,a] F. Romeo,[63a,63b] A. Saha,[63a] A. Santocchia,[63a,63b] A. Spiezia,[63a,63b] S. Taroni,[63a,63b] P. Azzurri,[64a,64c] G. Bagliesi,[64a] J. Bernardini,[64a] T. Boccali,[64a] G. Broccolo,[64a,64c] R. Castaldi,[64a] R. T. D'Agnolo,[64a,64c,c] R. Dell'Orso,[64a] F. Fiori,[64a,64b,c] L. Foà,[64a,64c] A. Giassi,[64a] A. Kraan,[64a] F. Ligabue,[64a,64c] T. Lomtadze,[64a] L. Martini,[64a,ee] A. Messineo,[64a,64b] F. Palla,[64a] A. Rizzi,[64a,64b] A. T. Serban,[64a,ff] P. Spagnolo,[64a] P. Squillacioti,[64a,c] R. Tenchini,[64a] G. Tonelli,[64a,64b] A. Venturi,[64a] P. G. Verdini,[64a] L. Barone,[65a,65b] F. Cavallari,[65a] D. Del Re,[65a,65b] M. Diemoz,[65a] C. Fanelli,[65a,65b] M. Grassi,[65a,65b,c] E. Longo,[65a,65b] P. Meridiani,[65a,c] F. Micheli,[65a,65b] S. Nourbakhsh,[65a,65b] G. Organtini,[65a,65b] R. Paramatti,[65a] S. Rahatlou,[65a,65b] M. Sigamani,[65a] L. Soffi,[65a,65b] N. Amapane,[66a,66b] R. Arcidiacono,[66a,66c] S. Argiro,[66a,66b] M. Arneodo,[66a,66c] C. Biino,[66a] N. Cartiglia,[66a] S. Casasso,[66a,66b] M. Costa,[66a,66b] N. Demaria,[66a] C. Mariotti,[66a,c] S. Maselli,[66a] E. Migliore,[66a,66b] V. Monaco,[66a,66b] M. Musich,[66a,c] M. M. Obertino,[66a,66c] N. Pastrone,[66a] M. Pelliccioni,[66a] A. Potenza,[66a,66b] A. Romero,[66a,66b] M. Ruspa,[66a,66c] R. Sacchi,[66a,66b] A. Solano,[66a,66b] A. Staiano,[66a] S. Belforte,[67a] V. Candelise,[67a,67b] M. Casarsa,[67a] F. Cossutti,[67a] G. Della Ricca,[67a,67b] B. Gobbo,[67a] M. Marone,[67a,67b,c] D. Montanino,[67a,67b,c] A. Penzo,[67a] A. Schizzi,[67a,67b] T. Y. Kim,[68] S. K. Nam,[68] S. Chang,[69] D. H. Kim,[69] G. N. Kim,[69] D. J. Kong,[69] H. Park,[69] D. C. Son,[69] T. Son,[69] J. Y. Kim,[70] Zero J. Kim,[70] S. Song,[70] S. Choi,[71] D. Gyun,[71] B. Hong,[71] M. Jo,[71] H. Kim,[71] T. J. Kim,[71] K. S. Lee,[71] D. H. Moon,[71] S. K. Park,[71] Y. Roh,[71] M. Choi,[72] J. H. Kim,[72] C. Park,[72] I. C. Park,[72] S. Park,[72] G. Ryu,[72] Y. Choi,[73] Y. K. Choi,[73] J. Goh,[73] M. S. Kim,[73] E. Kwon,[73] B. Lee,[73] J. Lee,[73] S. Lee,[73] H. Seo,[73] I. Yu,[73] M. J. Bilinskas,[74] I. Grigelionis,[74] M. Janulis,[74] A. Juodagalvis,[74]

H. Castilla-Valdez,[75] E. De La Cruz-Burelo,[75] I. Heredia-de La Cruz,[75] R. Lopez-Fernandez,[75] J. Martínez-Ortega,[75] A. Sanchez-Hernandez,[75] L. M. Villasenor-Cendejas,[75] S. Carrillo Moreno,[76] F. Vazquez Valencia,[76] H. A. Salazar Ibarguen,[77] E. Casimiro Linares,[78] A. Morelos Pineda,[78] M. A. Reyes-Santos,[78] D. Krofcheck,[79] A. J. Bell,[80] P. H. Butler,[80] R. Doesburg,[80] S. Reucroft,[80] H. Silverwood,[80] M. Ahmad,[81] M. I. Asghar,[81] J. Butt,[81] H. R. Hoorani,[81] S. Khalid,[81] W. A. Khan,[81] T. Khurshid,[81] S. Qazi,[81] M. A. Shah,[81] M. Shoaib,[81] H. Bialkowska,[82] B. Boimska,[82] T. Frueboes,[82] M. Górski,[82] M. Kazana,[82] K. Nawrocki,[82] K. Romanowska-Rybinska,[82] M. Szleper,[82] G. Wrochna,[82] P. Zalewski,[82] G. Brona,[83] K. Bunkowski,[83] M. Cwiok,[83] W. Dominik,[83] K. Doroba,[83] A. Kalinowski,[83] M. Konecki,[83] J. Krolikowski,[83] M. Misiura,[83] N. Almeida,[84] P. Bargassa,[84] A. David,[84] P. Faccioli,[84] P. G. Ferreira Parracho,[84] M. Gallinaro,[84] J. Seixas,[84] J. Varela,[84] P. Vischia,[84] P. Bunin,[85] I. Golutvin,[85] A. Kamenev,[85] V. Karjavin,[85] V. Konoplyanikov,[85] G. Kozlov,[85] A. Lanev,[85] A. Malakhov,[85] P. Moisenz,[85] V. Palichik,[85] V. Perelygin,[85] M. Savina,[85] S. Shmatov,[85] S. Shulha,[85] V. Smirnov,[85] A. Volodko,[85] A. Zarubin,[85] S. Evstyukhin,[86] V. Golovtsov,[86] Y. Ivanov,[86] V. Kim,[86] P. Levchenko,[86] V. Murzin,[86] V. Oreshkin,[86] I. Smirnov,[86] V. Sulimov,[86] L. Uvarov,[86] S. Vavilov,[86] A. Vorobyev,[86] An. Vorobyev,[86] Yu. Andreev,[87] A. Dermenev,[87] S. Gninenko,[87] N. Golubev,[87] M. Kirsanov,[87] N. Krasnikov,[87] V. Matveev,[87] A. Pashenkov,[87] D. Tlisov,[87] A. Toropin,[87] V. Epshteyn,[88] M. Erofeeva,[88] V. Gavrilov,[88] M. Kossov,[88] N. Lychkovskaya,[88] V. Popov,[88] G. Safronov,[88] S. Semenov,[88] I. Shreyber,[88] V. Stolin,[88] E. Vlasov,[88] A. Zhokin,[88] V. Andreev,[89] M. Azarkin,[89] I. Dremin,[89] M. Kirakosyan,[89] A. Leonidov,[89] G. Mesyats,[89] S. V. Rusakov,[89] A. Vinogradov,[89] A. Belyaev,[90] E. Boos,[90] V. Bunichev,[90] M. Dubinin,[90,e] L. Dudko,[90] A. Ershov,[90] A. Gribushin,[90] V. Klyukhin,[90] O. Kodolova,[90] I. Lokhtin,[90] A. Markina,[90] S. Obraztsov,[90] M. Perfilov,[90] S. Petrushanko,[90] A. Popov,[90] L. Sarycheva,[90,a] V. Savrin,[90] I. Azhgirey,[91] I. Bayshev,[91] S. Bitioukov,[91] V. Grishin,[91,c] V. Kachanov,[91] D. Konstantinov,[91] V. Krychkine,[91] V. Petrov,[91] R. Ryutin,[91] A. Sobol,[91] L. Tourtchanovitch,[91] S. Troshin,[91] N. Tyurin,[91] A. Uzunian,[91] A. Volkov,[91] P. Adzic,[92,gg] M. Djordjevic,[92] M. Ekmedzic,[92] D. Krpic,[92,gg] J. Milosevic,[92] M. Aguilar-Benitez,[93] J. Alcaraz Maestre,[93] P. Arce,[93] C. Battilana,[93] E. Calvo,[93] M. Cerrada,[93] M. Chamizo Llatas,[93] N. Colino,[93] B. De La Cruz,[93] A. Delgado Peris,[93] D. Domínguez Vázquez,[93] C. Fernandez Bedoya,[93] J. P. Fernández Ramos,[93] A. Ferrando,[93] J. Flix,[93] M. C. Fouz,[93] P. Garcia-Abia,[93] O. Gonzalez Lopez,[93] S. Goy Lopez,[93] J. M. Hernandez,[93] M. I. Josa,[93] G. Merino,[93] J. Puerta Pelayo,[93] A. Quintario Olmeda,[93] I. Redondo,[93] L. Romero,[93] J. Santaolalla,[93] M. S. Soares,[93] C. Willmott,[93] C. Albajar,[94] G. Codispoti,[94] J. F. de Trocóniz,[94] H. Brun,[95] J. Cuevas,[95] J. Fernandez Menendez,[95] S. Folgueras,[95] I. Gonzalez Caballero,[95] L. Lloret Iglesias,[95] J. Piedra Gomez,[95] J. A. Brochero Cifuentes,[96] I. J. Cabrillo,[96] A. Calderon,[96] S. H. Chuang,[96] J. Duarte Campderros,[96] M. Felcini,[96,hh] M. Fernandez,[96] G. Gomez,[96] J. Gonzalez Sanchez,[96] A. Graziano,[96] C. Jorda,[96] A. Lopez Virto,[96] J. Marco,[96] R. Marco,[96] C. Martinez Rivero,[96] F. Matorras,[96] F. J. Munoz Sanchez,[96] T. Rodrigo,[96] A. Y. Rodríguez-Marrero,[96] A. Ruiz-Jimeno,[96] L. Scodellaro,[96] I. Vila,[96] R. Vilar Cortabitarte,[96] D. Abbaneo,[97] E. Auffray,[97] G. Auzinger,[97] M. Bachtis,[97] P. Baillon,[97] A. H. Ball,[97] D. Barney,[97] J. F. Benitez,[97] C. Bernet,[97,f] G. Bianchi,[97] P. Bloch,[97] A. Bocci,[97] A. Bonato,[97] C. Botta,[97] H. Breuker,[97] T. Camporesi,[97] G. Cerminara,[97] T. Christiansen,[97] J. A. Coarasa Perez,[97] D. D'Enterria,[97] A. Dabrowski,[97] A. De Roeck,[97] S. Di Guida,[97] M. Dobson,[97] N. Dupont-Sagorin,[97] A. Elliott-Peisert,[97] B. Frisch,[97] W. Funk,[97] G. Georgiou,[97] M. Giffels,[97] D. Gigi,[97] K. Gill,[97] D. Giordano,[97] M. Girone,[97] M. Giunta,[97] F. Glege,[97] R. Gomez-Reino Garrido,[97] P. Govoni,[97] S. Gowdy,[97] R. Guida,[97] S. Gundacker,[97] J. Hammer,[97] M. Hansen,[97] P. Harris,[97] C. Hartl,[97] J. Harvey,[97] B. Hegner,[97] A. Hinzmann,[97] V. Innocente,[97] P. Janot,[97] K. Kaadze,[97] E. Karavakis,[97] K. Kousouris,[97] P. Lecoq,[97] Y.-J. Lee,[97] P. Lenzi,[97] C. Lourenço,[97] N. Magini,[97] T. Mäki,[97] M. Malberti,[97] L. Malgeri,[97] M. Mannelli,[97] L. Masetti,[97] F. Meijers,[97] S. Mersi,[97] E. Meschi,[97] R. Moser,[97] M. U. Mozer,[97] M. Mulders,[97] P. Musella,[97] E. Nesvold,[97] L. Orsini,[97] E. Palencia Cortezon,[97] E. Perez,[97] L. Perrozzi,[97] A. Petrilli,[97] A. Pfeiffer,[97] M. Pierini,[97] M. Pimiä,[97] D. Piparo,[97] G. Polese,[97] L. Quertenmont,[97] A. Racz,[97] W. Reece,[97] J. Rodrigues Antunes,[97] G. Rolandi,[97,ii] C. Rovelli,[97,jj] M. Rovere,[97] H. Sakulin,[97] F. Santanastasio,[97] C. Schäfer,[97] C. Schwick,[97] I. Segoni,[97] S. Sekmen,[97] A. Sharma,[97] P. Siegrist,[97] P. Silva,[97] M. Simon,[97] P. Sphicas,[97,kk] D. Spiga,[97] A. Tsirou,[97] G. I. Veres,[97,u] J. R. Vlimant,[97] H. K. Wöhri,[97] S. D. Worm,[97,ll] W. D. Zeuner,[97] W. Bertl,[98] K. Deiters,[98] W. Erdmann,[98] K. Gabathuler,[98] R. Horisberger,[98] Q. Ingram,[98] H. C. Kaestli,[98] S. König,[98] D. Kotlinski,[98] U. Langenegger,[98] F. Meier,[98] D. Renker,[98] T. Rohe,[98] L. Bäni,[99] P. Bortignon,[99] M. A. Buchmann,[99] B. Casal,[99] N. Chanon,[99] A. Deisher,[99] G. Dissertori,[99] M. Dittmar,[99] M. Donegà,[99] M. Dünser,[99] P. Eller,[99] J. Eugster,[99] K. Freudenreich,[99] C. Grab,[99] D. Hits,[99] P. Lecomte,[99] W. Lustermann,[99] A. C. Marini,[99] P. Martinez Ruiz del Arbol,[99] N. Mohr,[99] F. Moortgat,[99] C. Nägeli,[99,mm] P. Nef,[99] F. Nessi-Tedaldi,[99] F. Pandolfi,[99] L. Pape,[99] F. Pauss,[99] M. Peruzzi,[99]

F. J. Ronga,[99] M. Rossini,[99] L. Sala,[99] A. K. Sanchez,[99] A. Starodumov,[99,nn] B. Stieger,[99] M. Takahashi,[99] L. Tauscher,[99,a] A. Thea,[99] K. Theofilatos,[99] D. Treille,[99] C. Urscheler,[99] R. Wallny,[99] H. A. Weber,[99] L. Wehrli,[99] C. Amsler,[100,oo] V. Chiochia,[100] S. De Visscher,[100] C. Favaro,[100] M. Ivova Rikova,[100] B. Kilminster,[100] B. Millan Mejias,[100] P. Otiougova,[100] P. Robmann,[100] H. Snoek,[100] S. Tupputi,[100] M. Verzetti,[100] Y. H. Chang,[101] K. H. Chen,[101] C. Ferro,[101] C. M. Kuo,[101] S. W. Li,[101] W. Lin,[101] Y. J. Lu,[101] A. P. Singh,[101] R. Volpe,[101] S. S. Yu,[101] P. Bartalini,[102] P. Chang,[102] Y. H. Chang,[102] Y. W. Chang,[102] Y. Chao,[102] K. F. Chen,[102] C. Dietz,[102] U. Grundler,[102] W.-S. Hou,[102] Y. Hsiung,[102] K. Y. Kao,[102] Y. J. Lei,[102] R.-S. Lu,[102] D. Majumder,[102] E. Petrakou,[102] X. Shi,[102] J. G. Shiu,[102] Y. M. Tzeng,[102] X. Wan,[102] M. Wang,[102] B. Asavapibhop,[103] N. Srimanobhas,[103] A. Adiguzel,[104] M. N. Bakirci,[104,pp] S. Cerci,[104,qq] C. Dozen,[104] I. Dumanoglu,[104] E. Eskut,[104] S. Girgis,[104] G. Gokbulut,[104] E. Gurpinar,[104] I. Hos,[104] E. E. Kangal,[104] T. Karaman,[104] G. Karapinar,[104,rr] A. Kayis Topaksu,[104] G. Onengut,[104] K. Ozdemir,[104] S. Ozturk,[104,ss] A. Polatoz,[104] K. Sogut,[104,tt] D. Sunar Cerci,[104,qq] B. Tali,[104,qq] H. Topakli,[104,pp] L. N. Vergili,[104] M. Vergili,[104] I. V. Akin,[105] T. Aliev,[105] B. Bilin,[105] S. Bilmis,[105] M. Deniz,[105] H. Gamsizkan,[105] A. M. Guler,[105] K. Ocalan,[105] A. Ozpineci,[105] M. Serin,[105] R. Sever,[105] U. E. Surat,[105] M. Yalvac,[105] E. Yildirim,[105] M. Zeyrek,[105] E. Gülmez,[106] B. Isildak,[106,uu] M. Kaya,[106,vv] O. Kaya,[106,vv] S. Ozkorucuklu,[106,ww] N. Sonmez,[106,xx] K. Cankocak,[107] L. Levchuk,[108] J. J. Brooke,[109] E. Clement,[109] D. Cussans,[109] H. Flacher,[109] R. Frazier,[109] J. Goldstein,[109] M. Grimes,[109] G. P. Heath,[109] H. F. Heath,[109] L. Kreczko,[109] S. Metson,[109] D. M. Newbold,[109,ll] K. Nirunpong,[109] A. Poll,[109] S. Senkin,[109] V. J. Smith,[109] T. Williams,[109] L. Basso,[110,yy] K. W. Bell,[110] A. Belyaev,[110,yy] C. Brew,[110] R. M. Brown,[110] D. J. A. Cockerill,[110] J. A. Coughlan,[110] K. Harder,[110] S. Harper,[110] J. Jackson,[110] B. W. Kennedy,[110] E. Olaiya,[110] D. Petyt,[110] B. C. Radburn-Smith,[110] C. H. Shepherd-Themistocleous,[110] I. R. Tomalin,[110] W. J. Womersley,[110] R. Bainbridge,[111] G. Ball,[111] R. Beuselinck,[111] O. Buchmuller,[111] D. Colling,[111] N. Cripps,[111] M. Cutajar,[111] P. Dauncey,[111] G. Davies,[111] M. Della Negra,[111] W. Ferguson,[111] J. Fulcher,[111] D. Futyan,[111] A. Gilbert,[111] A. Guneratne Bryer,[111] G. Hall,[111] Z. Hatherell,[111] J. Hays,[111] G. Iles,[111] M. Jarvis,[111] G. Karapostoli,[111] L. Lyons,[111] A.-M. Magnan,[111] J. Marrouche,[111] B. Mathias,[111] R. Nandi,[111] J. Nash,[111] A. Nikitenko,[111,nn] J. Pela,[111] M. Pesaresi,[111] K. Petridis,[111] M. Pioppi,[111,zz] D. M. Raymond,[111] S. Rogerson,[111] A. Rose,[111] M. J. Ryan,[111] C. Seez,[111] P. Sharp,[111,a] A. Sparrow,[111] M. Stoye,[111] A. Tapper,[111] M. Vazquez Acosta,[111] T. Virdee,[111] S. Wakefield,[111] N. Wardle,[111] T. Whyntie,[111] M. Chadwick,[112] J. E. Cole,[112] P. R. Hobson,[112] A. Khan,[112] P. Kyberd,[112] D. Leggat,[112] D. Leslie,[112] W. Martin,[112] I. D. Reid,[112] P. Symonds,[112] L. Teodorescu,[112] M. Turner,[112] K. Hatakeyama,[113] H. Liu,[113] T. Scarborough,[113] O. Charaf,[114] C. Henderson,[114] P. Rumerio,[114] A. Avetisyan,[115] T. Bose,[115] C. Fantasia,[115] A. Heister,[115] P. Lawson,[115] D. Lazic,[115] J. Rohlf,[115] D. Sperka,[115] J. St. John,[115] L. Sulak,[115] J. Alimena,[116] S. Bhattacharya,[116] G. Christopher,[116] D. Cutts,[116] Z. Demiragli,[116] A. Ferapontov,[116] A. Garabedian,[116] U. Heintz,[116] S. Jabeen,[116] G. Kukartsev,[116] E. Laird,[116] G. Landsberg,[116] M. Luk,[116] M. Narain,[116] D. Nguyen,[116] M. Segala,[116] T. Sinthuprasith,[116] T. Speer,[116] R. Breedon,[117] G. Breto,[117] M. Calderon De La Barca Sanchez,[117] S. Chauhan,[117] M. Chertok,[117] J. Conway,[117] R. Conway,[117] P. T. Cox,[117] J. Dolen,[117] R. Erbacher,[117] M. Gardner,[117] R. Houtz,[117] W. Ko,[117] A. Kopecky,[117] R. Lander,[117] O. Mall,[117] T. Miceli,[117] D. Pellett,[117] F. Ricci-Tam,[117] B. Rutherford,[117] M. Searle,[117] J. Smith,[117] M. Squires,[117] M. Tripathi,[117] R. Vasquez Sierra,[117] R. Yohay,[117] V. Andreev,[118] D. Cline,[118] R. Cousins,[118] J. Duris,[118] S. Erhan,[118] P. Everaerts,[118] C. Farrell,[118] J. Hauser,[118] M. Ignatenko,[118] C. Jarvis,[118] G. Rakness,[118] P. Schlein,[118,a] P. Traczyk,[118] V. Valuev,[118] M. Weber,[118] J. Babb,[119] R. Clare,[119] M. E. Dinardo,[119] J. Ellison,[119] J. W. Gary,[119] F. Giordano,[119] G. Hanson,[119] H. Liu,[119] O. R. Long,[119] A. Luthra,[119] H. Nguyen,[119] S. Paramesvaran,[119] J. Sturdy,[119] S. Sumowidagdo,[119] R. Wilken,[119] S. Wimpenny,[119] W. Andrews,[120] J. G. Branson,[120] G. B. Cerati,[120] S. Cittolin,[120] D. Evans,[120] A. Holzner,[120] R. Kelley,[120] M. Lebourgeois,[120] J. Letts,[120] I. Macneill,[120] B. Mangano,[120] S. Padhi,[120] C. Palmer,[120] G. Petrucciani,[120] M. Pieri,[120] M. Sani,[120] V. Sharma,[120] S. Simon,[120] E. Sudano,[120] M. Tadel,[120] Y. Tu,[120] A. Vartak,[120] S. Wasserbaech,[120,aaa] F. Würthwein,[120] A. Yagil,[120] J. Yoo,[120] D. Barge,[121] R. Bellan,[121] C. Campagnari,[121] M. D'Alfonso,[121] T. Danielson,[121] K. Flowers,[121] P. Geffert,[121] F. Golf,[121] J. Incandela,[121] C. Justus,[121] P. Kalavase,[121] D. Kovalskyi,[121] V. Krutelyov,[121] S. Lowette,[121] R. Magaña Villalba,[121] N. Mccoll,[121] V. Pavlunin,[121] J. Ribnik,[121] J. Richman,[121] R. Rossin,[121] D. Stuart,[121] W. To,[121] C. West,[121] A. Apresyan,[122] A. Bornheim,[122] Y. Chen,[122] E. Di Marco,[122] J. Duarte,[122] M. Gataullin,[122] Y. Ma,[122] A. Mott,[122] H. B. Newman,[122] C. Rogan,[122] M. Spiropulu,[122] V. Timciuc,[122] J. Veverka,[122] R. Wilkinson,[122] S. Xie,[122] Y. Yang,[122] R. Y. Zhu,[122] V. Azzolini,[123] A. Calamba,[123] R. Carroll,[123] T. Ferguson,[123] Y. Iiyama,[123] D. W. Jang,[123] Y. F. Liu,[123] M. Paulini,[123] H. Vogel,[123] I. Vorobiev,[123] J. P. Cumalat,[124] B. R. Drell,[124] W. T. Ford,[124] A. Gaz,[124] E. Luiggi Lopez,[124] J. G. Smith,[124]

K. Stenson,[124] K. A. Ulmer,[124] S. R. Wagner,[124] J. Alexander,[125] A. Chatterjee,[125] N. Eggert,[125] L. K. Gibbons,[125] B. Heltsley,[125] W. Hopkins,[125] A. Khukhunaishvili,[125] B. Kreis,[125] N. Mirman,[125] G. Nicolas Kaufman,[125] J. R. Patterson,[125] A. Ryd,[125] E. Salvati,[125] W. Sun,[125] W. D. Teo,[125] J. Thom,[125] J. Thompson,[125] J. Tucker,[125] J. Vaughan,[125] Y. Weng,[125] L. Winstrom,[125] P. Wittich,[125] D. Winn,[126] S. Abdullin,[127] M. Albrow,[127] J. Anderson,[127] L. A. T. Bauerdick,[127] A. Beretvas,[127] J. Berryhill,[127] P. C. Bhat,[127] K. Burkett,[127] J. N. Butler,[127] V. Chetluru,[127] H. W. K. Cheung,[127] F. Chlebana,[127] V. D. Elvira,[127] I. Fisk,[127] J. Freeman,[127] Y. Gao,[127] D. Green,[127] O. Gutsche,[127] J. Hanlon,[127] R. M. Harris,[127] J. Hirschauer,[127] B. Hooberman,[127] S. Jindariani,[127] M. Johnson,[127] U. Joshi,[127] B. Klima,[127] S. Kunori,[127] S. Kwan,[127] C. Leonidopoulos,[127,bbb] J. Linacre,[127] D. Lincoln,[127] R. Lipton,[127] J. Lykken,[127] K. Maeshima,[127] J. M. Marraffino,[127] S. Maruyama,[127] D. Mason,[127] P. McBride,[127] K. Mishra,[127] S. Mrenna,[127] Y. Musienko,[127,ccc] C. Newman-Holmes,[127] V. O'Dell,[127] O. Prokofyev,[127] E. Sexton-Kennedy,[127] S. Sharma,[127] W. J. Spalding,[127] L. Spiegel,[127] L. Taylor,[127] S. Tkaczyk,[127] N. V. Tran,[127] L. Uplegger,[127] E. W. Vaandering,[127] R. Vidal,[127] J. Whitmore,[127] W. Wu,[127] F. Yang,[127] J. C. Yun,[127] D. Acosta,[128] P. Avery,[128] D. Bourilkov,[128] M. Chen,[128] T. Cheng,[128] S. Das,[128] M. De Gruttola,[128] G. P. Di Giovanni,[128] D. Dobur,[128] A. Drozdetskiy,[128] R. D. Field,[128] M. Fisher,[128] Y. Fu,[128] I. K. Furic,[128] J. Gartner,[128] J. Hugon,[128] B. Kim,[128] J. Konigsberg,[128] A. Korytov,[128] A. Kropivnitskaya,[128] T. Kypreos,[128] J. F. Low,[128] K. Matchev,[128] P. Milenovic,[128,ddd] G. Mitselmakher,[128] L. Muniz,[128] M. Park,[128] R. Remington,[128] A. Rinkevicius,[128] P. Sellers,[128] N. Skhirtladze,[128] M. Snowball,[128] J. Yelton,[128] M. Zakaria,[128] V. Gaultney,[129] S. Hewamanage,[129] L. M. Lebolo,[129] S. Linn,[129] P. Markowitz,[129] G. Martinez,[129] J. L. Rodriguez,[129] T. Adams,[130] A. Askew,[130] J. Bochenek,[130] J. Chen,[130] B. Diamond,[130] S. V. Gleyzer,[130] J. Haas,[130] S. Hagopian,[130] V. Hagopian,[130] M. Jenkins,[130] K. F. Johnson,[130] H. Prosper,[130] V. Veeraraghavan,[130] M. Weinberg,[130] M. M. Baarmand,[131] B. Dorney,[131] M. Hohlmann,[131] H. Kalakhety,[131] I. Vodopiyanov,[131] F. Yumiceva,[131] M. R. Adams,[132] I. M. Anghel,[132] L. Apanasevich,[132] Y. Bai,[132] V. E. Bazterra,[132] R. R. Betts,[132] I. Bucinskaite,[132] J. Callner,[132] R. Cavanaugh,[132] O. Evdokimov,[132] L. Gauthier,[132] C. E. Gerber,[132] D. J. Hofman,[132] S. Khalatyan,[132] F. Lacroix,[132] C. O'Brien,[132] C. Silkworth,[132] D. Strom,[132] P. Turner,[132] N. Varelas,[132] U. Akgun,[133] E. A. Albayrak,[133] B. Bilki,[133,eee] W. Clarida,[133] F. Duru,[133] S. Griffiths,[133] J.-P. Merlo,[133] H. Mermerkaya,[133,fff] A. Mestvirishvili,[133] A. Moeller,[133] J. Nachtman,[133] C. R. Newsom,[133] E. Norbeck,[133] Y. Onel,[133] F. Ozok,[133,ggg] S. Sen,[133] P. Tan,[133] E. Tiras,[133] J. Wetzel,[133] T. Yetkin,[133] K. Yi,[133] B. A. Barnett,[134] B. Blumenfeld,[134] S. Bolognesi,[134] D. Fehling,[134] G. Giurgiu,[134] A. V. Gritsan,[134] Z. J. Guo,[134] G. Hu,[134] P. Maksimovic,[134] M. Swartz,[134] A. Whitbeck,[134] P. Baringer,[135] A. Bean,[135] G. Benelli,[135] R. P. Kenny Iii,[135] M. Murray,[135] D. Noonan,[135] S. Sanders,[135] R. Stringer,[135] G. Tinti,[135] J. S. Wood,[135] A. F. Barfuss,[136] T. Bolton,[136] I. Chakaberia,[136] A. Ivanov,[136] S. Khalil,[136] M. Makouski,[136] Y. Maravin,[136] S. Shrestha,[136] I. Svintradze,[136] J. Gronberg,[137] D. Lange,[137] F. Rebassoo,[137] D. Wright,[137] A. Baden,[138] B. Calvert,[138] S. C. Eno,[138] J. A. Gomez,[138] N. J. Hadley,[138] R. G. Kellogg,[138] M. Kirn,[138] T. Kolberg,[138] Y. Lu,[138] M. Marionneau,[138] A. C. Mignerey,[138] K. Pedro,[138] A. Skuja,[138] J. Temple,[138] M. B. Tonjes,[138] S. C. Tonwar,[138] A. Apyan,[139] G. Bauer,[139] J. Bendavid,[139] W. Busza,[139] E. Butz,[139] I. A. Cali,[139] M. Chan,[139] V. Dutta,[139] G. Gomez Ceballos,[139] M. Goncharov,[139] Y. Kim,[139] M. Klute,[139] K. Krajczar,[139,hhh] A. Levin,[139] P. D. Luckey,[139] T. Ma,[139] S. Nahn,[139] C. Paus,[139] D. Ralph,[139] C. Roland,[139] G. Roland,[139] M. Rudolph,[139] G. S. F. Stephans,[139] F. Stöckli,[139] K. Sumorok,[139] K. Sung,[139] D. Velicanu,[139] E. A. Wenger,[139] R. Wolf,[139] B. Wyslouch,[139] M. Yang,[139] Y. Yilmaz,[139] A. S. Yoon,[139] M. Zanetti,[139] V. Zhukova,[139] S. I. Cooper,[140] B. Dahmes,[140] A. De Benedetti,[140] G. Franzoni,[140] A. Gude,[140] S. C. Kao,[140] K. Klapoetke,[140] Y. Kubota,[140] J. Mans,[140] N. Pastika,[140] R. Rusack,[140] M. Sasseville,[140] A. Singovsky,[140] N. Tambe,[140] J. Turkewitz,[140] L. M. Cremaldi,[141] R. Kroeger,[141] L. Perera,[141] R. Rahmat,[141] D. A. Sanders,[141] E. Avdeeva,[142] K. Bloom,[142] S. Bose,[142] D. R. Claes,[142] A. Dominguez,[142] M. Eads,[142] J. Keller,[142] I. Kravchenko,[142] J. Lazo-Flores,[142] S. Malik,[142] G. R. Snow,[142] A. Godshalk,[143] I. Iashvili,[143] S. Jain,[143] A. Kharchilava,[143] A. Kumar,[143] S. Rappoccio,[143] G. Alverson,[144] E. Barberis,[144] D. Baumgartel,[144] M. Chasco,[144] J. Haley,[144] D. Nash,[144] T. Orimoto,[144] D. Trocino,[144] D. Wood,[144] J. Zhang,[144] A. Anastassov,[145] K. A. Hahn,[145] A. Kubik,[145] L. Lusito,[145] N. Mucia,[145] N. Odell,[145] R. A. Ofierzynski,[145] B. Pollack,[145] A. Pozdnyakov,[145] M. Schmitt,[145] S. Stoynev,[145] M. Velasco,[145] S. Won,[145] L. Antonelli,[146] D. Berry,[146] A. Brinkerhoff,[146] K. M. Chan,[146] M. Hildreth,[146] C. Jessop,[146] D. J. Karmgard,[146] J. Kolb,[146] K. Lannon,[146] W. Luo,[146] S. Lynch,[146] N. Marinelli,[146] D. M. Morse,[146] T. Pearson,[146] M. Planer,[146] R. Ruchti,[146] J. Slaunwhite,[146] N. Valls,[146] M. Wayne,[146] M. Wolf,[146] B. Bylsma,[147] L. S. Durkin,[147] C. Hill,[147] R. Hughes,[147] K. Kotov,[147] T. Y. Ling,[147] D. Puigh,[147] M. Rodenburg,[147] C. Vuosalo,[147] G. Williams,[147] B. L. Winer,[147] E. Berry,[148] P. Elmer,[148] V. Halyo,[148] P. Hebda,[148] J. Hegeman,[148] A. Hunt,[148]

P. Jindal,[148] S. A. Koay,[148] D. Lopes Pegna,[148] P. Lujan,[148] D. Marlow,[148] T. Medvedeva,[148] M. Mooney,[148] J. Olsen,[148] P. Piroué,[148] X. Quan,[148] A. Raval,[148] H. Saka,[148] D. Stickland,[148] C. Tully,[148] J. S. Werner,[148] A. Zuranski,[148] E. Brownson,[149] A. Lopez,[149] H. Mendez,[149] J. E. Ramirez Vargas,[149] E. Alagoz,[150] V. E. Barnes,[150] D. Benedetti,[150] G. Bolla,[150] D. Bortoletto,[150] M. De Mattia,[150] A. Everett,[150] Z. Hu,[150] M. Jones,[150] O. Koybasi,[150] M. Kress,[150] A. T. Laasanen,[150] N. Leonardo,[150] V. Maroussov,[150] P. Merkel,[150] D. H. Miller,[150] N. Neumeister,[150] I. Shipsey,[150] D. Silvers,[150] A. Svyatkovskiy,[150] M. Vidal Marono,[150] H. D. Yoo,[150] J. Zablocki,[150] Y. Zheng,[150] S. Guragain,[151] N. Parashar,[151] A. Adair,[152] B. Akgun,[152] C. Boulahouache,[152] K. M. Ecklund,[152] F. J. M. Geurts,[152] W. Li,[152] B. P. Padley,[152] R. Redjimi,[152] J. Roberts,[152] J. Zabel,[152] B. Betchart,[153] A. Bodek,[153] Y. S. Chung,[153] R. Covarelli,[153] P. de Barbaro,[153] R. Demina,[153] Y. Eshaq,[153] T. Ferbel,[153] A. Garcia-Bellido,[153] P. Goldenzweig,[153] J. Han,[153] A. Harel,[153] D. C. Miner,[153] D. Vishnevskiy,[153] M. Zielinski,[153] A. Bhatti,[154] R. Ciesielski,[154] L. Demortier,[154] K. Goulianos,[154] G. Lungu,[154] S. Malik,[154] C. Mesropian,[154] S. Arora,[155] A. Barker,[155] J. P. Chou,[155] C. Contreras-Campana,[155] E. Contreras-Campana,[155] D. Duggan,[155] D. Ferencek,[155] Y. Gershtein,[155] R. Gray,[155] E. Halkiadakis,[155] D. Hidas,[155] A. Lath,[155] S. Panwalkar,[155] M. Park,[155] R. Patel,[155] V. Rekovic,[155] J. Robles,[155] K. Rose,[155] S. Salur,[155] S. Schnetzer,[155] C. Seitz,[155] S. Somalwar,[155] R. Stone,[155] S. Thomas,[155] M. Walker,[155] G. Cerizza,[156] M. Hollingsworth,[156] S. Spanier,[156] Z. C. Yang,[156] A. York,[156] R. Eusebi,[157] W. Flanagan,[157] J. Gilmore,[157] T. Kamon,[157,iii] V. Khotilovich,[157] R. Montalvo,[157] I. Osipenkov,[157] Y. Pakhotin,[157] A. Perloff,[157] J. Roe,[157] A. Safonov,[157] T. Sakuma,[157] S. Sengupta,[157] I. Suarez,[157] A. Tatarinov,[157] D. Toback,[157] N. Akchurin,[158] J. Damgov,[158] C. Dragoiu,[158] P. R. Dudero,[158] C. Jeong,[158] K. Kovitanggoon,[158] S. W. Lee,[158] T. Libeiro,[158] I. Volobouev,[158] E. Appelt,[159] A. G. Delannoy,[159] C. Florez,[159] S. Greene,[159] A. Gurrola,[159] W. Johns,[159] P. Kurt,[159] C. Maguire,[159] A. Melo,[159] M. Sharma,[159] P. Sheldon,[159] B. Snook,[159] S. Tuo,[159] J. Velkovska,[159] M. W. Arenton,[160] M. Balazs,[160] S. Boutle,[160] B. Cox,[160] B. Francis,[160] J. Goodell,[160] R. Hirosky,[160] A. Ledovskoy,[160] C. Lin,[160] C. Neu,[160] J. Wood,[160] S. Gollapinni,[161] R. Harr,[161] P. E. Karchin,[161] C. Kottachchi Kankanamge Don,[161] P. Lamichhane,[161] A. Sakharov,[161] M. Anderson,[162] D. A. Belknap,[162] L. Borrello,[162] D. Carlsmith,[162] M. Cepeda,[162] S. Dasu,[162] E. Friis,[162] L. Gray,[162] K. S. Grogg,[162] M. Grothe,[162] R. Hall-Wilton,[162] M. Herndon,[162] A. Hervé,[162] P. Klabbers,[162] J. Klukas,[162] A. Lanaro,[162] C. Lazaridis,[162] R. Loveless,[162] A. Mohapatra,[162] I. Ojalvo,[162] F. Palmonari,[162] G. A. Pierro,[162] I. Ross,[162] A. Savin,[162] W. H. Smith,[162] and J. Swanson[162]

(CMS Collaboration)

[1]*Yerevan Physics Institute, Yerevan, Armenia*
[2]*Institut für Hochenergiephysik der OeAW, Wien, Austria*
[3]*National Centre for Particle and High Energy Physics, Minsk, Belarus*
[4]*Universiteit Antwerpen, Antwerpen, Belgium*
[5]*Vrije Universiteit Brussel, Brussel, Belgium*
[6]*Université Libre de Bruxelles, Bruxelles, Belgium*
[7]*Ghent University, Ghent, Belgium*
[8]*Université Catholique de Louvain, Louvain-la-Neuve, Belgium*
[9]*Université de Mons, Mons, Belgium*
[10]*Centro Brasileiro de Pesquisas Fisicas, Rio de Janeiro, Brazil*
[11]*Universidade do Estado do Rio de Janeiro, Rio de Janeiro, Brazil*
[12a]*Universidade Estadual Paulista, São Paulo, Brazil*
[12b]*Universidade Federal do ABC, São Paulo, Brazil*
[13]*Institute for Nuclear Research and Nuclear Energy, Sofia, Bulgaria*
[14]*University of Sofia, Sofia, Bulgaria*
[15]*Institute of High Energy Physics, Beijing, China*
[16]*State Key Laboratory of Nuclear Physics and Technology, Peking University, Beijing, China*
[17]*Universidad de Los Andes, Bogota, Colombia*
[18]*Technical University of Split, Split, Croatia*
[19]*University of Split, Split, Croatia*
[20]*Institute Rudjer Boskovic, Zagreb, Croatia*
[21]*University of Cyprus, Nicosia, Cyprus*
[22]*Charles University, Prague, Czech Republic*
[23]*Academy of Scientific Research and Technology of the Arab Republic of Egypt, Egyptian Network of High Energy Physics, Cairo, Egypt*

[24]*National Institute of Chemical Physics and Biophysics, Tallinn, Estonia*
[25]*Department of Physics, University of Helsinki, Helsinki, Finland*
[26]*Helsinki Institute of Physics, Helsinki, Finland*
[27]*Lappeenranta University of Technology, Lappeenranta, Finland*
[28]*DSM/IRFU, CEA/Saclay, Gif-sur-Yvette, France*
[29]*Laboratoire Leprince-Ringuet, Ecole Polytechnique, IN2P3-CNRS, Palaiseau, France*
[30]*Institut Pluridisciplinaire Hubert Curien, Université de Strasbourg, Université de Haute Alsace Mulhouse, CNRS/IN2P3, Strasbourg, France*
[31]*Centre de Calcul de l'Institut National de Physique Nucleaire et de Physique des Particules, CNRS/IN2P3, Villeurbanne, France*
[32]*Université de Lyon, Université Claude Bernard Lyon 1, CNRS-IN2P3, Institut de Physique Nucléaire de Lyon, Villeurbanne, France*
[33]*Institute of High Energy Physics and Informatization, Tbilisi State University, Tbilisi, Georgia*
[34]*RWTH Aachen University, I. Physikalisches Institut, Aachen, Germany*
[35]*RWTH Aachen University, III. Physikalisches Institut A, Aachen, Germany*
[36]*RWTH Aachen University, III. Physikalisches Institut B, Aachen, Germany*
[37]*Deutsches Elektronen-Synchrotron, Hamburg, Germany*
[38]*University of Hamburg, Hamburg, Germany*
[39]*Institut für Experimentelle Kernphysik, Karlsruhe, Germany*
[40]*Institute of Nuclear Physics "Demokritos," Aghia Paraskevi, Greece*
[41]*University of Athens, Athens, Greece*
[42]*University of Ioánnina, Ioánnina, Greece*
[43]*KFKI Research Institute for Particle and Nuclear Physics, Budapest, Hungary*
[44]*Institute of Nuclear Research ATOMKI, Debrecen, Hungary*
[45]*University of Debrecen, Debrecen, Hungary*
[46]*Panjab University, Chandigarh, India*
[47]*University of Delhi, Delhi, India*
[48]*Saha Institute of Nuclear Physics, Kolkata, India*
[49]*Bhabha Atomic Research Centre, Mumbai, India*
[50]*Tata Institute of Fundamental Research-EHEP, Mumbai, India*
[51]*Tata Institute of Fundamental Research-HECR, Mumbai, India*
[52]*Institute for Research in Fundamental Sciences (IPM), Tehran, Iran*
[53a]*INFN Sezione di Bari, Bari, Italy*
[53b]*Università di Bari, Bari, Italy*
[53c]*Politecnico di Bari, Bari, Italy*
[54a]*INFN Sezione di Bologna, Bologna, Italy*
[54b]*Università di Bologna, Bologna, Italy*
[55a]*INFN Sezione di Catania, Catania, Italy*
[55b]*Università di Catania, Catania, Italy*
[56a]*INFN Sezione di Firenze, Firenze, Italy*
[56b]*Università di Firenze, Firenze, Italy*
[57]*INFN Laboratori Nazionali di Frascati, Frascati, Italy*
[58a]*INFN Sezione di Genova, Genova, Italy*
[58b]*Università di Genova, Genova, Italy*
[59a]*INFN Sezione di Milano-Bicocca, Milano, Italy*
[59b]*Università di Milano-Bicocca, Milano, Italy*
[60a]*INFN Sezione di Napoli, Napoli, Italy*
[60b]*Università di Napoli "Federico II," Napoli, Italy*
[60c]*Università della Basilicata (Potenza), Napoli, Italy*
[60d]*Università G. Marconi (Roma), Napoli, Italy*
[61a]*INFN Sezione di Padova, Padova, Italy*
[61b]*Università di Padova, Padova, Italy*
[61c]*Università di Trento (Trento), Padova, Italy*
[62a]*INFN Sezione di Pavia, Pavia, Italy*
[62b]*Università di Pavia, Pavia, Italy*
[63a]*INFN Sezione di Perugia, Perugia, Italy*
[63b]*Università di Perugia, Perugia, Italy*
[64a]*INFN Sezione di Pisa, Pisa, Italy*
[64b]*Università di Pisa, Pisa, Italy*
[64c]*Scuola Normale Superiore di Pisa, Pisa, Italy*
[65a]*INFN Sezione di Roma, Roma, Italy*
[65b]*Università di Roma, Roma, Italy*
[66a]*INFN Sezione di Torino, Torino, Italy*

[66b]Università di Torino, Torino, Italy
[66c]Università del Piemonte Orientale (Novara), Torino, Italy
[67a]INFN Sezione di Trieste, Trieste, Italy
[67b]Università di Trieste, Trieste, Italy
[68]Kangwon National University, Chunchon, Korea
[69]Kyungpook National University, Daegu, Korea
[70]Chonnam National University, Institute for Universe and Elementary Particles, Kwangju, Korea
[71]Korea University, Seoul, Korea
[72]University of Seoul, Seoul, Korea
[73]Sungkyunkwan University, Suwon, Korea
[74]Vilnius University, Vilnius, Lithuania
[75]Centro de Investigacion y de Estudios Avanzados del IPN, Mexico City, Mexico
[76]Universidad Iberoamericana, Mexico City, Mexico
[77]Benemerita Universidad Autonoma de Puebla, Puebla, Mexico
[78]Universidad Autónoma de San Luis Potosí, San Luis Potosí, Mexico
[79]University of Auckland, Auckland, New Zealand
[80]University of Canterbury, Christchurch, New Zealand
[81]National Centre for Physics, Quaid-I-Azam University, Islamabad, Pakistan
[82]National Centre for Nuclear Research, Swierk, Poland
[83]Institute of Experimental Physics, Faculty of Physics, University of Warsaw, Warsaw, Poland
[84]Laboratório de Instrumentação e Física Experimental de Partículas, Lisboa, Portugal
[85]Joint Institute for Nuclear Research, Dubna, Russia
[86]Petersburg Nuclear Physics Institute, Gatchina (St. Petersburg), Russia
[87]Institute for Nuclear Research, Moscow, Russia
[88]Institute for Theoretical and Experimental Physics, Moscow, Russia
[89]P.N. Lebedev Physical Institute, Moscow, Russia
[90]Skobeltsyn Institute of Nuclear Physics, Lomonosov Moscow State University, Moscow, Russia
[91]State Research Center of Russian Federation, Institute for High Energy Physics, Protvino, Russia
[92]University of Belgrade, Faculty of Physics and Vinca Institute of Nuclear Sciences, Belgrade, Serbia
[93]Centro de Investigaciones Energéticas Medioambientales y Tecnológicas (CIEMAT), Madrid, Spain
[94]Universidad Autónoma de Madrid, Madrid, Spain
[95]Universidad de Oviedo, Oviedo, Spain
[96]Instituto de Física de Cantabria (IFCA), CSIC-Universidad de Cantabria, Santander, Spain
[97]CERN, European Organization for Nuclear Research, Geneva, Switzerland
[98]Paul Scherrer Institut, Villigen, Switzerland
[99]Institute for Particle Physics, ETH Zurich, Zurich, Switzerland
[100]Universität Zürich, Zurich, Switzerland
[101]National Central University, Chung-Li, Taiwan
[102]National Taiwan University (NTU), Taipei, Taiwan
[103]Chulalongkorn University, Bangkok, Thailand
[104]Cukurova University, Adana, Turkey
[105]Middle East Technical University, Physics Department, Ankara, Turkey
[106]Bogazici University, Istanbul, Turkey
[107]Istanbul Technical University, Istanbul, Turkey
[108]National Scientific Center, Kharkov Institute of Physics and Technology, Kharkov, Ukraine
[109]University of Bristol, Bristol, United Kingdom
[110]Rutherford Appleton Laboratory, Didcot, United Kingdom
[111]Imperial College, London, United Kingdom
[112]Brunel University, Uxbridge, United Kingdom
[113]Baylor University, Waco, Texas, USA
[114]The University of Alabama, Tuscaloosa, Alabama, USA
[115]Boston University, Boston, Massachusetts, USA
[116]Brown University, Providence, Rhode Island, USA
[117]University of California, Davis, Davis, California, USA
[118]University of California, Los Angeles, Los Angeles, California, USA
[119]University of California, Riverside, Riverside, California, USA
[120]University of California, San Diego, La Jolla, California, USA
[121]University of California, Santa Barbara, Santa Barbara, California, USA
[122]California Institute of Technology, Pasadena, California, USA
[123]Carnegie Mellon University, Pittsburgh, Pennsylvania, USA
[124]University of Colorado at Boulder, Boulder, Colorado, USA

[125]*Cornell University, Ithaca, New York, USA*
[126]*Fairfield University, Fairfield, Connecticut, USA*
[127]*Fermi National Accelerator Laboratory, Batavia, Illinois, USA*
[128]*University of Florida, Gainesville, Florida, USA*
[129]*Florida International University, Miami, Florida, USA*
[130]*Florida State University, Tallahassee, Florida, USA*
[131]*Florida Institute of Technology, Melbourne, Florida, USA*
[132]*University of Illinois at Chicago (UIC), Chicago, Illinois, USA*
[133]*The University of Iowa, Iowa City, Iowa, USA*
[134]*Johns Hopkins University, Baltimore, Maryland, USA*
[135]*The University of Kansas, Lawrence, Kansas, USA*
[136]*Kansas State University, Manhattan, Kansas, USA*
[137]*Lawrence Livermore National Laboratory, Livermore, California, USA*
[138]*University of Maryland, College Park, Maryland, USA*
[139]*Massachusetts Institute of Technology, Cambridge, Massachusetts, USA*
[140]*University of Minnesota, Minneapolis, Minnesota, USA*
[141]*University of Mississippi, Oxford, Mississippi, USA*
[142]*University of Nebraska-Lincoln, Lincoln, Nebraska, USA*
[143]*State University of New York at Buffalo, Buffalo, New York, USA*
[144]*Northeastern University, Boston, Massachusetts, USA*
[145]*Northwestern University, Evanston, Illinois, USA*
[146]*University of Notre Dame, Notre Dame, Indiana, USA*
[147]*The Ohio State University, Columbus, Ohio, USA*
[148]*Princeton University, Princeton, New Jersey, USA*
[149]*University of Puerto Rico, Mayaguez, Puerto Rico*
[150]*Purdue University, West Lafayette, Indiana, USA*
[151]*Purdue University Calumet, Hammond, Indiana, USA*
[152]*Rice University, Houston, Texas, USA*
[153]*University of Rochester, Rochester, New York, USA*
[154]*The Rockefeller University, New York, New York, USA*
[155]*Rutgers, The State University of New Jersey, Piscataway, New Jersey, USA*
[156]*University of Tennessee, Knoxville, Tennessee, USA*
[157]*Texas A&M University, College Station, Texas, USA*
[158]*Texas Tech University, Lubbock, Texas, USA*
[159]*Vanderbilt University, Nashville, Tennessee, USA*
[160]*University of Virginia, Charlottesville, Virgina, USA*
[161]*Wayne State University, Detroit, Michigan, USA*
[162]*University of Wisconsin, Madison, Wisconsin, USA*

[a]Deceased.
[b]Also at Vienna University of Technology, Vienna, Austria.
[c]Also at CERN, European Organization for Nuclear Research, Geneva, Switzerland.
[d]Also at National Institute of Chemical Physics and Biophysics, Tallinn, Estonia.
[e]Also at California Institute of Technology, Pasadena, CA, USA.
[f]Also at Laboratoire Leprince-Ringuet, Ecole Polytechnique, IN2P3-CNRS, Palaiseau, France.
[g]Also at Suez Canal University, Suez, Egypt.
[h]Also at Zewail City of Science and Technology, Zewail, Egypt.
[i]Also at Cairo University, Cairo, Egypt.
[j]Also at Fayoum University, El-Fayoum, Egypt.
[k]Also at Helwan University, Cairo, Egypt.
[l]Also at British University in Egypt, Cairo, Egypt.
[m]Now at Ain Shams University, Cairo, Egypt.
[n]Also at National Centre for Nuclear Research, Swierk, Poland.
[o]Also at Université de Haute Alsace, Mulhouse, France.
[p]Also at Joint Institute for Nuclear Research, Dubna, Russia.
[q]Also at Skobeltsyn Institute of Nuclear Physics, Lomonosov Moscow State University, Moscow, Russia.
[r]Also at Brandenburg University of Technology, Cottbus, Germany.
[s]Also at The University of Kansas, Lawrence, KS, USA.
[t]Also at Institute of Nuclear Research ATOMKI, Debrecen, Hungary.

[u]Also at Eötvös Loránd University, Budapest, Hungary.
[v]Also at Tata Institute of Fundamental Research - HECR, Mumbai, India.
[w]Now at King Abdulaziz University, Jeddah, Saudi Arabia.
[x]Also at University of Visva-Bharati, Santiniketan, India.
[y]Also at Sharif University of Technology, Tehran, Iran.
[z]Also at Isfahan University of Technology, Isfahan, Iran.
[aa]Also at Shiraz University, Shiraz, Iran.
[bb]Also at Plasma Physics Research Center, Science and Research Branch, Islamic Azad University, Tehran, Iran.
[cc]Also at Facoltà Ingegneria, Università di Roma, Roma, Italy.
[dd]Also at Università degli Studi Guglielmo Marconi, Roma, Italy.
[ee]Also at Università degli Studi di Siena, Siena, Italy.
[ff]Also at University of Bucharest, Faculty of Physics, Bucuresti-Magurele, Romania.
[gg]Also at Faculty of Physics of University of Belgrade, Belgrade, Serbia.
[hh]Also at University of California, Los Angeles, CA, USA.
[ii]Also at Scuola Normale e Sezione dell'INFN, Pisa, Italy.
[jj]Also at INFN Sezione di Roma, Roma, Italy.
[kk]Also at University of Athens, Athens, Greece.
[ll]Also at Rutherford Appleton Laboratory, Didcot, United Kingdom.
[mm]Also at Paul Scherrer Institut, Villigen, Switzerland.
[nn]Also at Institute for Theoretical and Experimental Physics, Moscow, Russia.
[oo]Also at Albert Einstein Center for Fundamental Physics, Bern, Switzerland.
[pp]Also at Gaziosmanpasa University, Tokat, Turkey.
[qq]Also at Adiyaman University, Adiyaman, Turkey.
[rr]Also at Izmir Institute of Technology, Izmir, Turkey.
[ss]Also at The University of Iowa, Iowa City, IA, USA.
[tt]Also at Mersin University, Mersin, Turkey.
[uu]Also at Ozyegin University, Istanbul, Turkey.
[vv]Also at Kafkas University, Kars, Turkey.
[ww]Also at Suleyman Demirel University, Isparta, Turkey.
[xx]Also at Ege University, Izmir, Turkey.
[yy]Also at School of Physics and Astronomy, University of Southampton, Southampton, United Kingdom.
[zz]Also at INFN Sezione di Perugia, Università di Perugia, Perugia, Italy.
[aaa]Also at Utah Valley University, Orem, UT, USA.
[bbb]Now at University of Edinburgh, Scotland, Edinburgh, United Kingdom.
[ccc]Also at Institute for Nuclear Research, Moscow, Russia.
[ddd]Also at University of Belgrade, Faculty of Physics and Vinca Institute of Nuclear Sciences, Belgrade, Serbia.
[eee]Also at Argonne National Laboratory, Argonne, IL, USA.
[fff]Also at Erzincan University, Erzincan, Turkey.
[ggg]Also at Mimar Sinan University, Istanbul, Istanbul, Turkey.
[hhh]Also at KFKI Research Institute for Particle and Nuclear Physics, Budapest, Hungary.
[iii]Also at Kyungpook National University, Daegu, Korea.

Journal of Physics: Conference Series **331** (2011) 072019 doi:10.1088/1742-6596/331/7/072019

CMS distributed computing workflow experience

Jennifer Adelman-McCarthy[1], Oliver Gutsche[1], Jeffrey D. Haas[2], Harrison B. Prosper[2],Valentina Dutta[3], Guillelmo Gomez-Ceballos[3], Kristian Hahn[3], Markus Klute[3], Ajit Mohapatra[4], Vincenzo Spinoso[5], Dorian Kcira[6], Julien Caudron[7], Junhui Liao[7], Arnaud Pin[7], Nicolas Schul[7], Gilles De Lentdecker[8], Joseph McCartin[9], Lukas Vanelderen[9], Xavier Janssen[10],Andrey Tsyganov[11], Derek Barge[12] and Andrew Lahiff[13]

[1] Fermi National Accelerator Laboratory, USA
[2] Florida State University, USA
[3] Massachusetts Institute of Technology, USA
[4] University of Wisconsin-Madison, USA
[5] INFN Bari, Italy
[6] California Institute of Technology, USA
[7] Universite Catholique de Louvain, Belgium
[8] Universite Libre de Bruxelles, Belgium
[9] Universiteit Gent, Belgium
[10] Universiteit Antwerpen, Belgium
[11] Joint Inst. for Nuclear Research, Russian Federation
[12] University of California Santa Barbara, USA
[13] Rutherford Appleton Laboratory, United Kingdom

Abstract. The vast majority of the CMS Computing capacity, which is organized in a tiered hierarchy, is located away from CERN. The 7 Tier-1 sites archive the LHC proton-proton collision data that is initially processed at CERN. These sites provide access to all recorded and simulated data for the Tier-2 sites, via wide-area network (WAN) transfers. All central data processing workflows are executed at the Tier-1 level, which contain re-reconstruction and skimming workflows of collision data as well as reprocessing of simulated data to adapt to changing detector conditions. This paper describes the operation of the CMS processing infrastructure at the Tier-1 level. The Tier-1 workflows are described in detail. The operational optimization of resource usage is described. In particular, the variation of different workflows during the data taking period of 2010, their efficiencies and latencies as well as their impact on the delivery of physics results is discussed and lessons are drawn from this experience. The simulation of proton-proton collisions for the CMS experiment is primarily carried out at the second tier of the CMS computing infrastructure. Half of the Tier-2 sites of CMS are reserved for central Monte Carlo (MC) production while the other half is available for user analysis. This paper summarizes the large throughput of the MC production operation during the data taking period of 2010 and discusses the latencies and efficiencies of the various types of MC production workflows. We present the operational procedures to optimize the usage of available resources and we the operational model of CMS for including opportunistic resources, such as the larger Tier-3 sites, into the central production operation.

1. Introduction

In 2010, the LHC [1] at CERN started its physics program with the first long run collecting proton-proton collisions at a center-of-mass energy of 7 TeV. 2010 also marked the final transition of the CMS [2] computing systems from preparation to operation. This paper will describe the experience of the CMS collaboration with the data processing and Monte-Carlo (MC) production in 2010.

Several ingredients were necessary to complete these tasks, which include: software [5], workload and data management tools [6, 7], grid infrastructure [3, 4], CMS Tier-1 and Tier-2 sites and the operation teams to keep everything alive and working [8]. We would like to thank the developers of our tools, our integration teams, the CMS facility operations group, those who care for the functionality of sites, and all the rest of CMS who contribute to this team effort.

The Compact Muon Solenoid (CMS) Computing Model [9] is designed as a hierarchical structure of computing centers with well defined roles, located throughout the world. The CMS Computing resources follow a tree model of tier levels (computing centers) ranging from Tier 3 to Tier 0. These resources are part of the World-wide Large Hadron Collider Computing Grid (WLCG [10]).

A large majority of the CMS computing capacity is not located at the LHC host laboratory CERN, but is distributed around the world. CERN is at the top of the hierarchical structure as the only Tier-0 center. The Tier-0 is responsible for the safe keeping of the first copy of experimental RAW data (archived on tape, considered a cold backup copy not intended to be accessed frequently), prompt data processing, prompt calibration, and the distribution of data to all Tier-1 centers.

There are a total of 7 Tier-1 centers, located at large universities and national laboratories in France, Germany, Italy, Spain, Taiwan, the United Kingdom and the United States. Tier-1s are at the center of the data flow. The Tier-0 sends the raw and reconstructed data for custodial care (archived on tape) to the Tier-1s. Monte-Carlo simulations produced at the Tier-2s are also sent to the Tier-1s for custodial care (archived on tape). The Tier-1s perform event re-reconstruction and skimming workflows on the data, where the outputs are distributed to the Tier-2s. Since August 2010, the Tier-1s also process Monte Carlo simulations of data if resources are available.

The Tier-2 centers are located at about 50 sites around the world. The Tier-2s do not have tape systems available, all data are cached on disk for analysis. The Tier-2 level represents the primary analysis facilities for CMS. Monte Carlo simulations are mainly carried out at the Tier-2 level as well. The Tier-2s rely on Tier-1s as their link to CMS data and MC simulations for analysis access.

The Tier-3 level is special in the sense that it is not a pledged resource of the experiments, but rather voluntarily provided to CMS. A Tier-2 must have sufficient CPU and disk space to produce Monte Carlo simulations and to support CMS analysis activities, while a Tier-3 does not have these requirements. Therefore, while CMS can use Tier-3 resources for opportunistic purposes, it cannot rely on their availability.

2. Processing at Tier-1 level

The Tier-1 level takes care of all processing that needs input from samples custodially archived on tape. In the following, CMS' concepts of data partitioning and the characteristics of Tier-1 workflows are introduced followed by the summary of processing during 2010.

2.1. Data Partitioning

CMS stores events recorded by the detector system and its derived products in files of different contents. The following main data tiers characterize the content of these files:

- RAW: RAW event data contains detector data and trigger information. The largest contributor to the RAW event size of the order of 500 kB is the silicon strip detector.

- RECO: The Reconstructed data (RECO) contain reconstructed physics quantities derived from RAW data. Detector calibration constants are applied and physics objects are identified. A RECO event is about 400 kB in size.
- AOD: The Analysis Object Data (AOD) contains a small subset of the RECO data format, sufficient for 90% of all physics analyses. An AOD event is about 120 kB in size.
- GEN-SIM-RAW: The RAW data tier originating from Monte Carlo (MC) simulations with the Generator (GEN) information and the Simulation (SIM) information added. A GEN-SIM-RAW event is about 1000 kB in size.
- GEN-SIM-RECO: Corresponds to RECO using GEN-SIM-RAW as input and contains small amounts of generator and simulation information. A GEN-SIM-RECO event is about 500 kB in size.
- AODSIM: The AODSIM format contains a small subset of the GEN-SIM-RECO data format sufficient for 90% of all analyses. An AODSIM event is about 140 kB in size.

CMS determines the luminosity corresponding to the recorded data in granularity of a Luminosity Section (LS) which constitutes 23 seconds of data taking. In case of MC simulation, a LS holds the events of a single MC production job. A LS is always kept intact in a single file and not split between several files to guarantee bookkeeping of the luminosity during processing and analysis. The size of individual files is 2-10 GB, optimized for tape storage.

Files are grouped together into file-blocks of 500 to 1000 files. Blocks contain no more than one run. Site location is tracked on a block level and only complete blocks are available for processing, partially transferred blocks have to wait for the completion of the transfer to be processed.

Data from the detector is split into Primary Datasets (PD) by trigger selections by physics interest. Examples are the Electron, Photon and Jet PDs. MC samples are split by their generator configuration, like QCD or TTBar.

2.2. Processing workflows

The Production Agent (PA) [11] is the main component of the CMS Workload Management System, which enables large processing of data using CMS software. It is a message based modular python workload management system. There are 16 autonomous components, python daemons, within the PA. These components take care of job creation, submission, tracking, error handling, job cleanup, data merging and data publication.

CMS distinguishes two main processing workflow types on the Tier-1 level: data re-reconstruction and MC re-digitization/re-reconstruction, (a) and b) in Fig. 1). During data re-reconstruction, the Tier-1 sites process RAW data with newer software releases and/or updated alignment and detector condition constants, producing data in both the RECO and AOD formats. The processing jobs can produce output file sizes that are too small and non-optimal for tape storage. Therefore, a dedicated merge step combines the unmerged outputs of several processing jobs with the same data format. The Tier-1s then skim the reconstructed data, extracting events of interest, in a separate step. These events are written out into files of RECO or a combination of RECO and RAW formats and follow the same processing/merge cycle as the re-reconstruction (see a in Fig. 1).

The Tier-1 sites also reprocess Monte Carlo generated events with newer software versions and/or newer alignment and calibration constants. The GEN-SIM-RAW input is re-digitized producing an updated version of the simulated RAW data, which are then re-reconstructed. In order to eliminate multi-step processing (processing of a dependent workflow after waiting for completion of the merge step of the previous workflow), maximize computer resources and improve the production efficiency significantly, Chained Processing (CI) was established (see b in Fig. 1). In Chained Processing, all workflow steps are processed one after the other on

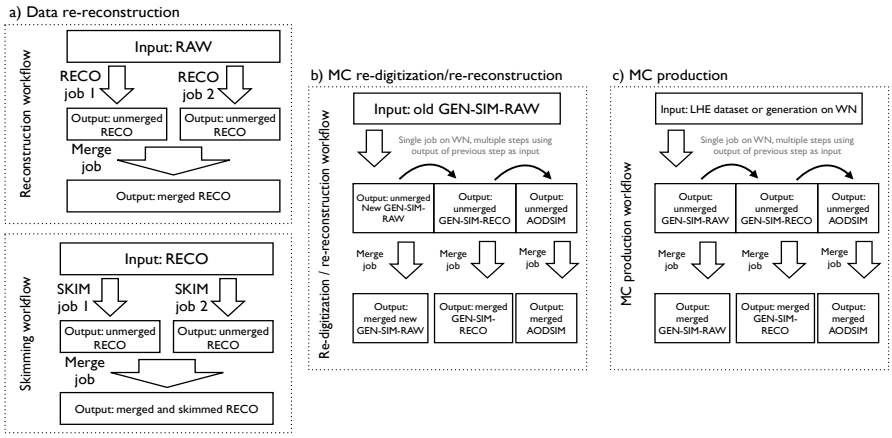

Figure 1. Schematic overview of CMS' processing and production workflows: a) data re-reconstruction, b) MC re-digitization/re-reconstruction, c) MC production.

the same workernode using the output of the previous step as input for the following step. In Chained Processing, the outputs are merged individually eliminating the need to wait for the completion of the merge step of the previous workflow.

Processing of input samples is not split between different sites but rather processed completely at a single site. The processing of a complete sample is optimized by splitting it into smaller jobs. Each job should run about 8-12 hours to optimize resource usage. Job splitting is done by file to keep luminosity sections intact. We also follow a run-based merging policy to avoid having files contain more than one run. During the processing, the intermediate output is stored on disk-only areas.

2.3. Processing experience in 2010

The Tier-1 sites have been stable during the 2010 collisions data taking period [8]. Apart from their custodial allocation, all RAW collision data samples have been distributed to all Tier-1s to increase processing flexibility. This was possible because of the small total data size. CMS collected cosmic data early in 2010. In March, the Large Hadron Collider (LHC) provided proton-proton collisions, but the bulk of the integrated luminosity has been collected since September, when beam luminosity increased due to the use of closely packed bunches in proton bunch trains. CMS recorded collisions at a data taking rate of 300Hz, with spikes reaching 700Hz. The primary datasets per data acquisition era are shown in Table 1.

CMS performed 3 MC re-digitization/re-reconstruction campaigns in 2010 (see Tab. 2) that produced significantly more output than the data taking including the over 16 re-reconstruction passes (see Tab. 3). The CPU needs for the re-reconstruction passes were small compared to the needs for the MC campaigns but increased after September 2010 with the increasing collected luminosity (see (*left*) in Fig. 2).

The Tier-1 production has been very successful during 2010 and the tools and operation teams significantly contributed to the timely publication of the first physics results of CMS, but not without challenges. Production efficiency suffered from lengthy debugging efforts before production quality of the workflows could be reached. The large number of requests extended the time spent on bookkeeping and completion of the workflows. This caused additional false starts due to pilot error. All processing of data requires a detailed post-mortem for each failed job; this was labor intensive and time consuming with the tools at hand. The production infrastructure

PD	Com10	2010A	2010B
Cosmics	593.1	264.2	68.2
MinimumBias	1339.9	119.2	19.0
ZeroBias	438.7	34.9	14.9
JetMETTau		168.0	
JetMET		31.6	
BTau		27.8	12.5
EG		61.8	
Mu		56.0	10.6
MuOnia		37.4	11.8
Commissioning		181.9	7.2
Jet			13.1
MultiJet			1.1
METFwd			8.2
Total	2371.7	982.7	166.9

Table 1. Number of Million events in Primary Datasets per Data Acquisition Era in 2010.

	Spring10	Summer10	Fall10
GEN-SIM-RAW			
Events (M)	658.6	592.5	469.0
Size (TB)	481.3	412.4	322.5
GEN-SIM-RECO			
Events (M)	744.6	592.0	469.0
Size (TB)	267.7	234.5	165.7
AODSIM			
Events (M)	658.0	588.0	469.0
Size (TB)	78.6	57.3	39.3

Table 2. Number of Million events (M) per MC re-digitization/re-reconstruction campaign in 2010.

	CMS Internal	Events (M)	Luminosity	Start date	Completion (days)
1	Jan23ReReco	40.7	N/A	01/23/10	2
2	Jan29ReReco	44.6	N/A	01/29/10	3
3	Feb9ReReco	44.6	N/A	02/09/10	2
4	Mar1rstReReco	6.2	N/A	03/01/10	5
5	Mar3rdReReco	223.0	N/A	03/03/10	5
6	Apr1ReReco	10.5	0.032	04/01/10	3
7	Apr20ReReco	168.8	0.516	04/20/10	1
8	May6thReReco	338.7	1.663	05/06/10	4
9	May27thReReco	824.4	18.195	05/27/10	3
10	Jun9thReReco (ICHEP)	1003.3	19.593	06/09/10	7
11	Jun14thReReco	1012.0	50.343	06/14/10	6
12	Jul6thReReco	26016800	83.291	07/06/10	1
13	Jul15thReReco	40.4	193.420	07/15/10	1
14	Jul16thReReco (ICHEP)	16.6	132.605	07/16/10	1
15	Jul26thReReco	11.5	115.010	07/26/10	1
16	Sep17ReReco	1295.8	3493.308	09/17/10	10

Table 3. Re-Reconstruction Passes During 2010; 7 TeV re-reconstruction passes start April 1st, 2010

imposed its own restrictions due to performance reasons; a single instance was limited to 3000 jobs running in parallel. Due to the messaging based design, jobs got lost during processing whose recovery was lengthy and difficult if not impossible in some cases.

3. MC production at the Tier-2 level

Tier-2s represent the primary CMS MC production and analysis facilities, where 50% of the resources are committed to producing MC simulations and 50% are committed for use in CMS analysis. Output from the MC production is archived on tape at the Tier-1 centers. The Tier-2s

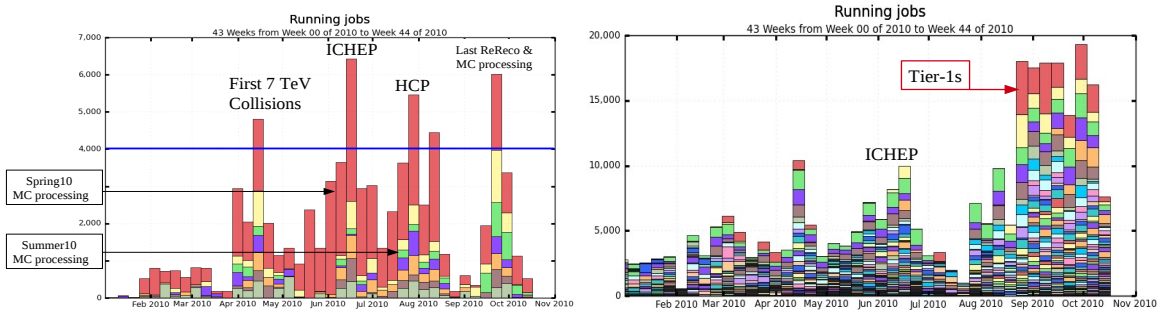

Figure 2. CMS processing (*left*) and MC production (*right*) jobs during 2010.

are divided up into geographic regions, grouped around Tier-1s. The NorduGrid region stands on its own because of their different middleware technology. These regions are managed by 5 operator teams.

3.1. MC Production

CMS requires a large number of MC events to supplement the data physics studies. The task of generating billions of MC events in a timely manner is accomplished using PAs like the Tier-1 processing. MC events are produced at all Tier-2 sites, a few opportunistic Tier-3 sites and, as of August 2010, Tier-1 sites in order to make better use of free resources. The MC production workflow is executed using a Chained Processing workflow type (see c in Fig. 1) where 3 outputs for GEN-SIM-RAW, GEN-SIM-RECO and AODSIM are stored. During 2009 and 2010, CMS produced over 3.5 billion events. Normal MC production capacity is about 300 Million events per month, however during September 2010 500 Million events were produced due to low-occupancy event compositions. Figure 2 shows the number of MC production jobs running in parallel in 2010. The increase in number of jobs in August 2010 is due to the significantly increased demand for MC events and the possibility to use free resources at the Tier-1 sites for production.

The MC production in 2009/2010 was very successful and could meet all demands. Also here, some issues were noticed. Apart from the same production infrastructure issues like the Tier-1 processing, the large number of different sites created a multitude of individual problems. Although the GRID infrastructure increased in stability over time and was very good in 2010 [8], occurring problems with basic services like compute and storage elements or individual workernodes increased the time effort for debugging and decreased the production efficiency.

4. Conclusions & Outlook

This has been a successful year for CMS' distributed workflow management in delivering input for successful first physics analysis with LHC proton-proton data: data were re-reconstructed 22 times; 3 Monte Carlo re-digitization/re-reconstruction campaigns were completed since the start of the 2010 run. Over the last 2 years, 3 billion Monte Carlo events were produced.

Looking into the future, developments to overcome shortcomings of the current workload management system (PA) are undergoing integration tests. The architecture of the new CMS Workload Management system (WMAgent) is based on a state machine rather than a messaging system to keep track of each and every processing job reliably and with 100% accountability. The new system will be the bases of all processing tasks at Tier-0, Tier-1, and MC production and analysis. The expected increase in production efficiency will make sure that CMS will meet its demands in producing input for physics analysis in the years to come.

5. Acknowledgements
We would like to thank the production tools and software development teams, the site administrators and facility teams, operation teams and all other CMS collaborators who contributed to a successful operation of all production and processing workflows on CMS' distributed computing infrastructure. We thank the international funding agencies amongst those the Department of Energy and the National Science Foundation for their support of this work.

[1] O. Bruning, P. Collier, P. Lebrun, S. Myers, R. Ostojic, J. Poole and P. Proudlock, "LHC design report. Vol. I: The LHC main ring", *CERN-2004-003*
[2] CMS Collaboration, "CMS, the Compact Muon Solenoid: Technical proposal",*CERN-LHCC-94-38*
[3] Enabling Grids for E-sciencE `http://www.eu-egee.org/`
[4] Open Science Grid `http://www.opensciencegrid.org/`
[5] C. Jones et al, "The new CMS event data model and framework", Proceedings for Computing in High-Energy Physics (CHEP '06), Mumbai, India, 13 Feb - 17 Feb 2006
[6] Egeland, R. and others, "Data transfer infrastructure for CMS data taking", Proceedings for XII Advanced Computing and Analysis Techniques in Physics Research, Erice, Italy (Nov. 2008)
[7] A.Afaq,et.al.,The CMS Dataset Bookkeeping Service,J.Phys.Conf.Ser,119,072001(2008).
[8] D. Bonacorsi, Experience with the CMS Computing Model from commissioning to collisions, CHEP 2010
[9] The CMS Collaboration CMS Computing Technical Design Report, CERN-LHCC-2005-023, (2005)
[10] Worldwide LHC Computing Grid (WLCG) urlhttp://lcg.web.cern.ch/LCG/public/default.htm
[11] Wakefield, S. and others, "Large Scale Job Management and Experience in Recent Data Challenges within the LHC CMS experiment, Proceedings for XII Advanced Computing and Analysis Techniques in Physics Research, Erice, Italy, Nov. 2008

Available on CMS information server

CMS DN -2009/021

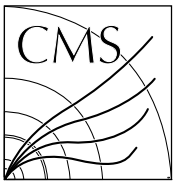

The Compact Muon Solenoid Experiment

Detector Note

The content of this note is intended for CMS internal use and distribution only

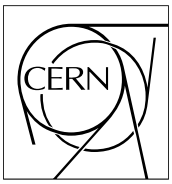

16 December 2009 (v2, 14 January 2010)

Response of Silicon Photomultipliers to Minimum Ionizing Particles

Alan Hahn

Fermi National Accelerator Laboratory, USA

Jeffrey D. Haas, Harrison B. Prosper, Sezen Sekmen

Florida State University, USA

Abstract

We present the results of an experiment that measured the response of silicon photomultiplier (SiPM) devices to minimum ionizing particles (MIPs). The SiPMs are proposed as replacements for the hybrid photodiodes (HPDs) of the Compact Muon Solenoid (CMS) Hadron Outer (HO) Calorimeter in the 2010-2011 upgrade. The experiment was performed as part of the HCAL Test Beam in July 2009 at CERN. The emphasis was on the investigation of the potential for an unexpected response from a MIP, which might result in a large spurious signal. We tested a new type of SiPM device, a micro-pixel avalanche photodiode (MAPD) manufactured by Zecotek, and found that a MIP typically fired a single pixel. The MIP interaction with the MAPD would fire two and sometimes three pixels, however with a lower rate.

1 Introduction

The Hadron Calorimeter (HCAL) Group of the Compact Muon Solenoid (CMS) Collaboration has proposed to upgrade the Hadron Outer (HO) calorimeter by replacing the hybrid photodiodes (HPD) with silicon photomultiplier (SiPM) devices during the 2010-2011 shutdown. HPDs and SiPMs are both photodetectors sensitive to a single photon. Until recently, the only technology available for this purpose has been photomultiplier tubes which are fragile, large, and sensitive to magnetic fields. SiPMs are semiconductor devices consisting of an avalanche photodiode matrix on a common silicon substrate. SiPMs are expected to perform better than HPDs because they have a higher quantum efficiency, a good charge resolution, a larger gain, much lower power consumption and are insensitive to magnetic fields. The SiPMs may also prove useful as a muon trigger due to their sensitivity to minimum ionizing particles (MIPs).

During the Large Hadron Collider (LHC) run, a barrage of charged particles will enter the CMS calorimeter system, so it is important to understand how a MIP interaction affects each part of the detector. We are interested in characterizing a MIP interaction with a SiPM in order to assess the potential of unexpected large spurious responses to this type of interaction. An experiment to investigate this was carried out during the HCAL Test Beam in July 2009 at CERN. Here we focus on results from a special type of SiPM called a micro-pixel avalanche photodiode (MAPD). This note is organized as follows: In Section 2 we give a description of the HO, SiPMs and MAPDs. In Section 3, we give an overview of the experiment, describe the setup, the devices tested and the operation. In Section 4 we present the analysis followed by our conclusions in Section 5.

2 Description of hardware

2.1 Hadron Outer calorimeter

The combined system of Electromagnetic Calorimeter barrel (EB) and Hadron Calorimeter barrel (HB) with $|\eta| < 1.4$ is not thick enough to fully contain hadronic showers. The effective interaction length has been increased by placing hadron detectors inside the muon chambers yet outside the cryostat. CMS has 5 rings numbered -2, -1, 0, +1, +2. Figure 1 shows the schematic view of a quarter of the HCAL. In ring 0, the Hadron Outer calorimeter (HO) [4] is made up of two layers of scintillators placed on either side of a 19.5 cm thick piece of iron at radial distances of 3820 mm and 4070 mm. In all other rings, the HO has a single layer of scintillator at a radial distance of 4070 mm.

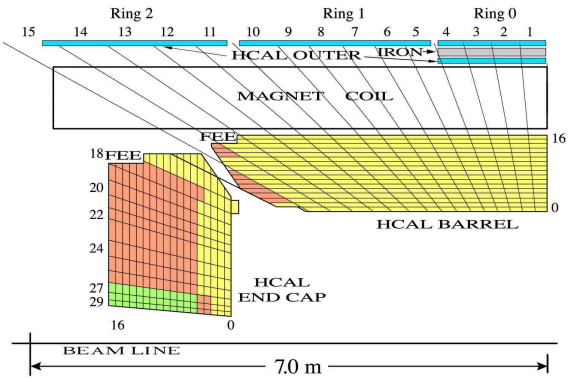

Figure 1: Schematic view of a quarter of the Hadron Calorimeter (HCAL).

Figure 2 shows the schematic view of an HO tray. Light from the scintillator tiles is collected using multi-clad Y11 Kuraray wavelength shifting (WLS) fibers. The scintillator tiles are packed into a single unit, which is $\sim 5^\circ$ in ϕ but covers the entire span of a muon ring in the z direction. The light is then transported to the photodetectors located on the return yoke, with a multi-clad Kuraray clear fiber. Currently, HO utilizes HPDs as photodetectors that convert the scintillator light into electrical charge. The charge is then measured and encoded into a non-linear digital scale of 25 nanoseconds time bins through a charge integrator that uses the Large Hadron Collider (LHC) clock.

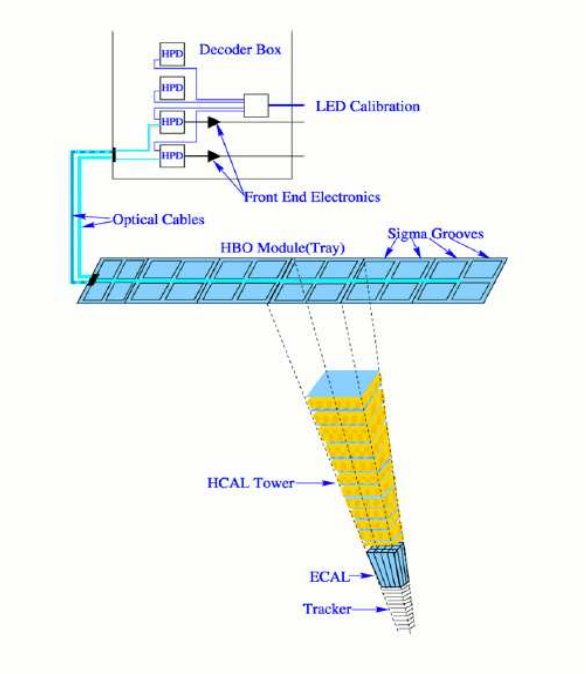

Figure 2: Schematic view of an HO tray shown with individual tiles and the corresponding grooves for wavelength shifting fibers. Each tile is mapped to a tower of HB. Optical fibers from the tray extend to the decoder box, which contains the photodetector and readout electronics [4].

2.2 SiPMs

SiPMs consist of an avalanche photodiode matrix on a common silicon substrate. They work in Geiger mode where each pixel in the matrix has its own resistor, as is shown in Figure 3.

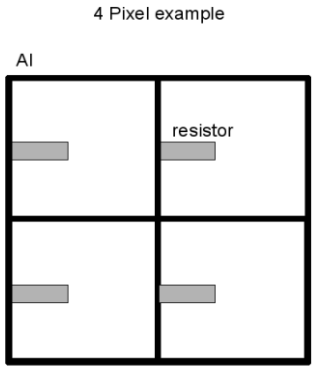

Figure 3: Top view of a SiPM device with four pixels.

Figure 4 shows a cut out view of a single SiPM pixel. SiPMs are activated by an excess of free electrons in the device's depletion region. The depletion region is created with a p-n junction, where the excess electrons in the n-type doped material are attracted to the holes in the p-type region, and the holes are attracted to the electrons in the n-type doped region. When a free electron enters this system, it propagates along the applied electric field as shown in Figure 5. SiPMs operate as reverse bias diodes. An example of a reverse bias diode with a depletion region is shown in the center of Figure 6. A pixel is activated (in Geiger mode) when a free electron in the depletion region with an applied electric field triggers a self sustaining avalanche of electrons localized to the triggered pixel. Each pixel is kept in this metastable state where any electron-hole pair created in the depletion region discharges

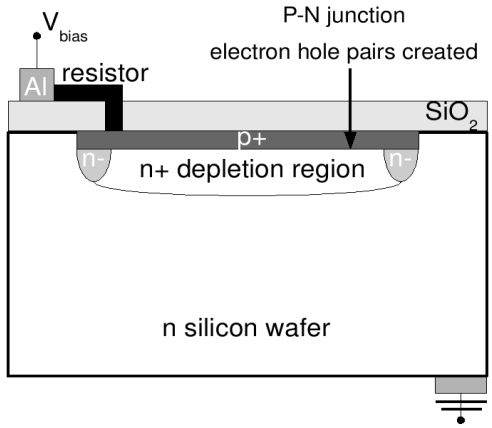

Figure 4: Side cut view of one pixel, where $\mathrm{V_{bias}}$ is the bias voltage, Al is the Aluminum conducting band outlining the pixel matrix, $\mathrm{SiO_2}$ is the insulation layer and the p+ and n+ regions make up the p-n junction. The n- region separates multiple pixel activations, and the body of the device is a non-doped n-type silicon wafer $\sim 50\ \mu\mathrm{m}$, where the doping is $\sim 4\ \mu\mathrm{m}$.

an individual pixel. The bias voltage then recharges the device back to its metastable state. In most SiPMs, the voltage drop is regulated by a resistor. In Geiger mode, these pixels operate as digital devices, either on or off.

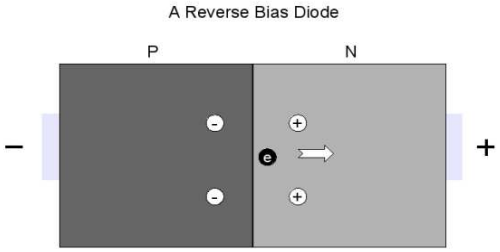

Figure 5: Motion of a free electron in a diode.

When a photon or MIP interacts with a pixel, the charge liberated in the pixel is given by

$$Q = C * (V_{\mathrm{bias}} - V_{\mathrm{bd}}), \tag{1}$$

where C is the capacitance of the SiPM, V_{bias} is the bias voltage applied to the SiPM, and V_{bd} is the breakdown voltage of the pixel. In these devices, a single pixel can fire while other pixels in the same device remain in their metastable state. The greater the number of pixels in a device, the larger the number of photons or MIPs that can be detected. It is possible, however, for a second photon passing through a fired pixel to go undetected. Multiple interactions during a single pixel discharge can introduce a saturation effect, as described further in Section 3.2.1.

SiPMs have excellent features, such as: high quantum efficiency, good charge resolution, fast response, compact size, gains of $\sim 10^6$, are impervious to magnetic fields and require low bias voltage (30-70V). Two types of SiPMs are under consideration for the HO upgrade: one from Hamamatsu and a Zecotek MAPD. Our study focuses on the latter.

2.3 MAPDs

Figure 7 shows five 3×3 mm^2 micro-pixel avalanche photodiode (MAPD) devices. For simplicity, hereafter we shall refer to the micro-pixels as pixels.

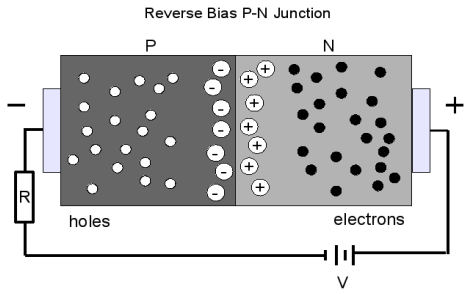

Figure 6: A reversed bias diode with a depletion region in the center.

Figure 7: Five Zecotek MAPDs [8].

MAPDs have a different design compared to the standard SiPM described in Section 2.2. The new design has a higher pixel density, which increases the dynamic range up to $\sim 10^4$ photons. This was the largest dynamic range of the devices we tested. The MAPDs use the same type of p-n junction as the standard SiPMs, however, MAPDs have a single surface sensitive to interactions instead of a discrete surface matrix with inactive regions as shown in Figure 8. The matrix of avalanche regions are placed inside the silicon substrate at a depth of $\sim 4\mu\mathrm{m}$ using a special distribution of the inner electric field [11]. This matrix is made of $\sim 10^4$ independent avalanche regions per mm^2 with individual micro-wells for charge collection and trapping. Charge collection in individual micro-wells provides a local self-quenching of the avalanche processes. Quite remarkably, this means there is no need to use resistors. However, manufacturing the MAPD takes a sophisticated process with epitaxial growing of extremely pure silicon wafers with deep ion implantation.

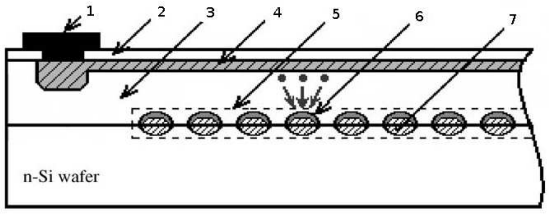

Figure 8: Side cut view of an MAPD with individual micro-wells. The numbers point to the following: 1. common metal electrode, 2. buffer layer of silicon oxide, 3. epitaxial silicon layer of p-type conductivity, 4. a high-doped silicon layer of p-type conductivity, 5. a region with micro-wells, 6. local avalanche regions and, 7. individual micro-wells [10].

3 The experiment

3.1 Setup

The experiment took place as a part of the HCAL Test Beam 2009 at CERN. We were provided with muon, electron and pion beams having energies that ranged from $\sim$ 30 to 300 GeV. The beam size was determined by the distribution across a scintillator upstream of all experiments. The beam was roughly 15 mm wide and 20 mm in height with the highest density of particles at the center of the beam, where a 2.5 mm^2 SiPM would detect roughly 2% of the total available beam.

Our experiment, shown in Figure 9, was the first to interact with the beam. We used two SiPMs: a trigger SiPM to verify that a particle interaction took place, and a test SiPM to observe and evaluate the MIP interaction. The two SiPMs were positioned $\sim$1 cm apart along the beam direction. The trigger device was made from a Zecotek $3 \times 3\ \mathrm{mm}^2$ MAPD with a $3 \times 3\ \mathrm{mm}^2$ scintillator epoxied to its face, enclosed in a light tight material in order to avoid any photon induced interactions. The test device, a $1 \times 1\ \mathrm{mm}^2$ Zecotek MAPD, is $1/9$ of the area of the trigger device, so only a fraction of the particle beam on which we triggered passed through the test device. Both the trigger and the test devices were connected to separate amplifiers, separated by $\sim 4\ \mathrm{mm}$. The schematic is shown in Figure 10.

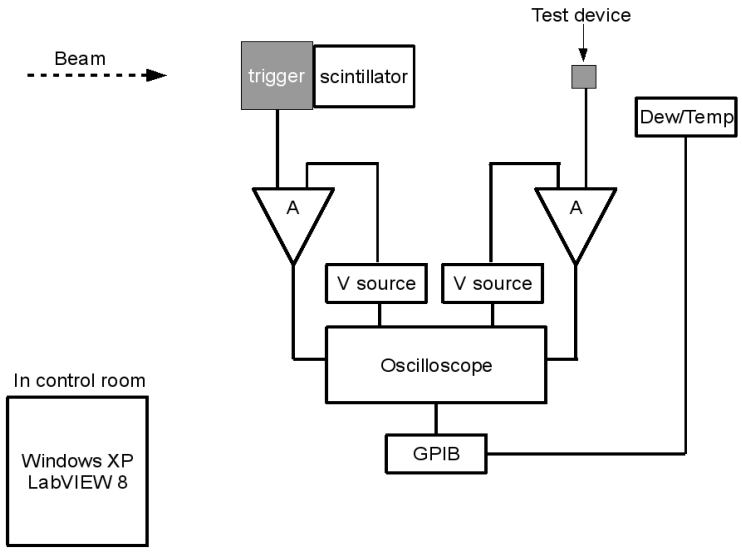

Figure 9: Experimental setup to measure a SiPM's response to MIPs.

The amplifiers were connected to a Model 6487 Keithley PicoAMMeter/Voltage Source device and a single Model D5A-0301-05 DVE switching power supply, 5V-4A output, operated remotely via LabVIEW. As a precaution, LabVIEW was set up to reduce the bias voltage by small incremental steps in the event of a power down situation, so the SiPMs would not be damaged. The output from each amplifier was connected to a LeCroy 1.5 GHz Oscilloscope, LCb84DXL. The data were transmitted to a Dell computer running Windows XP and LabVIEW 8, located in the control room, using a National Instruments GPIB-ENET/100 ethernet cable. The remote access was necessary due to access restriction during beam. The data were saved in binary formatted files and then converted to ASCII format to be used in the analysis.

3.2 Tested devices

We tested the following devices:

- Center of Perspective Technology and Apparatus (CPTA) $2.2 \times 2.2\ \mathrm{mm}^2$ (400 pixels per mm^2) [5],
- Fondazione Bruno Kessler (FBK) $1 \times 1\mathrm{mm}^2$ (400 pixels per mm^2)[6],

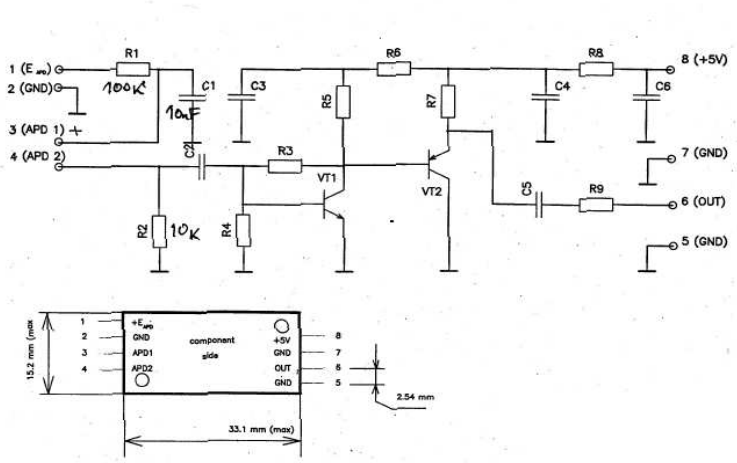

Figure 10: Schematic of amplifiers.

- Hamamatsu $1 \times 1\mathrm{mm}^2$ SiPM (400 pixels per mm^2)[7],
- Hamamatsu model MPPC S10931-050P(x) $3 \times 3\mathrm{mm}^2$ SiPM (400 pixels per mm^2)[7],
- Zecotek $1 \times 1\mathrm{mm}^2$ MAPD (14,000 pixels per mm^2)[8].

The first four are standard SiPMs with pixel sizes of 50×50 $\mu\mathrm{m}^2$ and the fifth is the MAPD. In this note, we only show results from the MAPD device, which was chosen due to its clean pulse shape and relatively low noise.

3.2.1 Saturation

When a pixel in Geiger mode, fires due to one or more photons the signal will be the same. If a photon or MIP passes through a SiPM while it is active, due to an earlier interaction, it is said to be *saturated* and the secondary interaction may go undetected. We simulated the saturation effect by modeling a SiPM as a collection of m boxes

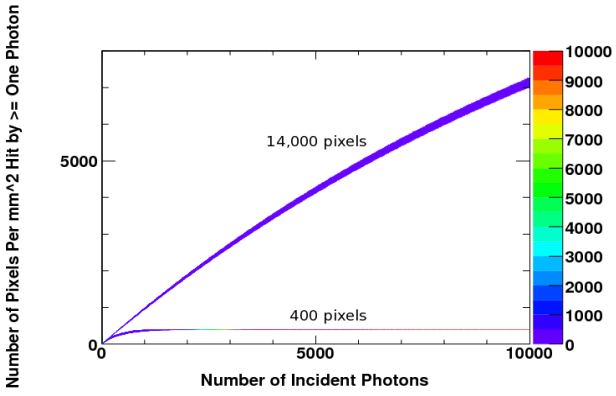

Figure 11: SiPM and MAPD pixel saturation effects simulated by a Monte Carlo study. Results are shown for 400 pixels per mm^2) and 14000 pixels per mm^2) devices.

(pixels) to which n photons were thrown k times. In Figure 11 we show the number of pixels having at least one photon for two different pixel densities where 400 pixels simulates a Hamamatsu SiPM and 14,000 pixels simulates a Zecotek MAPD after $k = 100000$ trials. The horizontal-axis shows the number of incident photons n and the vertical-axis shows the number of pixels p activated by at least one photon. The scale on the right is the

number of times in k trials p pixels are activated. As expected, for $n << m$, the chance that more than one photon lands in a pixel is very small, but as n increases, this probability also increases. The response function saturates in both devices.

3.3 Notes on operation

Our initial intent was to perform the analysis online during data acquisition. We planned to histogram the number of MIP interactions with the oscilloscope. However, during the first few days of the experiment observing the MIP signal above the thermal noise proved to be very difficult, and so a change in setup became necessary. In the new setup, the oscilloscope recorded the raw data and wrote out individual traces. The traces consist of a sequence of voltages recorded every 0.5 nanoseconds. This new setup enabled a closer offline inspection of the data.

The oscilloscope read data continuously from the trigger and test devices. When the trigger voltage exceeded 0.15 volts, the oscilloscope wrote out both the trigger and test device traces in LabVIEW via the GPIB connection. Since the oscilloscope was continually reading data, we were able to acquire data both before and after the trigger. We refer to each such trace, shown in Figure 12, as an *event*. The beam came in bunches $\sim$33 seconds apart. We recorded between 6 to 12 events per bunch crossing. Normally, the oscilloscope records a negative voltage, but in this analysis we invert the sign of the voltage for convenience. We observed, during early inspections, that the pulse shape generated from each device was dependent on the type of device as well as the device's surface area. We also observed that the voltage of the thermally activated pixels were approximately the same as the voltage from a MIP.

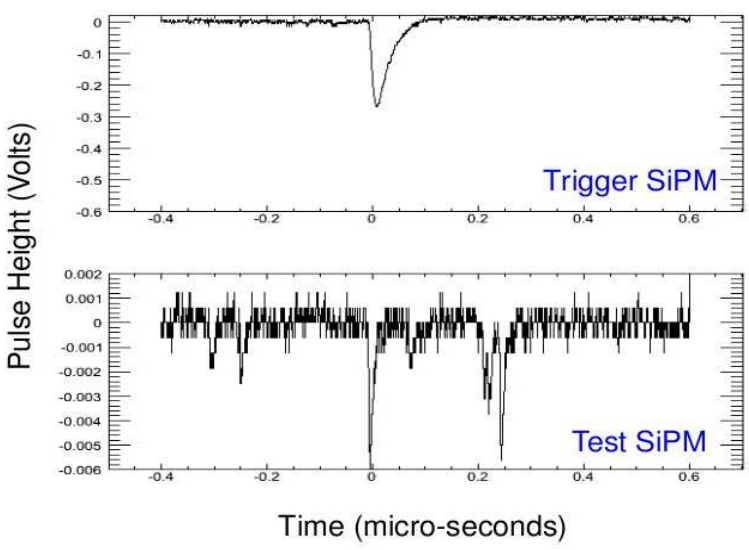

Figure 12: A trace of one event from LabVIEW showing the raw data from a $1 \times 1\mathrm{mm}^2$ MAPD.

4 Analysis

The focus of our analysis is to characterize the interaction of a MIP with a MAPD in terms of the number of pixels fired. We tried to achieve this by checking the signal correlation with the trigger, pulse shape, temperature, average and maximum voltage in a given time window, which are all presented below.

4.1 Signal correlation

We expect the time of signal pulses from a MIP interaction to correlate with (i.e., be in coincidence with) the trigger device at time $t = 0$ seconds, whereas the thermally activated pulses, which constitute the noise, should have a flat temporal distribution. We refer to the time window of signal pulses correlated with the trigger device as

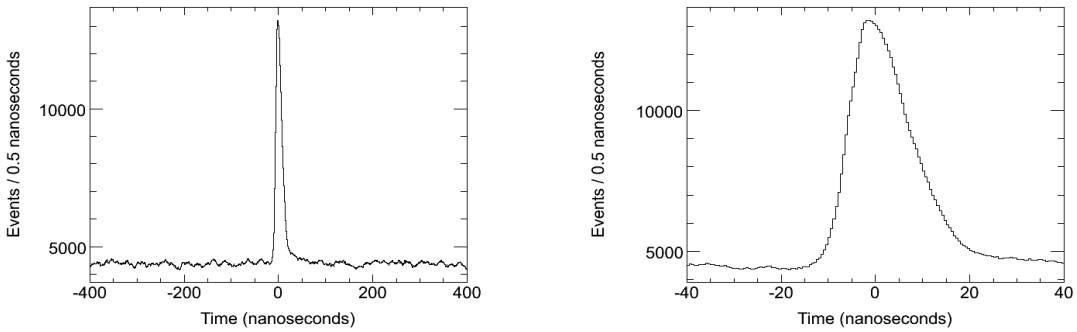

Figure 13: Time distribution of voltages greater than 0.001 Volts (left) and the same distribution in a smaller time window around $t = 0$ (right).

the *signal time window*, whereas a time window where the distribution is flat and comes from thermal noise will be referred to as the *noise time window*.

In Figure 13 we show the time distribution of voltages greater than 0.001 Volts. The right-hand plot is a zoom of the region around $t = 0$. The significant peak at $t = 0$ confirms that we are observing a MIP signal.

4.2 Pulse shape

The area of the pulse and the pulse height have a direct relationship to the number of pixels fired. We are interested in effects due to pixels firing from sources other than MIPs (such as delta rays). These affects will be observable in the pulse shape. The algorithm used to analyze the pulse shape is as follows:

- Voltage > 0.001 volts, to eliminate electronic noise.
- Start with the voltage at $t = 0$.
- Step left in 0.5 nanosecond time bins until the voltage drops below 0.001 volts, and define that time bin as the left time limit.
- Return to $t = 0$, and this time step right in 0.5 nanosecond bins until the voltage drops below 0.001 volts. Define that time bin as the right time limit.
- The voltage data between the two time limits is referred to as the signal pulse.
- The *maximum voltage* is the highest voltage between the two time limits.

Figure 14 shows two different trace sections with three pulses each. The left-hand plot shows three well-seperated pulses, where the pulse near $t = 0$ could be due to a MIP interaction, whereas the other two pulses are likely to be due to noise. In the right-hand plot, two of the pulses have significant overlap close to $t = 0$, one of which could be due to a MIP and the other is again likely to be due to noise. The signal pulse area and maximum voltage is expected to be proportional to the number of pixels fired during the MIP interaction. For example, if two pixels fire simultaneously during the MIP interaction, the area of the resulting pulse as well as the maximum voltage should be approximately twice as large compared to the case where one pixel fires. In order to investigate the pulse shape further, we examined the signal pulse's full-width-at-half-maximum (FWHM) and the maximum voltage using the following algorithm:

- Locate the maximum voltage as described above.
- Calculate half of the maximum voltage value.
- Go to the maximum voltage bin, and step left bin by bin until the bin with voltage closest to half of the maximum voltage is located. Define that bin as the left time limit.
- Return to the maximum voltage bin, and this time step right bin by bin until the bin with voltage closest to half of the maximum voltage is found. Define that bin as the right time limit.

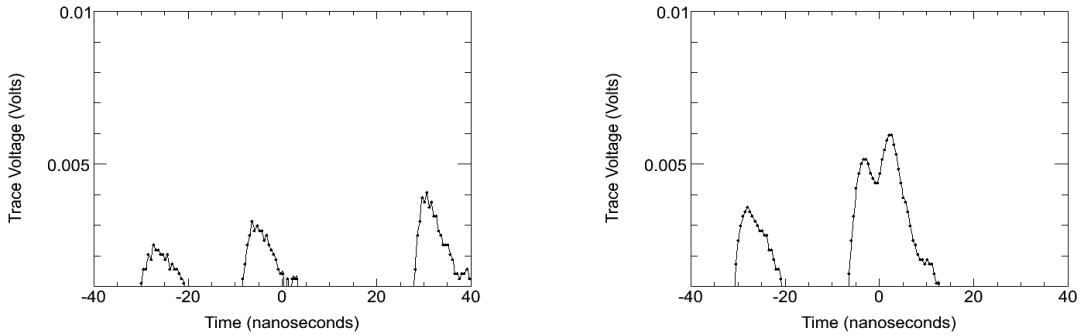

Figure 14: Section of a single trace over a voltage threshold of 0.001V with three pulses (left), where the pulse near $t = 0$ is likely to be due to a MIP, whereas the other two pulses are presumably due to noise. Another trace section with three pulses, where two pulses overlap close to $t = 0$ (right). One of the overlapping pulses is possibly due to a MIP interaction and the other is due to noise.

- The time difference between the two time limits is the FWHM.

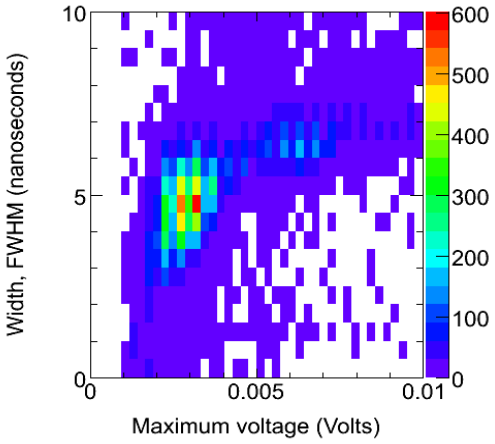

Figure 15: Distribution of FWHM versus maximum voltage for the signal.

Figure 15 shows the distribution of FWHM versus maximum voltage for the signal. We see that the maximum voltage is proportional to the FWHM for voltages less than 0.01 volts, and we observe a linear trend between 0.001 and 0.01 volts. For larger voltages, the relationship becomes non-linear.

4.2.1 Temperature

MAPDs are known to be temperature sensitive devices. Previous studies report a $\sim 5 - 10\%$ change in maximum voltage per degree Celsius. Figure 16 shows a plot of the maximum voltage versus ambient temperature. However due to limited statistics we were unable to observe this effect.

4.3 MIP Signal

We use two methods to quantify the MIP signal: (1) we integrate voltages in the signal time window, and (2) we find the maximum voltage in that window.

4.3.1 Definition using integration

In this method, we integrate the voltage over the time within the signal time window using the following algorithm:

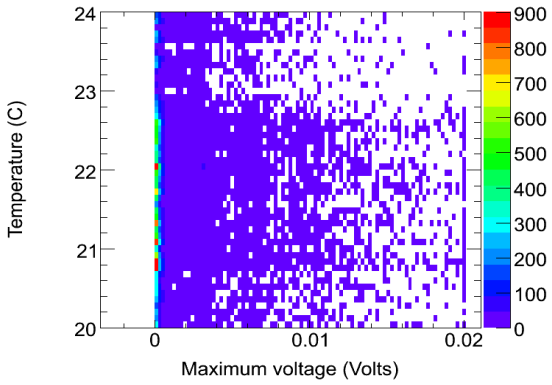

Figure 16: Ambient temperature versus maximum voltage.

- Sum the voltages within signal time window.
  - Set the signal time window to -10 to 10 nanoseconds, as suggested by Figure 13.
  - Sum the voltages within this time window.
- Sum the voltages within the noise time window.
  - Set the noise time window to -300.0 to -280.0 nanoseconds. Note that the window is chosen to be far away from $t = 0$ to avoid contributions from the signal.
  - Sum the voltages within this time window.
- For both cases, calculate the average voltage by dividing the voltage sum by the width of the time window.

In Figure 17, we plot the the distribution of average voltage for the signal and noise time windows. The right-hand plot, which is a zoom of the plot on the left clearly shows three peaks in the signal distribution, while the background distribution exhibits two peaks. In both cases, the large peak centered at zero corresponds to the pedestal [1)]. We expect the pedestals for the signal and the noise time windows to be the same, however, we found the shapes of the pedestals to be somewhat different. One possible reason could be a difference in the response of the electronics (such as amplifiers and power sources) in the presence and the absence of the MIP signal. The other two peaks in the signal distribution correspond to the firing of one and two pixels, respectively. On the other hand, the noise distribution shows only a single peak apart from the pedestal, presumably arising from the thermally activated pixels. We see no indication of an additional peak due to the simultaneous firing of two pixels. This is to be expected given that the thermal noise is random and the probability for two pixels to be thermally activated within the same time window is negligible.

4.3.2 Definition using maximum voltage

In this method, the signal is defined as the maximum (i.e., peak) voltage of the pulse using the following algorithm:

- Find the maximum voltage within the signal time window.
  - Set the signal time window to -5 to 0 nanoseconds, as suggested by Figure 13 where we see the rising edge of the distribution.
  - Find the maximum of the voltages within this time window.
- Find the maximum voltage within the noise time window.
  - Set the noise time window to -300.0 to -295.0 nanoseconds. Note again that the window is chosen to be far away from $t = 0$ to avoid contributions from the signal.
  - Find the maximum of the voltages within this time window.

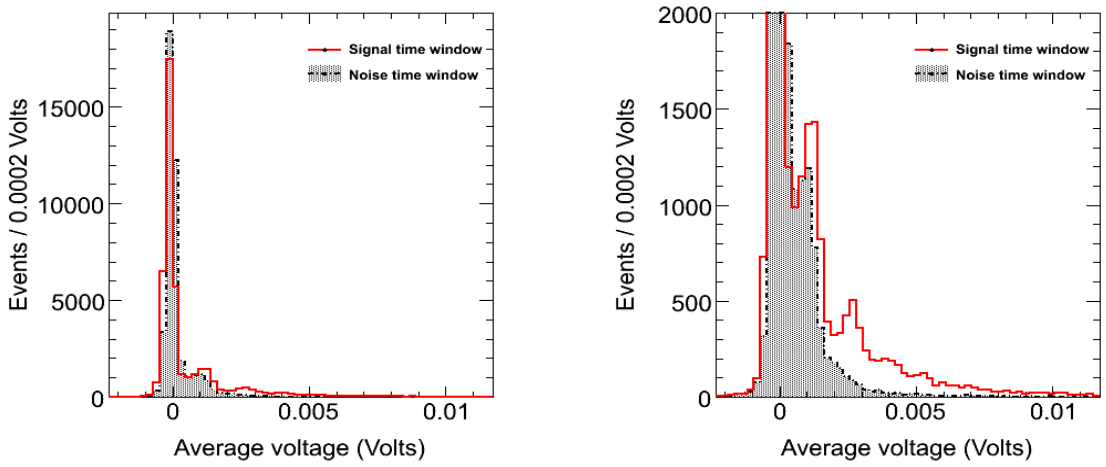

Figure 17: Average voltage distribution in signal (solid red line) and noise (shaded histogram with dashed black line) time windows, for all events (left) and for a zoom in the vertical direction (right).

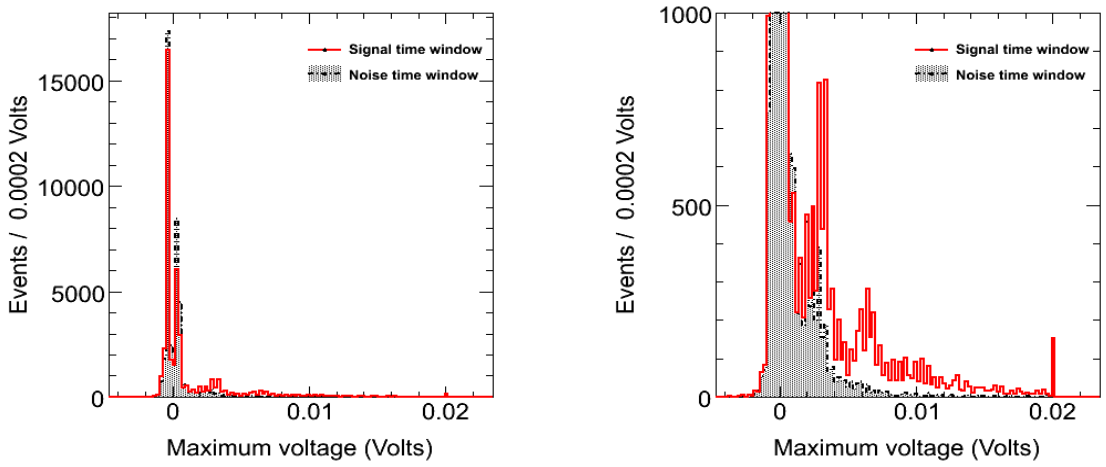

Figure 18: Maximum voltage distribution in signal (solid red line) and noise (shaded histogram with dashed black line) time windows, for all events (left) and for a zoom in the vertical direction (right).

Figure 18 shows the distribution of maximum voltage in the signal and noise time windows. In the right-hand plot, which is a zoom of the plot on the left, there are three major peaks in the signal distribution, and a hint of a fourth peak, whereas in the noise distribution two peaks are seen. As in the case with average voltage, the first peak in both signal and background corresponds to the pedestal. However, this time, the pedestal peak is composed of two peaks, because the maximum voltage measured for the pedestal can be sometimes negative and sometimes positive, and there is no averaging. Again, the signal and noise pedestal shapes are somewhat different due to reasons discussed in Section 4.4.1. The other three peaks in the signal distribution are associated with the firing of one, two and three pixels, and the equal spacing between the peaks shows a discrete change in maximum voltage values, which correspond to individual pixels firing. The second peak in the noise distribution is again due to the thermally activated pixels, as was explained in Section 4.4.1.

5 Conclusion

We tested a number of silicon photomultiplier (SiPM) devices during the HCAL Test Beam 2009 to characterize their responses to MIP interactions. In this note, we presented results for the Zecotek micro-pixel avalanche photodiode (MAPD). Our experiment used a standard SiPM to trigger the readout of data collected by a free-running oscilloscope. We defined the signal from the SiPM under study in two ways: the average and maximum voltages of a pulse. We found no anomalous behavior in the response of a MAPD running in Geiger mode to MIPs. In particular, we found that a MIP fires a single pixel most of the time, but can fire two or more with a lower probability. As expected, the time distribution of thermally activated pixels is uniform.

6 Acknowledgements

We would like to thank the CERN staff and the technical staffs of the institutes participating in the HCAL Test Beam 2009 for their vital contributions. We also thank the CMS group members of Florida State University for useful discussions. This work is supported by the United States Department of Energy grants.

References

[1] Dolgoshein, B. et al., NIM **A504**, 48-52, (2003)

[2] Teshima, M. et al., *SiPM development for Astroparticle Physics applications*, Proceedings of the 30th International Cosmic Ray Conference. July 3 - 11, (2007)

[3] Korpar, S. et al., *Measurements of Cherenkov Photons with Silicon Photomultipliers*, arXiv:0812.0531v1

[4] S. Abdullin *et al.* [CMS HCAL Collaborations],"Design, performance, and calibration of the CMS Hadron-outer calorimeter," Eur. Phys. J. C **57** (2008) 653.

[5] Center of Perspective Technology and Apparatus, Moscow, Russia URL:http://www.cpta-apd.ru/eng/APDen.html

[6] Fondazione Bruno Kessler, Trento, Italy URL: http://www.fbk.eu/

[7] Hamamatsu Photonics, Japan URL: http://sales.hamamatsu.com/

[8] Zecotek, Vancouver, BC, Canada URL: http://www.zecotek.com/503/1107/

[9] Zecotek, Vancouver, BC, Canada URL: http://www.zecotek.com/EN/426/1525

[10] Z.Ya. Sadygov, et al., Nuclear Instruments and Methods in Physics Research A 567 (2006) 70..73

[11] Z.Ya. Sadygov, Russian Patent Application 2005108324 of 24.03.2005

[12] Mikron, Switzerland URL: http://www.mikron.com/internet.nsf/ID/HomeEN

[13] HCAL Test Beam 2009, URL: https://twiki.cern.ch/twiki/bin/view/CMS/TestBeam2009

[1)] In general, the pedestal is the noise distribution. In our case, there are two sources for the noise (1) from thermally activated pixels and (2) everything else, including electronic noise. In this note, we refer to the latter as the pedestal.

APPENDIX B

SYNCHRONIZATION

A synchronization sub-group was formed, between the QCD High p_T group and the Exotica Multi-Jet group, to coordinate analyses with similar event and object selection. There are two sets of synchronization: one with the QCD group, and one with the Extinction Analysis group. All groups agreed on the following list of criteria:

- Use Kostas Kousouris ntuple software package, location: cvs UserCode/KKousour/QCDAnalysis
- Version: V00-05-013
- EPS Golden JSONs, Runs: 160404 to 167913
- CMSSW_4_2_4 release
- Global Tag: GR_R_42_V19
- JEC services: ak∗PFL1FastL2L3Residual, ak∗CaloL1L2L3Residual
- Configuration: ProcessedTreeProducer_data_cfg.py
- The jet p_{T} bin widths increase with jet p_{T}, corresponding approximately to the jet p_{T} resolution as a function of p_{T}: 0, 1, 5, 6, 8, 10, 12, 15, 18, 21, 24, 28, 32, 37, 43, 49, 56, 64, 74, 84, 97, 114, 133, 153, 174, 196, 220, 245, 272, 300, 330, 362, 395, 430, 468, 507, 548, 592, 638, 686, 737, 790, 846, 905, 967, 1032, 1101, 1172, 1248, 1327, 1410, 1497, 1588, 1684, 1784, 1890, 2000, 2116, 2238, 2366, 2500, 2640, 2787, 2941, 3103, 3273, 3450, 3637, 3832, 4037, 4252, 4477, 4713, 4961, 5220, 5492, 5777, 6076, 6389, 6717, 7000.

B.1 Extinction analysis

B.1.1 1st Synchronization

Synchronization with the Extinction group requirements were:

- HLT_Jet370v$*$ triggers
- Events with loose HCAL noise summary tag
- Events with a good primary vertex
- Use ak7PF Jets with a tight Jet ID
- 1.092 fb^{-1}
- 160404-167913 runs

Table B.1. Synchronization exercise with Extinction analysis group. The table is divided up into columns of rapidity: 0.5, 1.0, 1.5. The discrepancy in the 1.0 < |y| <= 1.5 column, may be due to rapidity bias applied in the Extinction analyzer software but not in our software. This body of work is limited to the central rapidity bin |y| < 0.5.

HLT_Jet370v∗						
	$\|\eta\| < 0.5$		$0.5 < \|\eta\| <= 1.0$		$1.0 < \|\eta\| <= 1.5$	
jet p_{T} bin	CI	Extinction	CI	Extinction	CI	Extinction
507	25107	25107	20751	20751	13022	12799
548	16147	16147	12967	12967	7653	7542
592	10045	10045	7945	7945	4233	4168
638	6126	6126	4833	4833	2499	2467
686	3884	3884	2999	2999	1417	1402
737	2399	2399	1793	1793	760	753
790	1544	1544	1047	1047	371	370
846	959	959	625	625	218	215
905	596	596	350	350	108	108
967	336	336	173	173	46	46
1032	174	174	129	129	21	21
1101	147	147	73	73	15	14
1172	87	87	28	28	5	5
1248	29	29	14	14	5	5
1327	25	25	14	14	0	0
1410	12	12	2	2	1	1
1497	5	5	2	2	0	0
1588	1	1	1	1	0	0
1684	0	0	0	0	0	0
1784	0	0	0	0	0	0
1890	2	2	0	0	0	0

B.1.2 2nd Synchronization on 2fb^{-1} of 2011 Data

- HLT_Jet300v∗ trigger
- Events with loose HCAL noise summary tag
- Events with a good primary vertex
- Use ak7PF Jets with a tight Jet ID

Table B.2. Synchronization exercise with Extinction analysis group. This synchronization is over the 2.004/fb of 2011 data. The table is divided up into columns of rapidity: 0.5, 1.0, 1.5. The discrepancy in the 1.0 < |y| <= 1.5 column, may be due to rapidity bias applied in the Extinction analyzer but not in our analyzer. This analysis is limited to the central rapidity bin |y| < 0.5.

HLT_Jet300v1						
	$\|\eta\| < 0.5$		$0.5 < \|\eta\| <= 1.0$		$1.0 < \|\eta\| <= 1.5$	
jet p_{T} bin	CI	Extinction	CI	Extinction	CI	Extinction
395	15812	15812	13665	13665	9119	8931
430	10106	10106	8578	8578	5705	5590
468	6060	6060	5204	5204	3118	3056
507	3710	3710	3109	3109	1884	1855
548	2436	2436	1863	1863	1169	1152
592	1390	1390	1158	1158	602	595
638	873	873	698	698	369	366
686	593	593	441	441	244	243
737	341	341	299	299	122	121
790	220	220	162	162	51	51
846	127	127	95	95	27	26
905	84	84	45	45	16	16
967	48	48	28	28	3	3
1032	26	26	17	17	6	6
1101	27	27	11	11	4	3
1172	13	13	5	5	2	2
1248	5	5	3	3	1	1
1327	2	2	2	2	0	0
1410	5	5	1	1	1	1
1497	0	0	0	0	0	0
1588	0	0	0	0	0	0
1684	0	0	0	0	0	0
1784	0	0	0	0	0	0
1890	0	0	0	0	0	0

Table B.3. Synchronization exercise with Extinction analysis group. This synchronization is over the 2.004/fb of 2011 data. The table is divided up into columns of rapidity: 0.5, 1.0, 1.5. The discrepancy in the 1.0 < |y| <= 1.5 column, may be due to rapidity bias applied in the Extinction analyzer but not in our analyzer. This analysis is limited to the central rapidity bin |y| < 0.5.

HLT_Jet300v2						
	$\|\eta\| < 0.5$		$0.5 < \|\eta\| <= 1.0$		$1.0 < \|\eta\| <= 1.5$	
jet p_{T} bin	CI	Extinction	CI	Extinction	CI	Extinction
395	12779	12779	10901	10901	7652	7487
430	7973	7973	7014	7014	4544	4452
468	4843	4843	4252	4252	2532	2491
507	2925	2925	2425	2425	1539	1519
548	1905	1905	1501	1501	888	873
592	1203	1203	1041	1041	507	493
638	823	823	581	581	305	302
686	475	475	355	355	168	164
737	297	297	220	220	95	93
790	182	182	127	127	40	40
846	146	146	59	59	31	31
905	72	72	48	48	11	11
967	38	38	20	20	8	8
1032	16	16	16	16	0	0
1101	22	22	11	11	1	1
1172	11	11	5	5	2	2
1248	2	2	1	1	0	0
1327	4	4	1	1	0	0
1410	2	2	0	0	0	0
1497	0	0	0	0	0	0
1588	0	0	0	0	0	0
1684	0	0	0	0	0	0
1784	0	0	0	0	0	0
1890	0	0	0	0	0	0

Table B.4. Synchronization exercise with Extinction analysis group. This synchronization is over the 2.004/fb of 2011 data. The table is divided up into columns of rapidity: 0.5, 1.0, 1.5. The discrepancy in the 1.0 < |y| <= 1.5 column, may be due to rapidity bias applied in the Extinction analyzer but not in our analyzer. This analysis is limited to the central rapidity bin |y| < 0.5.

HLT_Jet300v3						
	$\|\eta\| < 0.5$		$0.5 < \|\eta\| <= 1.0$		$1.0 < \|\eta\| <= 1.5$	
jet p_{T} bin	CI	Extinction	CI	Extinction	CI	Extinction
395	50861	50861	43809	43809	29944	29285
430	32073	32073	27408	27408	18072	17737
468	19322	19322	16284	16284	10344	10175
507	12097	12097	9843	9843	6274	6162
548	7695	7695	6133	6133	3588	3541
592	4877	4877	3769	3769	2040	2011
638	2902	2902	2300	2300	1160	1139
686	1819	1819	1406	1406	633	626
737	1109	1109	844	844	365	363
790	755	755	471	471	183	182
846	425	425	308	308	114	112
905	279	279	172	172	49	49
967	170	170	81	81	20	20
1032	79	79	67	67	7	7
1101	57	57	34	34	6	6
1172	41	41	8	8	1	1
1248	12	12	6	6	2	2
1327	13	13	5	5	0	0
1410	4	4	1	1	0	0
1497	5	5	1	1	0	0
1588	1	1	1	1	0	0
1684	0	0	0	0	0	0
1784	0	0	0	0	0	0
1890	0	0	0	0	0	0

Table B.5. Synchronization exercise with Extinction analysis group. This synchronization is over the 2.004/fb of 2011 data. The table is divided up into columns of rapidity: 0.5, 1.0, 1.5. The discrepancy in the 1.0 < |y| <= 1.5 column, may be due to rapidity bias applied in the Extinction analyzer but not in our analyzer. This analysis is limited to the central rapidity bin |y| < 0.5.

HLT_Jet300v4						
	$\|\eta\| < 0.5$		$0.5 < \|\eta\| <= 1.0$		$1.0 < \|\eta\| <= 1.5$	
jet p_{T} bin	CI	Extinction	CI	Extinction	CI	Extinction
395	373	373	335	335	224	224
430	256	256	197	197	130	130
468	146	146	135	135	75	75
507	88	88	67	67	40	37
548	74	74	62	62	23	23
592	29	29	25	25	14	14
638	24	24	27	27	12	12
686	20	20	15	15	7	7
737	12	12	4	4	5	5
790	4	4	4	4	1	1
846	1	1	4	4	0	0
905	3	3	1	1	0	0
967	2	2	0	0	0	0
1032	2	2	0	0	0	0
1101	1	1	0	0	0	0
1172	0	0	0	0	0	0
1248	1	1	0	0	0	0
1327	1	1	0	0	0	0
1410	0	0	0	0	0	0
1497	0	0	0	0	0	0
1588	0	0	0	0	0	0
1684	0	0	0	0	0	0
1784	0	0	0	0	0	0
1890	0	0	0	0	0	0

Table B.6. Synchronization exercise with Extinction analysis group. This synchronization is over the 2.004/fb of 2011 data. The table is divided up into columns of rapidity: 0.5, 1.0, 1.5. The discrepancy in the 1.0 < |y| <= 1.5 column, may be due to rapidity bias applied in the Extinction analyzer but not in our analyzer. This analysis is limited to the central rapidity bin |y| < 0.5.

HLT_Jet300v5						
	$\|\eta\| < 0.5$		$0.5 < \|\eta\| <= 1.0$		$1.0 < \|\eta\| <= 1.5$	
jet p_{T} bin	CI	Extinction	CI	Extinction	CI	Extinction
395	101562	101562	87050	87050	58882	57626
430	65229	65229	55184	55184	35769	35028
468	39114	39114	32908	32908	20742	20356
507	24253	24253	19868	19868	12100	11876
548	15697	15697	12597	12597	7197	7074
592	9476	9476	7400	7400	4019	3955
638	5839	5839	4557	4557	2307	2273
686	3638	3638	2873	2873	1254	1241
737	2379	2379	1656	1656	683	676
790	1400	1400	1038	1038	401	401
846	889	889	605	605	206	205
905	543	543	328	328	100	100
967	326	326	194	194	61	61
1032	186	186	110	110	19	19
1101	119	119	78	78	11	10
1172	77	77	37	37	3	3
1248	34	34	10	10	5	5
1327	15	15	8	8	0	0
1410	7	7	3	3	0	0
1497	3	3	2	2	0	0
1588	5	5	3	3	0	0
1684	1	1	0	0	0	0
1784	0	0	0	0	1	1
1890	2	2	0	0	0	0

B.1.3 QCD Synchronization

Synchronization with the QCD group requirements were:

- A combination of HLT_Jet240v∗ and HLT_Jet300v∗ triggers with all prescales included
- Events with loose HCAL noise summer tag
- Events with good primary vertex

- Use ak5 PF and Calo Jets with a tight Jet ID

Table B.7. Synchronization exercise with the QCD analysis group.

Selection criterion	QCD	CI
HLT_Jet240_v1		
Events passing trigger:	390359	390359
Events passing PV:	364950	364950
Events passing PV and loose HCAL noise:	322593	322593
PFJets with pT > 362 GeV	16261	16261
CaloJets with pT > 362 GeV	15813	15813
PFJets with tightJetID	16117	16117
CaloJets with tightJetID	15642	15642
HLT_Jet240_v2		
Events passing trigger:	427297	427297
Events passing PV:	426735	426735
Events passing PV and loose HCAL noise:	363322	363322
PFJets with pT > 362 GeV	18967	18967
CaloJets with pT > 362 GeV	18797	18797
PFJets with tightJetID	18475	18475
CaloJets with tightJetID	18164	18164
HLT_Jet240_v3		
Events passing trigger:	174703	174703
Events passing PV:	174510	174510
Events passing PV and loose HCAL noise:	150867	150867
PFJets with pT > 362 GeV	8603	8603
CaloJets with pT > 362 GeV	8512	8512
PFJets with tightJetID	8456	8456
CaloJets with tightJetID	8299	8299
HLT_Jet240_v4		
Events passing trigger:	671651	671651
Events passing PV:	671142	671142
Events passing PV and loose HCAL noise:	582857	582857
PFJets with pT > 362 GeV	33515	33515
CaloJets with pT > 362 GeV	32963	32963
PFJets with tightJetID	33097	33097
CaloJets with tightJetID	32430	32430

Table B.8. Synchronization exercise with the QCD analysis group.

Selection criterion	QCD	CI
HLT_Jet240_v5		
Events passing trigger:	4944	4944
Events passing PV:	4923	4923
Events passing PV and loose HCAL noise:	3962	3962
PFJets with pT > 362 GeV	260	260
CaloJets with pT > 362 GeV	250	250
PFJets with tightJetID	254	254
CaloJets with tightJetID	242	242
HLT_Jet240_v6		
Events passing trigger:	326230	326230
Events passing PV:	325114	325114
Events passing PV and loose HCAL noise:	293834	293834
PFJets with pT > 362 GeV	16993	16993
CaloJets with pT > 362 GeV	16705	16705
PFJets with tightJetID	16838	16838
CaloJets with tightJetID	16509	16509

Table B.9. Synchronization exercise with the QCD analysis group. The jet count comparison shows excellent agreement, though there is a one jet discrepancy shown in red.

Selection criterion	QCD	CI
HLT_Jet300_v1		
Events passing trigger:	403347	403347
Events passing PV:	402509	402509
Events passing PV and loose HCAL noise:	339459	339459
PFJets with pT > 362 GeV	58695	58695
CaloJets with pT > 362 GeV	58229	58229
PFJets with tightJetID	57201	57201
CaloJets with tightJetID	56215	56215
HLT_Jet300_v2		
Events passing trigger:	292854	292854
Events passing PV:	292329	292329
Events passing PV and loose HCAL noise:	247228	247228
PFJets with pT > 362 GeV	47352	47352
CaloJets with pT > 362 GeV	46845	46845
PFJets with tightJetID	46420	46420
CaloJets with tightJetID	45553	45553

Table B.10. Synchronization exercise with the QCD analysis group. The jet count comparison shows excellent agreement, though there is a one jet discrepancy shown in red.

Selection criterion	QCD	CI
HLT_Jet300_v3		
Events passing trigger:	1129923	1129923
Events passing PV:	1128278	1128278
Events passing PV and loose HCAL noise:	968290	968290
PFJets with pT > 362 GeV	187027	187027
CaloJets with pT > 362 GeV	184250	184249
PFJets with tightJetID	184651	184651
CaloJets with tightJetID	181246	181245
HLT_Jet300_v4		
Events passing trigger:	9182	9182
Events passing PV:	9122	9122
Events passing PV and loose HCAL noise:	7338	7338
PFJets with pT > 362 GeV	1440	1440
CaloJets with pT > 362 GeV	1435	1435
PFJets with tightJetID	1414	1414
CaloJets with tightJetID	1396	1396
HLT_Jet300_v5		
Events passing trigger:	506185	506185
Events passing PV:	502739	502739
Events passing PV and loose HCAL noise:	443746	443746
PFJets with pT > 362 GeV	85274	85274
CaloJets with pT > 362 GeV	83831	83831
PFJets with tightJetID	84362	84362
CaloJets with tightJetID	82693	82693

APPENDIX C

PYTHIA

C.1 Pythia samples

The CMS official Pythia samples used in this work are:

- /QCD_Pt-*_TuneZ2_7TeV_pythia6/Summer11-PU_S4_START42_V11-v1/AODSIM,
- /QCDplus3TeVcontact_pt-*_7TeV-pythia6/Summer11-PU_S4_START42_V11-v1/AODSIM,
- /QCDplus5TeVcontact_pt-*_7TeV-pythia6/Summer11-PU_S4_START42_V11-v1/AODSIM,
- /QCDplus8TeVcontact_pt-*_7TeV-pythia6/Summer11-PU_S4_START42_V11-v1/AODSIM,
- /QCDplus12TeVcontact_pt-*_7TeV-pythia6/Summer11-PU_S4_START42_V11-v1/AODSIM,

where the naming convention is as follows: type of process, p_{T} range, center-of-mass energy, type of generator, MC production era, pile up conditions, software version, processing iteration, data format type.

C.2 Pythia configuration

In Pythia, the ITCM(5) term (>= 1) allows for the introduction of anomalous couplings in addition to the Standard Model ones. When set to unity, the model assumes that only the u and d quarks are composite, at the scale studied. When the ITCM(5) term is 2 or 4, composite terms are included in the interactions between all quarks, and when the ITCM(5) term equals 3 the interaction produces events using the helicity non-conserving model. The sign of the contact interaction term is set with the parameter RTCM(42). We used ITCM(5) = 2, that is interactions between all quarks with a positive contact term for all contact interaction models in our analysis.

Table C.1. PYTHIA 6.422 configuration for $\Lambda = 8$ TeV contact interactions.

PYTHIA 6.422 settings specific to contact interactions	
Settings	Description
ITCM(5)=2	Switch on contact int. for all quarks
RTCM(41)=8000	Set contact scale Λ to 8 TeV
RTCM(42)=1	Sign of contact int. is +
MSUB(381)=1	$q_i q_j \to q_i q_j$ via QCD plus a contact int.
MSUB(382)=1	$q_i \bar{q}_i \to q_k \bar{q}_k$ via QCD plus a contact int.
MSUB(13)=1	$q_i \bar{q}_i \to gg$ via normal QCD
MSUB(28)=1	$q_i g \to q_i g$ via normal QCD
MSUB(53)=1	$gg \to q_k \bar{q}_k$ via normal QCD
MSUB(68)=1	$gg \to gg$ via normal QCD
CKIN(3)=170	minimum $\hat{p}_T$ for hard int.
CKIN(4)=230	maximum $\hat{p}_T$ for hard int.

APPENDIX D

COPYRIGHTS

The three publications are all open access.

D.1 Physics Review D

November 2012

Terms and conditions associated with the American Physical Society Transfer of Copyright Agreement

Copyright to the [above-listed] unpublished and original article submitted by the [above] author(s), the abstract forming part thereof, and any subsequent errata (collectively, the Article) is hereby transferred to the American Physical Society (APS) for the full term thereof throughout the world, subject to the Author Rights (as hereinafter defined) and to acceptance of the Article for publication in a journal of APS. This transfer of copyright includes all material to be published as part of the Article (in any medium), including but not limited to tables, figures, graphs, movies, other multimedia files, and all supplemental materials. APS shall have the right to register copyright to the Article in its name as claimant, whether separately or as part of the journal issue or other medium in which the Article is included.

The author(s), and in the case of a Work Made For Hire, as defined in the U.S. Copyright Act, 17 U.S.C. 101, the employer named [below], shall have the following rights (the Author Rights):

1. All proprietary rights other than copyright, such as patent rights.

2. The nonexclusive right, after publication by APS, to give permission to third parties to republish print versions of the Article or a translation thereof, or excerpts therefrom,

without obtaining permission from APS, provided the APS-prepared version is not used for this purpose, the Article is not republished in another journal, and the third party does not charge a fee. If the APS version is used, or the third party republishes in a publication or product charging a fee for use, permission from APS must be obtained.

3. The right to use all or part of the Article, including the APS-prepared version without revision or modification, on the author(s) web home page or employers website and to make copies of all or part of the Article, including the APS-prepared version without revision or modification, for the author(s) and/or the employers use for educational or research purposes.

4. The right to post and update the Article on free-access e-print servers as long as files prepared and/or formatted by APS or its vendors are not used for that purpose. Any such posting made or updated after acceptance of the Article for publication shall include a link to the online abstract in the APS journal or to the entry page of the journal. If the author wishes the APS-prepared version to be used for an online posting other than on the author(s) or employers website, APS permission is required; if permission is granted, APS will provide the Article as it was published in the journal, and use will be subject to APS terms and conditions.

5. The right to make, and hold copyright in, works derived from the Article, as long as all of the following conditions are met: (a) at least one author of the derived work is an author of the Article; (b) the derived work includes at least ten (10) percent of new material not covered by APSs copyright in the Article; and (c) the derived work includes no more than fifty (50) percent of the text (including equations) of the Article. If these conditions are met, copyright in the derived work rests with the authors of that work, and APS (and its successors and assigns) will make no claim on that copyright. If these conditions are not met, explicit APS permission must be obtained. Nothing in this Section shall prevent APS (and its successors and assigns) from exercising its rights in the Article.

6. If the Article was prepared under a U.S. Government contract, the government shall have the rights under the copyright to the extent required by the contract.

All copies of part or all of the Article made under any of the Author Rights shall include the appropriate bibliographic citation and notice of the APS copyright.

By signing this Agreement, the author(s), and in the case of a Work Made For Hire, the employer, jointly and severally represent and warrant that the Article is original with the author(s) and does not infringe any copyright or violate any other right of any third parties, and that the Article has not been published elsewhere, and is not being considered for publication elsewhere in any form, except as provided herein. If each authors signature does not appear [below], the signing author(s) represent that they sign this Agreement as authorized agents for and on behalf of all authors who have the legal right to transfer copyright and that this Agreement and authorization is made on behalf of the same. The signing author(s) (and, in the case of a Work Made For Hire, the signing employer) also represent and warrant that they have the full power to enter into this Agreement and to make the grants contained herein.

D.2 Science IOP

For papers published in our open access proceedings titles IOP Publishing no longer requires authors to sign and submit copyright forms. Our regular journals are unaffected by this change. Authors who wish to publish a paper in the following titles:

- Journal of Physics: Conference Series (JPCS),
- IOP Conference Series: Materials Science and Engineering (MSE),
- IOP Conference Series: Earth and Environmental Science (EES),

are asked to submit a paper only if all authors of the paper can agree in full to the terms of the licence. All papers submitted to us for publication in the above titles will be published according to the following terms and conditions.

D.2.1 Licence terms and conditions

By submitting your paper to the conference organizer, you, as author/representative of all the authors, grant a royalty free licence to IOP Publishing Limited (IOP) to use the copyright in the paper for the full term of copyright in all ways otherwise restricted by copyright, including the right to reproduce, distribute and communicate the article to the public and to make any other use which IOP may choose world-wide, by all means, media and formats, whether known or unknown at the date of submission, to the conference organizer.

This licence does not transfer the copyright in the paper as submitted which therefore remains with the authors or their employer, as appropriate. IOP encourages authors to use the paper in any way provided that, where possible, he/she displays citation information and the IOP Proceedings Licence Notice, for electronic use, best efforts are made to include a link to the online abstract in the journal and no author offers the paper to another publisher (prior to withdrawal or rejection) or includes it in another publisher's website.

However, a re-written and extended version of the paper may be published in another journal provided such re-use is within generally accepted ethical scientific limits and provided further citation information and the IOP Proceedings Licence Notice is displayed if possible, and for electronic use best efforts are made to include a link to the online abstract in the journal.

By granting this licence, the author warrants that the paper he/she is submitting is his/her original work, has not been published previously (other than in a research thesis or dissertation which fact has been notified to the conference organizer in writing), all named authors participated sufficiently in the conception and writing of the paper, have received a final version of the paper, agree to its submission and take responsibility for it, and the submission has been approved as necessary by the authorities at the establishment where the research was carried out.

By granting this licence, the author also warrants that he/she acts on behalf of, and with the knowledge of, all authors of the paper, that the paper does not infringe any third party rights, it contains nothing libellous, all factual statements are, to the best of the authors'

knowledge, true or based on valid research conducted according to accepted norms, and all required permissions have been obtained.

D.2.2 The IOP Proceedings Licence Notice

The IOP Proceedings Licence Notice should be displayed as: Published under licence in Journal Title by IOP Publishing Ltd. where Journal Title is one of: Journal of Physics: Conference Series, IOP Conference Series: Materials Science and Engineering, IOP Conference Series: Earth and Environmental Science.

D.3 CERN

Supporting Open Access Publishing

CERN is committed to Open Access and the Scientific Information Service implements the vision and policies of the Organization.

CERNs vision is directly inspired to our establishing Convention which stipulates that "all results of its experimental and theoretical work shall be published or otherwise made generally available. As a publicly and internationally funded research institution we believe everyone should get access to our results without any financial barrier. Open Access publishing is a tool to reach this objective. CERN recognizes the value journals add, at a cost, to scientific information, and is implementing a series of initiative to facilitate Open Access publishing in high-quality journals.

The most important tool to implement this vision is the SCOAP3 initiative, through which CERN and partners in over 20 countries are working to convert to Open Access existing high-quality High-Energy Physics journals. While waiting for the SCOAP3 initiative to be operational, and all High-Energy Physics literature to be available Open Access, CERN and leading publishers in the field (the American Physical Society, Elsevier, SISSA and Springer) have reached agreements to make the scientific publications from the LHC accelerator available Open Access and under a Creative Common license, thus complying with the publication policy of our Physics Department

In other fields, such as accelerator science, CERN contributes to Open Access by contributing to the sponsorship the Open Access journal Physical Review Special Topics Accelerators and Beams

In addition, CERN contributes to underwriting part of the running costs of arXiv, as well as building tools for open access to all this information such as INSPIRE. We also co-ordinated a consortium of libraries, publishers and funding agencies, SOAP, in a large-scale study to identify the demand and offer for Open Access and its main drivers and barriers.

These initiatives do not cover the entire spectrum of the literature produced at CERN. As signatories of COPE, we take further action to encourage a transition to Open Access publishing. In particular, recognizing that high-quality scientific publishing has a cost, and scientific journals play a key role in the quality-assurance process, the Scientific Information Service covers reasonable fees that some journals could charge in order to make research articles Open Access. This instrument is only available for articles published in Open Access journals that are entirely Open Access, and not for so called hybrid journals, which sell subscriptions and make part of their content available Open Access: the CERN Library has already paid for those journals, so Open Access fees cannot be covered. These arrangements apply for research articles spontaneously submitted by members of personnel. Applying is easy: just contact the Scientific Information Service to discuss arrangements.

REFERENCES

[1] Albert Einstein and Leopold Infeld. *The Evolution of Physics: From Early Concepts to Relativity and Quanta*. New York: Simon and Schuster, 1966. 1

[2] S. Willenbrock. The standard model and the top quark. 2002. hep-ph/0211067v3. 1.1

[3] Particle Data Group Collaboration. Review of particle properties. *Phys. Rev.*, **D66**:010001, 2002. PhysRevD.66.010001. 2.1

[4] CMS Collaboration. Observation of a new boson at a mass of 125 gev with the cms experiment at the lhc. *Phys. Lett.*, **B716**(1):30, 2012. arXiv:1207.7235. 2.1

[5] ATLAS Collaboration. Combined search for the standard model higgs boson using up to 4.9 fb^{-1} of pp collision data at with the atlas detector at the lhc. *Phys. Lett.*, **B710**(1):49, 2012. Science:0370-2693. 2.1

[6] Particle Data Group. The review of particle physics. *Phys. Rev.*, **D86**:010001, 2012. Phys.Rev.D66.010001.R. 2.1.1

[7] Peskin E M. and Schroeder D. V. *An Introduction to Quantum Field Theory*. 1995. 2.1.1

[8] R.E. Marshak. From the strong and weak Gell-Mann-Nishijima groups to QCD and QFD. 1987. CERN:000088213CER. 2.1.1

[9] Paritcle Data Group. 2010. rpp2010-rev-qcd. 2.1.1, 2.1.1, 2.1.2

[10] Craig D. Roberts. Strong QCD and Dyson-Schwinger Equations. 2012. arXiv:1203.5341. 2.1.1

[11] Antonio Pich. The standard model of electroweak interactions. 2012. arXiv:1201.0537. 2.1.1

[12] Michael E. Peskin and James D. Wells. How can a heavy higgs boson be consistent with the precision electroweak measurements? *Phys. Rev.*, **D64**:093003, 2001. PhysRevD.64.093003. 2.1.1

[13] CTEQ Collaboration. Handbook of perturbative QCD: Version 1.0. *Rev.Mod.Phys.*, 67:157, 1995. 2.1.2, 2.1.2

[14] David d'Enterria. Small-x qcd studies with cms at the lhc. 2007. arXiv:0703024. 2.1.2

[15] Giovanni Antonio Chirilli. High-energy qcd factorization from dis to pa collisions. 2012. arXiv:1209.1614. 2.1.2

[16] T. Sjöstrand, S. Mrenna, and P. Skands. PYTHIA 6.4 physics and manual. *JHEP*, 05:026, 2006. arXiv:0603175. 2.1.2

[17] Stefano Forte Fabrizio Caola and Juan Rojo. Hera data and dglap evolution: Theory and phenomenology. *Nuclear Physics*, **A854**(1):32, 2011. Science:S0375947410006512. 2.1.2

[18] Inclusive jet cross section in $\overline{p}p$ collisions at $\sqrt{s} = 1.8$ TeV. 2.2, 6

[19] CERN Collaboration. *LHC Design Report*. 2004. CERN:782076. 3.1, 3.1

[20] O. Domnguez G. Arduini H. Bartosik S. Claudet J. Esteban-Muller F. Roncarolo E. Shaposhnikova L. Tavian G. Rumolo, G. Iadarola. Lhc experience with different bunch spacings in 2011 (25, 50 and 75ns). In *Proceedings of Chamonix 2012 workshop on LHC Performance*, 2012. CERN. 3.1

[21] CMS Collaboration. The CMS experiment at the CERN LHC. *JINST*, 3:S08004, 2008. IOP:1748-0221. 3.1

[22] CMS Collaboration. The cms- experiment at the cern lhc. *Journal of Instrumentation*, 3, 2008. IOP:S08004. 3.2

[23] CMS Collaboration. CMS technical design report, volume II: Physics performance. *J. Phys.*, **G34**:995, 2007. Science:0954-3899. 3.2

[24] CMS Collaboration. Performance of the CMS Level-1 Trigger during Commissioning with Cosmic Ray Muons. *JINST*, 5:T03002, 2010. arXiv:0911.5422. 3.2

[25] CMS Collaboration. Commissioning of the CMS High Level Trigger. *JINST*, 4:P10005, 2009. arXiv:0908.1065. 3.2

[26] CMS Collaboration. Paticle-flow event reconstruction in cms and performance for jets, taus, and E_T^{miss}. 2009. CMS-PAS-PFT-09-001. 4.1.3, 4.1.4, 4.2.2, 4.2.3

[27] CMS Collaboration. Shape, transverse size, and charged-hadron multiplicity of jets in pp collisions at $\sqrt{s} = 7$ TeV. *Journal of High Energy Physics*, 2012, 2012. arXiv:1204.3170. 4.2.1

[28] CMS Collaboration. Jet performance in pp collisions at $\sqrt{s} = 7$ TeV. 2010. CMS-PAS-JME-10-003. 4.2.3

[29] Gerald C. Blazey, Jay R. Dittmann, Stephen D. Ellis, V. Daniel Elvira, K. Frame, et al. Run II jet physics. page 47, 2000. arXiv:0005012. 4.2.3

[30] S.D. Ellis, J. Huston, K. Hatakeyama, P. Loch, and M. TAloriesmann. Jets in hadron-hadron collisions. *Progress in Particle and Nuclear Physics*, 60:484, 2008. arXiv:0712.2447. 4.2.3

[31] C. Buttar, J. D'Hondt, M. Kramer, G. Salam, M. Wobisch, et al. Standard model handles and candles working group: Tools and jets summary report. Technical report, 2008. arXiv:0803.0678. 4.2.3

[32] Matteo Cacciari, Gavin P. Salam, and Gregory Soyez. The Anti-k(t) jet clustering algorithm. *JHEP*, 0804:063, 2008. arXiv:0802.1189. 4.2.3

[33] CMS Collaboration. Jet energy calibration and transverse momentum resolution in cms. *JINST*, 6:P11002, 2011. CMS-PAS-JME-10-011. 4.2.4

[34] CMS collaboration. Determination of the jet energy scale in cms. *Journal of Physics: Conference Series*, 404(1):012013, 2012. IOP:012013. 4.2.4, 5.4.1

[35] CMS Collaboration. Identification and filtering of uncharacteristic noise in the cms hadron collider. *JINST*, 5:T03014, 2010. arXiv:0911.4881. 5.1.4

[36] CMS Collaboration. Calorimeter jet quality criteria for the first cms collision data. 2010. CMS-PAS-JME-09-008. 5.1.4

[37] Kenneth Lane and Stephen Mrenna. Collider phenomenology of technihadrons in the technicolor straw man model. *Phys. Rev.*, **D67**:115011, 2003. PhysRevD.67.115011. 5.2.1

[38] Estia J. Eichten, Kenneth D. Lane, and Michael E. Peskin. New tests for quark and lepton substructure. *Phys. Lett.*, 50:811, 1983. PhysRevLett.50.811. 5.2.1

[39] E. Eichten, I. Hinchliffe, K. Lane, and C. Quigg. Supercollider physics. *Rev. Mod. Phys.*, 56:579, 1984. RevModPhys.56.579. 5.2.1

[40] P. Chiappetta and M. Perrottet. Possible bounds on compositeness from inclusive one jet production in large hadron colliders. *Phys. Lett.*, **B253**:489, 1991. Science:037026939191757M. 5.2.1

[41] Kenneth D. Lane. Electroweak and flavor dynamics at hadron colliders. arXiv:9605257. 5.2.1

[42] T. Kluge, K. Rabbertz, and Wobisch. Fast pQCD calculations for PDF fits. 2006. arXiv:0609285. 5.2.2

[43] Zhao Li Hung-Liang Lai, Joey Huston et al. Uncertainty induced by qcd coupling in the cteq global analysis of parton distributions. 2010. arXiv:1004.4624. 5.2.2, 5.4.2, 5.4.2

[44] CMS Collaboration. Measurement of the inclusive jet cross section in pp collisions at $\sqrt{s} = 7$ TeV. *Phys. Lett.*, 107:132001, 2011. PhysRevLett.107.132001. 5.2.2, 5.4.1, 5.4.2

[45] S. Agostinelli et al. GEANT4—a simulation toolkit. *Nucl. Instrum. and Meth. A*, 506:250, 2003. 5.2.2

[46] J. F. Owens. Private communication, 2011. 5.2.2

[47] CMS Collaboration. Measurement of the inclusive jet cross section in pp collisions at $\sqrt{s} = 7$ TeV. 2010. 5.4.1

[48] J. Pumplin, D.R. Stump, J. Huston, H.L. Lai, Pavel M. Nadolsky, et al. New generation of parton distributions with uncertainties from global QCD analysis. *JHEP*, 0207:012, 2002. JHEP:581996. 5.4.1

[49] M R Whalley D Bourilkov, R C Group. Lhapdf: Pdf use from the tevatron to the lhc. 2006. arXiv:0605240. 5.4.2

[50] J. O. Berger, J.M. Bernardo, and D. Sun. The formal definition of reference priors. *Ann. Stat.*, 37:905, 2009. arXiv. 5.4.3

[51] D. Sun and J. O. Berger. Reference priors with partial information. *Biometrika*, 85:55, 1998. Biomet. 5.4.3

[52] L. Demortier, S. Jain, and H. B. Prosper. Reference priors for high energy physics. *Phys. Rev.*, **D82**:034002, 2010. PhysRevD.82.034002. 5.4.3

[53] J. Gao, C. Li, J. Wang, H. Zhu, and C. Yuan. Next-to-leading qcd effect on the quark compositeness search at the lhc. *Phys. Rev. Lett.*, 106:142001, 2011. PhysRevLett.106.142001. 6.1

[54] Jun Gao. Cijet: a program for computation of jet cross sections induced by quark contact interactions at hadron colliders. 2013. arXiv:1301.7263. 6.1

[55] CMS Collaboration. *Journal of Physics: Conference Series*, 331(7):072019, 2011. DOI:072019. A

[56] CMS Collaboratidon. Response of silicon photomultipliers to minimum ionizing particles. 2010. CERN:CMS-DN-2009-021. A

[57] CMS Collaboration. Technology and instrumentation in particle physics 2011 upgrade of the cms hadron outer calorimeter with sipms for the cms hcal collaboration. 2010. FNAL. A

BIOGRAPHICAL SKETCH

Jeffrey David Haas

Citizenship: USA

Education: PhD in Physics from Florida State University, 2013

Objective: Placement in a career position which inspires interest and passion.

Publications

- CMS Collaboration, Search for contact interactions using the inclusive jet pT spectrum in pp collisions at $\sqrt{s}$ =7 TeV, arXiv:1301.5023, Phys. Rev. D 87, 052017, 2013.
- CMS Collaboration, Measurement of the Inclusive Jet Cross Section in pp Collisions at $\sqrt{s}$ = 7 TeV, arXiv:1106.0208, Phys.Rev.Lett.107:132001, 2011.
- CMS Collaboration, CMS Distributed Computing Workflow Experience, Journal of Physics: Conference Series IOPScience 072019, 2011.
- J. Haas, A. Hahn, H. Prosper, S. Sekmen, Response of Silicon Photomultipliers to Minimum Ionizing Particles, CMS-DN-2009-021, 2010.

Presentations

- 10/18/2010 Invited, Official CMS Representative, CHEP2010: International Conference on Computing in High Energy and Nuclear Physics 2010, Taipei (Taiwan), "CMS Distributed Computing Workflow Experience"
- 03/22/2010 Invited, Official CMS Representative, All Experimenters' Meetings, Fermilab, "LHC and CMS Update"
- 02/03/2010 Invited, Christos Leonidopoulos: Fire-side chat with the CMS Deputy Trigger Coordinator, Fermilab "Triggers for SUSY Analyses"

- 10/22/2009 Official CMS Representative, Canadian American Mexican Graduate Student Physics Conference, Universidad Nacional Autonoma de Mexico Campus Morelos , Acapulco (Mexico), "Detection of Minimum Ionizing Particles with Silicon Photomultiplier"

- 05/08/2009 Invited, Berkeley Workshop on Physics Opportunities with the First LHC Data, Berkeley, CA, "Finding Supersymmetry without using Missing Transverse Energy"

- 05/05/2009 APS Denver, CO "Finding Supersymmetry without using Missing Transverse Energy"

Service Work Experience

- Tier-1 data operations team member

  Analyses of large data volumes, data mining, EGEE/OSG public GRID infrastructures.

  Workload management of globally distributed grid production and processing infrastructure for CMS.

  Object oriented software development and software optimization.

  Strong communication skills and proven record of teamwork and leadership.

Awards

- 2010 Physics Award Florida State University "Hagopian Family Endowment Award"

Software Experience

- Programming: C#, C++, C, ROOT, HTML, LabVIEW, Shell scripting, FORTRAN, IDL, Javascript, PHP, LaTeX, Visual Basic, .Net, COBOL, Visual Studio 2005 and 2008

- Databases: Oracle, Sequel, Informix

- Applications: GIMP, Adobe, Microsoft, Open Office Suite, Matlab, Mathematica, Virtual Box, PYTHIA, MadGraph, GEANT4, PGS, Visual Studio

- Operating Systems: Windows, Linux (Ubuntu, Fedora, Scientific Linux 5)
- Distributed Computing: Condor, CRAB, ProdAgent

Hardware Experience

- Test beam evaluation of Micro-pixel Avalanche Photo Diodes (MAPD), CERN
- Assembled Fiber Optic cables
- Implementation design for SiPMs
- Semiconductor Fabrication:
- Characterization of Niobium Thin Films, SFSU Cryogenic Electronics Group